Large Eddy Simulation of Boundary Shear Stress in Water Channels of Rectangular and Trapezoidal Shapes

Rui Zeng

A Thesis
in
The Department
of
Building, Civil, and Environmental Engineering

Presented in Partial Fulfilment of the Requirements
for the Degree of Master of Applied Science in Civil Engineering at
Concordia University
Montreal, Quebec, Canada

October 2016

CONCORDIA UNIVERSITY
School of Graduate Studies

This is to certify that the thesis prepared

By: Rui Zeng

Entitled: Large Eddy Simulation of Boundary Shear Stress in Rectangular and Trapezoidal Channels

and submitted in partial fulfillment of the requirements for the degree of

Master of Applied Science (Civil Engineering)

complies with the regulations of the University and meets the accepted standards with respect to originality and quality.

Signed by the final examining committee:

Dr. L. Wang Chair

Dr. M. Paraschivoiu, MIE, External-to-Program Examiner

Dr. A. S. Ramamurthy Examiner

Dr. S. S. Li Supervisor

Approved by Dr. F. Haghighat
Chair of Department or Graduate Program Director

Dr. A. Asif
Dean of Faculty

Date October, 2016

ABSTRACT

Large Eddy Simulation of Boundary Shear Stress in Water Channels of Rectangular and Trapezoidal Shapes

Rui Zeng

The flow of water in an open channel is typically turbulent, exerting shear stresses on its boundaries, i.e. the channel-bed and sidewalls. Knowledge of boundary shear stress (BSS) distributed at a channel section has many important applications. For example, the BSS distributions affect channel stability, fish habitats, and the resuspension and subsequent transport of bed sediments. However, knowledge of the BSS is far from being complete, partly because there are technical difficulties in measuring shear stresses distributed across the bed width and sidewalls. This research thesis aims to investigate BSS distributions by means of large eddy simulation (LES). This numerical technique is superior to the commonly used traditional computational fluid dynamics approaches, with respect to detailed predictions of near-boundary flow.

Water channels of rectangular and trapezoidal shapes under open-water as well as ice-covered conditions were included as LES domains in this study. The LES results of BSS from this study were compared with available data from laboratory experiments. The comparisons show that the LES results capture typical features, as reported in the literature, of BSS distributions at rectangular and trapezoidal channel sections, including the occurrence of inflection points caused by bottom vortices. The BSS is shown to vary across the bed width and sidewalls of the channel sections. The bed shear stress is relatively high in the large central portion of the bed width and drops rapidly toward the lower corners of the channel sections. The sidewall shear stress has a similar shape as the bed shear stress. The normalised bed shear stresses in the corner regions have different distributions between the trapezoidal channel and the rectangular channel section. Secondary flow in the channels are shown to cause BSS spatial fluctuations in the central portion of the channel-bed. The maximum BBS does not necessarily occur at the same location as the maximum primary velocity. As expected, the flow structures and turbulent shear stresses in the channel sections are sensitive to the presence of ice cover as well as to inflow disturbances.

The successful predictions are attributed to a proper implementation of no-slip conditions at the solid boundaries, as opposed to the use of uncertain estimates of solid surface roughness, and to an adequate representation of the viscous sublayer by the LES mesh used. It is crucial to allow mesh refinements adjacent to the bed and sidewalls as well as in the corner regions, and to ensure that the wall distance of the first node off a solid surface does not exceed unity, which is not the case in most of the existing LES applications to open-channel hydraulics. For the first time, this research thesis has explored practical LES strategies for accurate and efficient BSS predictions; these include the types of conditions imposed at the free surface and the ice cover underside, the lateral open boundaries at the upstream and downstream ends of a LES domain, and sensitivity tests. It has been demonstrated that the LES technique offers an attractive complement to laboratory measurements of BSS. With an exponential increase in computing power, it will eventually be feasible to perform LES for high Reynolds number flow in water channels.

ACKNOWLEDGEMENT

First of all, I would like to thank my supervisor, Dr. S. Samuel Li for his unfailing support and continuous encouragement. The door to Prof. Li's office is always open whenever I run into a problem or had a question about my research thesis. His invaluable guidance and abundant help are greatly appreciated. It has been an honor and a privilege working under the supervision of Dr. Li for the past two years. What I have learned is not only the knowledge related to this research thesis, but also the passion for one's work and life.

I would like to thank Ms. Azita Najafi-Nejad-Nasser for her help with the software.

I would like to thank the examiners Dr. A.S. Ramamurthy, Dr. L. Wang and Dr. M. Paraschivoiu, for their comments and suggestions.

This study would not have been possible without the financial support from the Natural Sciences and Engineering Research Council of Canada through Discovery Grants held by Dr. S. S. Li.

Finally, I would like to express my very profound gratitude to my parents and friends for providing me with endless happiness and inspiration throughout my study in Canada. This accomplishment would not have been possible without them. Thank you.

TABLE OF CONTENTS

List of Symbols

The following symbols have been used in this thesis:

A	Cross-sectional area of flow (m^2)
C	Constant of integration, or Courant number
C_f	Skin friction coefficient based on edge velocity, $C_f = \frac{2\tau_0}{\rho U_0^2}$
$C_{f,\text{bed}}$	Chézy friction coefficient
C_{ij}	LES cross-term tensor (m^2/s^2)
C_1	Constant developed from the log-law
C_L	Closure coefficient
C_s	Smagorinsky coefficient
d	Preston tube diameter (m), or distance from a control volume to the closest wall (m)
D	Flow domain
g	Gravitational acceleration (m/s^2)
g_i	Gravitational acceleration in tensor notation (m/s^2)
G	Gravitational force (m), or filter function
H	Flow depth (m)
k_0	Parameter related to per-unit-width discharge
L	Characteristic length (m)
L_{ij}	Leonard-stress tensor (m^2/s^2)
L_s	Characteristic length scale of subgrid-scale motion (mixing length) (m)
m	Mass of water (kg)
m_i, m_b	Parameters associated with ice and riverbed frictional effects
P	Static pressure (Pa)
P_0	Stagnation pressure (Pa)
$\overline{p}$	Resolvable pressure (Pa)
q	Velocity scale of the sub-grid scale motion (m/s)
Q	Discharge (m^3/s)
Q_{ij}	LES stress tensor, $Q_{ij} = C_{ij} + R_{ij}$ (m^2/s^2)

R	Hydraulic radius (m), or the radius of a pipe (m)
R_{ij}	SGS Reynolds stress tensor (m^2/s^2)
Re_L	Reynolds number based on characteristic length
Re_x	Reynolds number based on distance from the leading edge
S	Energy slope, or bed slope for uniform flows
S_{ij}	Resolved strain-rate tensor (s^{-1})
t	Time (s)
u, v, w	Instantaneous velocity components in x, y, z directions (m/s)
u', v', w'	Fluctuating velocity components in x, y, z directions (m/s)
u_i', u_j'	Subgrid-scale velocities in tensor notation (m/s)
$\overline{u}_i, \overline{u}_j$	Resolvable filtered velocities in tensor notation (m/s)
U, V, W	Reynolds-averaged velocity components in x, y, z directions (m/s)
U_i	Bulk mean velocity in tensor notation, i.e., averaged over the cross section (m/s)
U_0	Characteristic velocity over a flat plane (m/s)
U_e	Free stream velocity (m/s)
U_s	Depth averaged velocity (m/s)
U_a, U_b	Streamwise mean velocities at a distance of y_a and y_b from the wall (m/s)
U^+	Dimensionless, sublayer-scaled, velocity, $U^+ = \frac{U}{U_*}$
U_*	Shear velocity $U_* = \sqrt{\tau_0 / \rho}$ (m/s)
V	Volume of the computational cell (m^3)
x	Distance along the plate from the leading edge (m)
x, y, z	Rectangular Cartesian coordinates (m)
x_i, x_j	Position vectors in tensor notation (m)
x^+, y^+, z^+	Dimensionless wall distance in streamwise, vertical, lateral directions, $y^+ = yU_*/\nu$
y_a, y_b	Vertical distances from the wall (m)
γ	Specific weight of fluid (N/m^3)
δ	Thickness of viscous sublayer (m)
δ^*	Displacement thickness (m)
Δ	LES filter width (m)

ΔP	Mean pressure drop in a pipe or a duct (Pa)
Δt	Time step (s)
θ	Momentum thickness (m), or an angle of inclination to the horizontal
κ	Von Karman constant
μ	Dynamic viscosity of the fluid (Pa·s)
ν	Kinematic viscosity of the fluid, $\nu = \mu/\rho$ (m^2/s)
ν_τ	Smagorinsky eddy viscosity (m^2/s)
ρ	Mass density of the fluid (kg/m^3)
τ	Total shear stress (Pa)
τ_0	Shear stress at solid boundary (Pa)
τ_{ij}	Subgrid scale stress tensor (Pa), or shear stress anywhere in fluid in tensor notation (Pa)
τ_s	Sidewall shear stress (Pa)
τ_t	Reynolds stress (Pa)
τ_w	Bed shear stress (Pa)
τ_μ	Viscous shear (Pa)
$\bar{\tau}_0$	Mean boundary shear stress over a specific surface area (Pa)
$\bar{\tau}_{cb}$	Mean bed shear stress (Pa)
$\bar{\tau}_{cs}$	Mean sidewall shear stress (Pa)
$\overline{\Phi}(x)$	A filtered variable

List of Figures

List of Tables

1. Introduction

1.1 Background

Boundary shear stress, frequently referred to as the unit tractive force impacting channel stability, is an important parameter of open channel flow. When water flows in the channel, boundary shear stress forms on its boundaries as the pull of water acts on the wetted area in the direction of flow. The mean boundary shear stress, $\bar{\tau}_0$, can be estimated using the formula $\bar{\tau}_0 = \gamma RS$, where γ is the specific weight of water, R is the hydraulic radius, and S is the bed slope (Chow, 1959, p. 168). However, the local boundary shear stress along the wetted perimeter of an open channel is difficult to obtain because of its non-uniform characteristics.

The distribution of boundary shear stresses at the bed and on the sidewalls of an open channel is a fundamental element that must be accounted for in almost every river engineering project. A good understanding of the implications of boundary shear stress has many important applications such as monitoring sediment transport, channel stability, and fish habitats.

The local boundary shear stress is relevant when attempting to estimate the initiation of sediment motions and subsequent transport. Sediment transport is defined as "a phenomenon that water flowing in natural or artificial channels has the ability to scour sands, gravel, or large boulders from the bed or banks and sweep them downstream" (Henderson, 1966, p. 405). Also, knowledge of local boundary shear stress is of economic importance as it affects the design of hydraulic structures, the costs of a flood control scheme, and the storage capacity of a reservoir. The initiation of entraining stationary sediment particles from the channel-bed must satisfy the condition that the boundary shear stress exerted by the fluid exceeds the critical shear stress. However, merely estimating the mean boundary shear stress across an entire cross section is not a realistic method of predicting the initiation of sediment motions because this can underestimate sediment transport. Local shear stresses vary considerably from point to point. In addition, knowledge of local boundary shear stress across a cross section in open channel flows enhances our ability to accurately determine sediment transport capacity.

Boundary shear stress is widely accepted as an appropriate erosion criterion in stable channel design. For example, the tractive force method is often used to design erodible open channels based

on the use of boundary shear stress and sediment transport relationships (Akan, 2001). The size and type of materials used at different locations in the channel to protect the channel boundaries are determined by the distribution of boundary shear stress. An inappropriate channel design can lead to serious problems such as bank erosion and channel pattern changes.

Nearly all water contains some solid matter in suspension, which can be physical, chemical, or biological in origin. Birtwell (1999) suggested that elevated levels of sediments could be harmful to fish species because of the negative impacts on their habitats. Land erosion and sediment input to waterways can increase the amount of materials in suspension. As bank erosion is related to boundary shear stress distributions, the related knowledge is indispensable to the maintenance of stable fish habitats.

In attempts to better avoid undesirable difficulties related to hydraulic engineering applications, many researchers have investigated boundary shear stress distributions in water channels. However, a completely satisfactory theory that can predict boundary shear stress distribution has yet to be developed. Field investigations are difficult because they require a significant amount of labour and financial resources, most notably in ice-covered rivers, where environmental monitoring and research tend to be logistically challenging. Experimental measurements are sometimes inaccurate because of equipment deficiencies, and they are very expensive and time-consuming. Analytical methods usually use empirical coefficients based on specific experimental data. Generally, there are deviations in certain areas, such as the regions near channel corners and free surface. The numerical models derived from Reynolds-averaged Navier-Stokes equations usually neglect some turbulent transient characteristics. Both poor meshing techniques and the wall functions adopted in some numerical models can lead to inaccurate results. Therefore, there is a need for a more systematic discussion and elaborate description of the features of boundary shear stress distributions in channels with simple geometry. Moreover, there has been very limited research so far, dealing with boundary shear stress distributions in ice-covered conditions. This is virtually an unexplored area of hydraulic studies. Furthermore, the distribution of boundary shear stress at the channel-bed and on its sidewalls depends on the shape of the channel cross section, the structure of secondary flow, and the roughness of the solid boundaries. However, accurate estimates of roughness are difficult to obtain, which has hindered our ability to predict boundary

shear stresses. The use of no-slip conditions helps reduce prediction uncertainties. Large eddy simulation offers the hope to accurately capture the effects of secondary flow, which can only be estimated roughly in analytical models.

Last but not least, the critical condition of sediment movement is often overestimated if traditional sediment transport theories are applied to situations with high turbulence intensities. Hence, a thorough understanding of the issues related to the instantaneous distribution of local bed shear stress is also of importance. With LES technique, it becomes possible to obtain not only the distribution of boundary shear stress but also a deeper comprehension of instantaneous boundary shear stress.

LES technique was selected as the modeling approach in this research. The modeling technique is an efficient and economical way of exploring the distribution of boundary shear stress. In this research, each simulation only requires computing time of 10-30 hours thanks to the use of a supercomputer. The technique permits a systematic assessment of the effects of such factors as geometry, mesh size, and time step on prediction accuracy. It is possible to explore the details of turbulent characteristics near the channel boundaries in channels of various geometrical shapes.

Given the difficulties of attaining boundary shear stress distributions along the boundaries of channels of different shapes, is there a feasible numerical approach that avoids the inaccuracies of previous numerical studies while reducing expenses? What are the common features of boundary shear stress? What are the modeling strategies that allow for proper mesh and reasonable parameters? What are the differences in boundary shear stress distributions in open water versus ice-covered channels?

1.2 Objectives

We are interested in predicting the distribution of boundary shear stress without having to estimate the roughness of boundary surfaces. We expect that the results that are more accurate. We deal with both rectangular and trapezoidal open channels. We aim to improve our understanding of boundary shear stress distributed along the wetted perimeter of different channels. The specific objectives of this research are:

- to obtain LES predictions of boundary shear stress distributions in channels of various shapes under different flow conditions. This includes rectangular open channels, trapezoidal open channels, rectangular ice-covered channels, and trapezoidal ice-covered channels;
- to validate the LES predictions with available experimental results;
- to investigate effective meshing and parameter setup strategies for boundary shear stress simulations; and
- to systematically investigate the functioning of User Defined Functions (UDF), symmetry conditions, periodic boundary conditions, and the sweep technique (using hexahedral mesh with a specific length to height ratio) in LES.

1.3 Scope of this Research Work

To achieve the objectives mentioned above, the remaining part of the thesis is organised as follows. Chapter Two provides a summary of previous investigations of boundary shear stress using different approaches. The summary includes analytical, numerical, and experimental studies. It also includes field measurements of boundary shear stress. The chapter discusses five basic methods for determining the friction velocity (or equivalently the boundary shear stress). In addition, the graphical division method and depth-averaged method are discussed. The discussion covers the feasibility and accuracy of measurement apparatus, hydraulic parameters (e.g. velocity and mean boundary shear stress) in ice-covered channels.

Chapter Three describes the modelling methodologies used in this research thesis. The description gives details of the model domains, governing equations, choices of numerical techniques, associated parameters, boundary conditions, and initial conditions. This chapter also provides reasons for choosing LES and simulation strategies, which help enhance spatial resolutions with lower computing costs.

Chapter Four presents LES results for rectangular and trapezoidal channels under open water and ice-covered conditions. The results presented include bed and sidewall shear stresses as well as velocity contours and profiles. The results correspond to a selection of the amount of nodes, mesh dimensions, and model time period. The predicted boundary shear stresses are compared with experimental results.

Chapter Five gives conclusions based on this LES study and suggestions for further investigations of boundary shear stress in water channels.

1.4 Contributions

A number of contributions have been made through this study, as outlined below:

1) This study has filled a knowledge gap in shear stress distributions in ice-covered channel boundaries.
2) It has contributed to the establishment of effective LES strategies for reliable predictions of turbulent channel flow.
3) This LES study offers an attractive complement to physical models, laboratory experiments, and field measurements.

2. Literature Review

2.1 General

The distribution of boundary shear stress along the wetted perimeter of a channel is very complicated. It depends on many factors, such as the shape of channel cross section, the size and distribution of secondary flow cells, and the wall roughness. Section 2.2 will review five basic methods for determining the boundary shear stress.

Since the 1930s, many researchers have made theoretical investigations of the distribution of the boundary shear stress. They proposed the concepts of dividing the channel cross section into many sub-sections or three different regions. Since then, some researchers have brought new ideas based on various hypotheses. They have extensively employed two-dimensional (2D) depth-averaged approach before realizing the significance of secondary flow structure. Other methods such as the Vorticity Equation Method, the Laminar Flow Solution Method, and the Turbulent Kinetic Energy Method, have been developed in the past few decades. Section 2.3 will show details related to this topic.

Numerical predictions appear to be a future trend. Research contributions in this area will be elaborated in Section 2.4. The framework of the discussion is based on different types of turbulence models employed such as Reynolds-averaged Navier-Stokes (RANS) based turbulence models, the Direct Numerical Simulation (DNS), and the Large Eddy Simulation (LES) technique.

This review intends to present some significant laboratory measurements about local boundary shear stress in open channels. Numerous researchers have implemented flume measurements in the past, but only those focusing on distributions of shear stress in simple open channels will be reviewed in Section 2.5.

Field measurements have always been prevalent. It is hard to measure the boundary shear stress directly in rivers. The estimation of boundary shear stress relies on the observation of velocity profiles. Researchers have used different apparatus to obtain realistic data. Section 2.6 summarizes typical field studies.

Studies of ice-covered channels will be reviewed in Section 2.7. Several researchers have studied velocity profiles, the estimation of discharge, and mean boundary shear stress values under the ice-covered condition, but only limited work is related to distribution of the local boundary shear stress in ice-covered channels.

2.2 Basic Methods for Determining Boundary Shear Stress

The friction velocity U_* is defined as:

[2.1] $$U_* = \sqrt{\frac{\tau_0}{\rho}}$$

where τ_0 is shear stress at a solid boundary, ρ is the density of water. Many approaches utilize this equation to convert the shear velocity to the boundary shear stress.

Nezu and Nakagawa (1993, p. 48-49) enumerated various basic methods, which are summarized in the following sub-sections, to determine the friction velocity.

2.2.1 Estimation from Channel Slope

The shear stress at the boundary can be obtained from the channel slope S, under the conditions of normal and uniform flow, and the relationship is:

[2.2] $$\tau_0 = \gamma RS$$

where γ is the specific weight of the water, τ_0 is the shear stress at solid boundary, and R is the hydraulic radius (Henderson, 1966, p. 91). Equation [2.2] expresses the simplest way to obtain the boundary shear stress based on the condition that the gravitational force of the water is equal to the friction drag along the channel, and there is no acceleration of flow. As a result, the shear stress obtained here is a unit tractive force over the unit wetted perimeter, which is a typical way to calculate the shear velocity several decades ago (Raichlen, 1967; McQuivey & Richardson, 1969).

In 2D flow, if the channel width is sufficiently large compared to the depth especially for shallow rectangular channels, R in Equation [2.2] is replaced by the flow depth H as:

[2.3] $$\tau_0 = \gamma HS$$

The shear stress in Equation [2.3] is proportional to the flow depth, leading to the Vertical Depth Method. Shear stress can also be assumed to be proportional to the area between two verticals (Vertical Area Method). If the transverse slope of the channel-bed is steep, it is better to use the depth perpendicular to the channel-bed (Normal Depth Method). A corresponding method to vertical area method in transverse steep channels is called Normal Area Method, in which shear stress is proportional to the area between two perpendiculars. These methods cannot provide satisfactory results in deep channels or channels with a steep slope (Khodashenas & Paquier, 1999). Furthermore, these methods have significant errors at places near the free surface or the corners of channel boundary (Yu & Tan, 2007).

2.2.2 Estimation from the Logarithmic Law

Shear velocity U_* can be evaluated from the logarithmic law. Equation [2.4] is the 'log-law' formula, derived by Von-Karman (Keulegan, 1938). This equation, also called Prandtl-Karman logarithmic velocity distribution equation, can be expressed as:

$$\frac{U}{U_*} = \frac{1}{\kappa}\ln\left(\frac{yU_*}{\nu}\right) + C \quad (30 < y^+ < 200) \tag{2.4}$$

where U is the streamwise Reynolds-averaged velocity at a distance of y from the wall, ν is the kinematic viscosity of water, κ is the von Karman constant, C is a constant of integration, and y^+ is the dimensionless wall distance. In Chapter 2, (x, y, z) are rectangular Cartesian coordinates and denote the streamwise direction, the vertical direction, and the spanwise direction.

The velocities are not uniformly distributed in the channel section due to the existence of free surface and the friction along the channel walls. There are many other factors, which affect the velocity distribution in a channel section, such as the unusual shape of the section, the roughness of the channel, and the presence of bends. Therefore, the constants in Equation [2.4] will change accordingly with the applied conditions.

Regardless of whether the boundary is acting smooth, transitional or rough, the logarithmic Equation [2.4] can be restated as:

$$\sqrt{\frac{\tau_0}{\rho}} = U_* = \frac{1}{C_1}\frac{U_b - U_a}{\log(y_b / y_a)} \tag{2.5}$$

where U_b and U_a are streamwise mean velocities at a distance of y_a and y_b from the wall, respectively; y_b and y_a denote the distance from the wall at two different locations, and C_1 is a constant. The shear velocity can be estimated using a known Reynolds-averaged velocity profile. The local shear stress distribution on the boundary can, therefore, be calculated based on two or more measured velocity points. One of the applications of this idea is the Clauser Plot Method, which involves drawing the right-hand quotients on a semi-logarithmic paper (Section 2.5.1.2).

2.2.3 Estimation from Reynolds Stress Distribution

Boundary shear stress can be determined from the measured Reynolds Stress distribution. For fully developed turbulent channel flow, the total shear stress τ is given by:

[2.6] $$\frac{\tau}{\rho} = U_*^2\left(1-\frac{y}{H}\right) = -\overline{u'v'} + \nu\frac{\partial U}{\partial y}$$

where H is the flow depth, and u' and v' are fluctuating velocity components in x, y directions. The total shear stress varies linearly from the shear stress value τ_w at the bed to zero at the free surface.

The thickness of the viscous sublayer δ can be determined by (Fox & McDonald, 1992, p.343):

[2.7] $$\delta = \frac{y^+\nu}{U_*} \qquad (\text{for } y^+=5)$$

Reynold's stress ($\tau_t = -\rho\overline{u'v'}$) rather than viscous shear ($\tau_\mu = \mu\frac{\partial U}{\partial y}$) is dominant over the entire center region of a pipe, or rather, the outer region of sublayer. The total shear stress is expressed as:

[2.8] $$\tau = \tau_t = -\rho\overline{u'v'} \quad (\delta < y < H)$$

When approaching close to the wall (within the viscous sublayer), the viscous shear is dominant due to the viscosity, giving:

[2.9] $$\tau = \tau_\mu = \mu\frac{\partial U}{\partial y} \quad (0 < y < \delta)$$

where μ is the dynamic viscosity of water.

If Reynold's stress ($\tau_t = -\rho\overline{u'v'}$) is measured near the boundary but outside the region of viscous sublayer, the boundary shear stress is approximately equal to the value of Reynolds stress (Figure 2.1) as:

[2.10] $$\tau_0 = \tau_t = -\rho\overline{u'v'} \ (\delta < y)$$

This method is the most appropriate for research in turbulent flow because it incorporates fluctuating velocity. However, it is challenging to get data at such a close distance to the solid boundary (Nezu & Nakagawa, 1993, p 49).

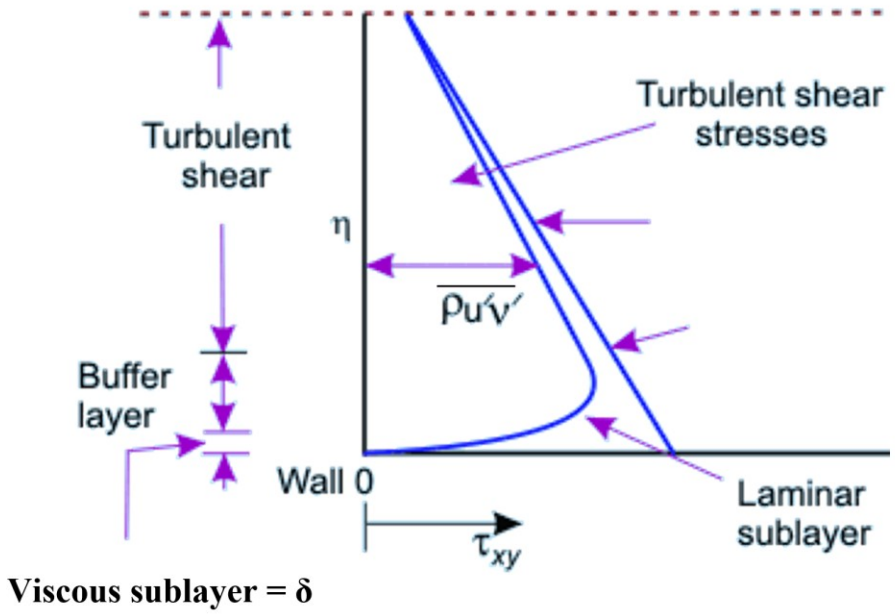

Figure 2.1 Distribution of turbulent shear stress along a wall (Fox & McDonald, 1992, p. 342)

2.2.4 Estimation from Velocity Distribution in Sublayer

Similar to the method discussed in Section 2.2.2, if a viscous sublayer exists in the velocity profile, shear velocity U_* can be determined from the velocity distribution in that region, with the aid of:

[2.11] $$\frac{U}{U_*} = \frac{yU_*}{\nu} \quad \text{or} \quad U^+ = y^+ \quad (\text{for } 0 \le y^+ \le 5)$$

where U^+ is the dimensionless velocity. Equation [2.11] has been obtained by integrating Equation [2.9].

When the mesh is fine enough to resolve the viscous sublayer in LES, the wall shear stress is obtained from this relationship (ANSYS, 2013a).

2.2.5 Estimation from Preston Tube

According to Preston (1954), the dynamic pressure $\frac{1}{2}U^2$, measured using a pitot tube of a given geometrical shape, was a universal function of boundary shear stress. The original relation suggested by Preston (1954) was:

[2.12] $$\frac{(P_0 - P)d^2}{\rho\nu^2} = f(\frac{\tau_0 d^2}{\rho\nu^2})$$

where P is the static pressure at a point in the flow, P_0 is the stagnation pressure at the same point, and d is the tube diameter. Preston (1954) measured the total pressure at the boundary with a pitot tube, where the dynamic pressure $\frac{1}{2}U^2$ is zero, and the static pressure at the same location, using pressure tap in the pipe. Subsequently, researchers combined the measurements of static pressure and stagnation pressure into one instrument called Pitot-static tube and applied it to an open channel flow.

Equation [2.13] describes the velocity profile when the Pitot tube is placed in a region where the log-law holds. A schematic of the typical Pitot-static tube is shown in Figure 2.2. Stagnation pressure P_0 is measured at point B through the inner tube, while the static pressure P at point C is sensed by small holes in the outer tube. Based on Bernoulli equation, the local flow velocity can be estimated from the pressure difference between the stagnation pressure and the static pressure by a pitot tube (Equation [2.14]) (Thornton, Cox & Sclafani, 2008). To obtain Equation [2.12], Equation [2.1] and Equation [2.14] are substituted into Equation [2.13], and dimensionless analysis is then used.

[2.13] $$\frac{U}{U_*} = f_1(\frac{yU_*}{\nu})$$

[2.14] $$U = \sqrt{\frac{2(P_0 - P)}{\rho}}$$

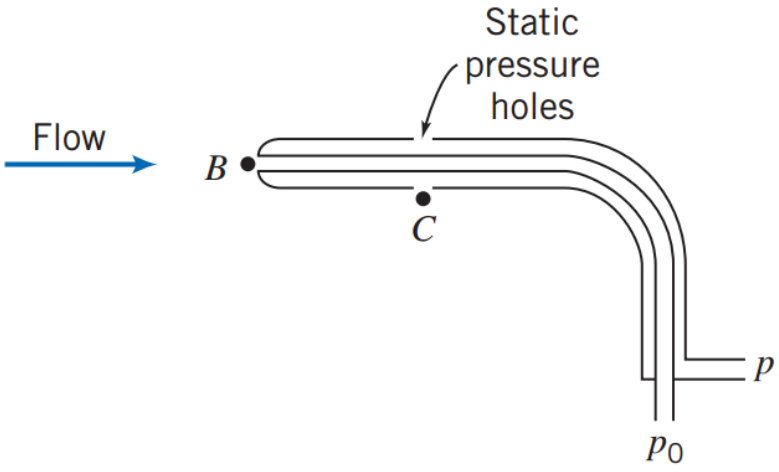

Figure 2.2 A schematic of the typical Pitot-static tube (Thornton et al., 2008)

For relatively thick turbulent wall flows and tiny tubes, the measurement could be fully immersed in the viscous sublayer. In this case, the Reynolds-averaged velocity profile in Equation [2.13] across the tube opening will be linear. In most cases, the finite wall thickness of a typical tube will result in the location of the tube opening being primarily in the logarithmic portion of velocity profile. It is for these situations that the majority of Preston tube calibrations have been developed.

Calibration of Preston tube is necessary for the relationship to be applicable in a more general sense, and it requires to collect velocity data near the bed in the channel with known boundary shear stress. Both Preston (1954) and Patel (1965) calibrated Preston tubes using data from pipe flow. Ferriss (1965) used channel flow data, and Zarbi and Reynolds (1991) used data from boundary layer to perform calibrations for a Preston tube. Though invented several years ago, this apparatus is still widely used by many researchers in present studies to obtain the local shear stress (Ghosh & Roy, 1970; Chanson, 2000; Kean, Kuhnle, Smith, Alonso & Langendoen, 2009).

Many factors have influences on the accuracy of a Preston tube. The technique is inappropriate for highly non-equilibrium wall flows or other situations where the logarithmic velocity profile has been significantly altered. The ratio of inner to outer diameter of Preston tube is also an important parameter (Patel, 1965). Moreover, alignment of the Preston tube in the flow direction can be a significant source of error, especially in three-dimensional (3D) boundary layers where the mean flow direction is not always easy to determine. Lastly, care must be taken to ensure that the flow

at the static pressure port is not influenced by the presence of wall or other interferences. Applications that are more practical are discussed in Section 2.5.1.1.

2.3 Theoretical Effort

2.3.1 Graphical Division by Ray-isovel Approach

Leighly (1932) was the first to obtain the boundary shear stress distribution on natural open channel boundaries using the Ray-isovel Approach. This graphical division approach divides the channel cross section into many subsections by lines (rays) that are perpendicular to the isovels. The rays extend from the channel boundaries to the maximum isovel, meaning that water above maximum velocity line is not contributing to the boundary shear stress. This approach involves the conformal mapping technique, also called conformal transformation, which is a transformation that preserves local angles.

By neglecting the effects of secondary currents, it is found that the boundary shear stress acting on the channel-bed must be balanced by the downstream component of water weight contained between each of two adjacent orthogonal rays. The shear stress on a unit area can be calculated by:

[2.15] $$G = mgS$$

where G is the gravitational force, m is the mass of water between two rays, and g is the acceleration of gravity. For a non-uniform flow, S should be replaced by the hydraulic slope. It is the same method summarized in Section 2.2.1, but the idea of graphical division using isovels is the first time shown in the world.

The distribution of boundary shear stress in an open channel obtained by Leighly (1932) is shown in Figure 2.3. It showed the maximum bed shear stress values on the channel-bed are near the base of steep sides rather than near the centerline of flat channel-bed. However, there is no trend of a dramatic drop of boundary shear stress when approaching the corners. In general, this proposal did not render any conclusive results, but it is considered a significant inspiration to other researchers (Graf, 1984).

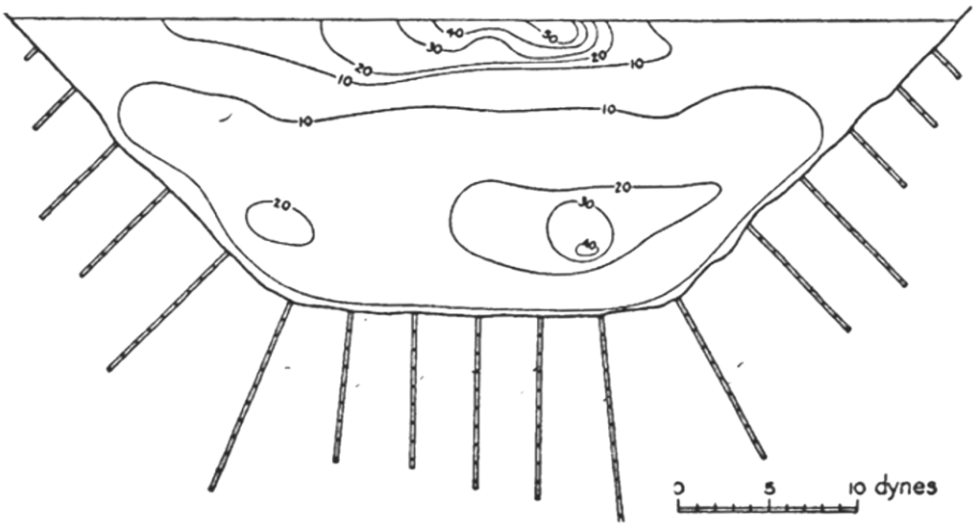

Figure 2.3 The distribution of boundary shear stress in an open channel obtained by Leighly (1932)

The velocity distribution is the prerequisite for the graphical division approach. Chiu and Lin (1983) developed a mathematic modeling technique (numerical model) to simulate the velocity distribution. The simulated flow isovels were then used as a new coordinate system (Figure 2.4) to obtain boundary shear stress and secondary flow distributions covering the entire boundary of a channel bend. It is concluded that the location of the maximum boundary shear stress is not necessary to be the same as the maximum primary velocity. Large discrepancies were found in the prediction of secondary flow distribution because some model coefficients were computed using measured data.

Subsequently, Chiu and Chiou (1986) extended the model to rectangular open channels. In a given channel cross section, the turbulent shear stress on the rays is zero. They investigated the boundary shear stress under various Manning's roughness, aspect ratios (the ratio of the width to the depth of the channel cross section), and the slope of channel. The results disagree with the experimental data on the boundaries.

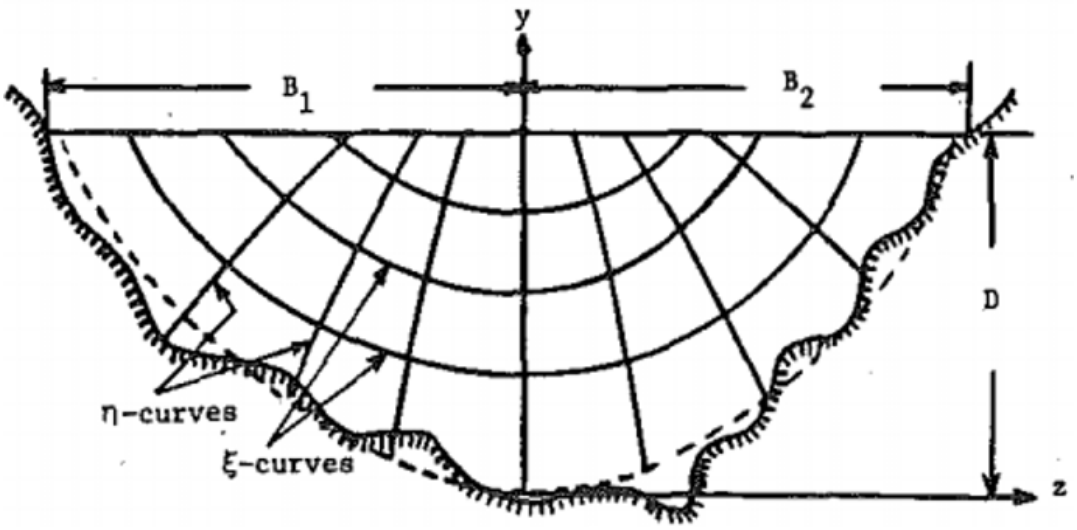

Figure 2.4 Primary flow velocity distribution and ξ-η coordinate system (Chiu & Lin, 1983)

Houjou and Ishii (1990) developed another method for determining the distribution of velocity based on the assumption that a scalar eddy viscosity is proportional to the shear velocity in each subsection when using the Ray-isovel Approach. The 2D momentum equations proposed by this model were solved numerically, and the boundary shear stress distribution was computed for a rectangular open channel flow. They confirmed that the roughness and the aspect ratio have an influence on the flow structure. In addition, they found a slight difference of bed shear stress with the experimental results near the corners due to the lack of secondary flow effect in the model.

The importance of secondary flow was detected by Kean and Smith (2004) and Kean et al. (2009). They adopted the turbulent closure technique from the model of Houjou and Ishii (1990). The velocity and boundary shear stress distributions were predicted in channels with banks and floodplains protected by woody vegetation (Kean & Smith, 2004) and rough cobbles (Kean et al., 2009). Principal differences between measured and calculated fields are caused by the lack of secondary circulation effects. This is because better agreement between their model and experimental results can be achieved by distorting the calculated flow field with measured secondary flow data.

Yu and Tan (2007) used a flow-net method to obtain the boundary shear stress, based on the assumption that the energy production balances its dissipation within each sub-area partitioned by two adjacent potential lines. The flow-net method is essentially the same as the Ray-isovel

Approach, in which the wetted cross section was mapped by orthogonal streams (rays) and potential lines (isovels). The only difference with the Ray-isovel method is that the ends of the potential lines are located at the imaginary boundary on the free surface instead of the maximum velocity contour. Numerical experiments were carried out to determine this imaginary boundary. This model was applied to circular, rectangular, trapezoidal, and compound channels. Reasonable agreements with experimental data were shown even near the water margins and corner regions, except for locations with sharp corners and protrusions, such as the step-bank of floodplain. The omission of the secondary flow effect leads to general overestimation of the boundary shear stress. Since the secondary flow cells strengthen the flow and energy exchange, they can average the boundary shear stress distribution.

Knowledge of primary velocity distributions is required for the Ray-isovel technique. Going forward, proper implementation of the secondary flow effect into the model will be of interest. To summarize, despite the fact that Graphical division using the Ray-isovel Approach is simpler than the CFD technique, the model using Graphical division technique is still a useful tool to determine the distributions of velocity and boundary shear stress in complex channels. The Graphical division technique substantially requires less computational efforts than fully 3D flow models (Kean & Smith, 2004).

2.3.2 Graphical Division by Hydraulic Radius Separation Approach

There is another way to achieve the graphical division dating back to the 1930s. Keulegan (1938) proposed to separate the flow cross section area into three sections in order to find an expression for the bulk mean velocity of each subsection, which is the flow rate averaged over the area of each section. The cross section was divided using the bisectors of base angles for a polygonal channel. However, the reason to choose bisectors as division lines is not explained.

As shown in Figure 2.5, Einstein (1942) developed another method for partitioning the flow cross section into different parts using two sidewalls and a channel-bed through the consideration of isovel pattern. It is assumed that the bulk mean velocitiy in each section are the same without any explanation. As a result, the shear force on the bed could be separated from the lateral boundaries.

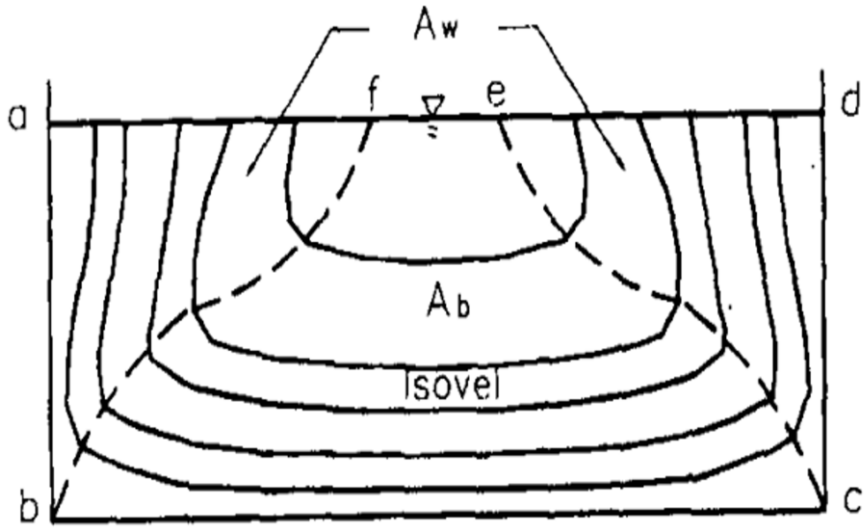

Figure 2.5 Partitioning of flow cross section by Einstein (1942)

The mean boundary shear stress is calculated using the basic method mentioned in Section 2.2.1 in relation to the energy slope (Equation [2.2]).

Each mean boundary shear stress needs its hydraulic radius estimated by the area of each section divided by its wetted perimeter. There is no friction at the interface between the areas. The potential energy in each section is dissipated by the related boundary, respectively. Therefore, this graphical division approach is named as the Hydraulic Radius Separation Approach, which is still widely used together with laboratory studies.

Yang and Lim (1997, 1998) developed an analytical method for demarcating the locations of division lines in Einstein's work. The equations are corresponding to the channel shape, aspect ratio and roughness distribution on the wetted perimeter. A design of separation lines with the steepest descent between the core flow region and the channel corners were generated. The division lines were straight with zero stress (Figure 2.6). Only the mean boundary shear stress was obtained with poor quality within rectangular cross sections.

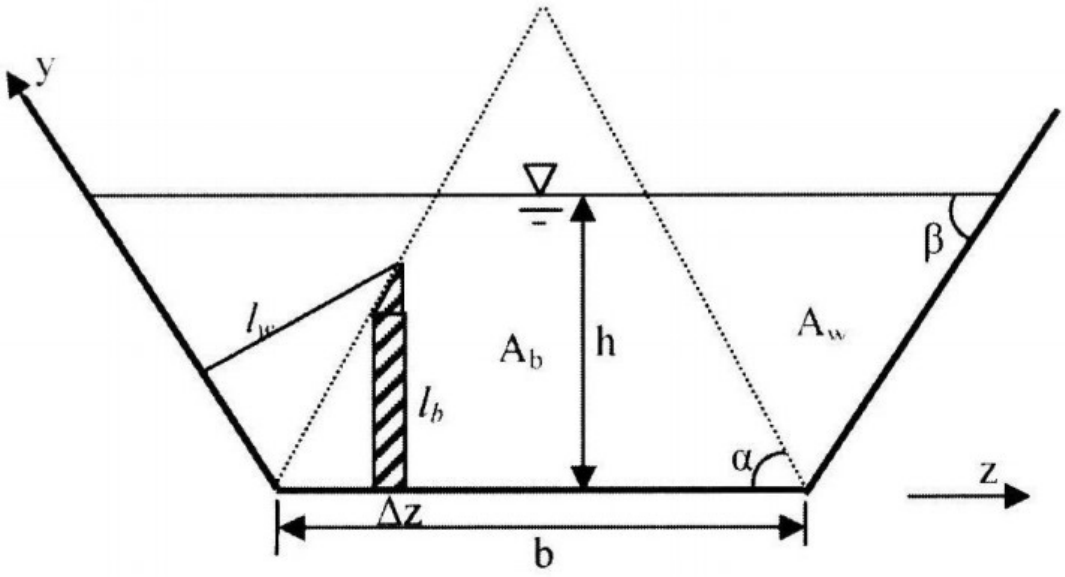

Figure 2.6 The intersection of straight division lines above the free surface (Yang & Lim, 2005)

The model was used to obtain the boundary shear stress distributions in smooth rectangular channels (Yang & McCorquodale, 2004) and rough trapezoidal open channels (Yang & Lim, 2005). Yang and McCorquodale (2004) applied an order of magnitude treatment to the Reynolds equations. Analytical solutions of boundary shear stress distribution were developed by integration under different conditions. The solutions involving the secondary current effect, using empirical coefficients based on known data, gave better results compared to the rest. However, the local boundary shear stress at corner regions on the channel-bed is incorrect, and the equations do not incorporate the geometry of the channel, which is not ideal. Yang and Lim (2005) developed three equations to describe the shear stress distributions in various sub-sections, where there is no effect of secondary flow. It is found that the local boundary shear stress at the free surface is zero, and the maximum values (peak point) on the sidewalls approaches to the bed as the base angle increases. Furthermore, near corners, the values of sidewall shear stress are not correct.

A new method for partitioning the channel cross section in rectangular channels has been developed by Guo and Julien (2005). Analytical equations were developed for the delineating lines. Two empirical correction factors were introduced for secondary current and eddy viscosity to reduce the overestimation of experimental data. De Cacqueray, Hargreaves and Morvan (2009) used the CFD technique to calculate the various terms in the equations proposed by Guo and Julien

(2005). The internal shear and secondary currents are important to get the local shear stress. The division methods of Keulegan (1938) and Yang and Lim (1997) were proven to be equivalent. It is postulated that Guo and Julien's formulas could potentially be used for any division line approach.

Kabiri-Samani, Farshi and Chamani (2012) derived semi-analytical equations to obtain boundary shear stress distributions in the best hydraulic trapezoidal sections (the cross section with the maximum hydraulic radius) based on the methodology of Guo and Julien (2005). The locations of maximum velocity and maximum shear stress were also found to be inconsistent.

Several graphical division methods are summarized above. Correction coefficients were used to express the secondary current effect. However, the methods employing these coefficients gave bad results near the channel corners. Methods that are more effective are needed to account for the secondary flows.

2.3.3 Shiono and Knight Method (SKM)

A 2D approach based on the depth-averaged Navier-Stokes equations for uniform steady flows has been proposed (Knight, Shiono & Pirt, 1989). This method, often called Lateral Distributional Method (LDM), involves dividing the area of cross section vertically into some slices and solving the depth-averaged Navier-Stokes equations over the slices.

One of the LDMs called SKM is often used to obtain the shear stress distribution in channel flow. Shiono and Knight (1991) developed this analytical model in compound channels to get the depth-averaged velocity across the channel. The boundary shear stress and the discharge can be calculated from the velocity distribution by Darcy-Weisbach equation and numerical integration, respectively. Three hydraulic parameters related to the bed friction factor, the lateral eddy viscosity, and the depth-averaged secondary flow are considered in this method.

These parameters have been studied by different researchers. Ervine, Babaeyan-Koopaei and Sellin (2000) replaced the depth-averaged secondary flow parameter by a coefficient accounting for the impact of complex 3D mixing processes. Castanedo, Medina and Mendez (2005) proposed

different forms of the terms used to express the lateral distribution of turbulent shear stress in depth-averaged momentum equations. Sharifi, Sterling and Knight (2009) developed an algorithm to study the lateral variation of friction factor.

The prediction of depth-averaged velocity and discharge in natural rivers (Knight et al., 1989), the identification of mechanisms that influence the variation of bed shear stress (Sofialidis & Prinos, 1998), and the prediction of stage-discharge relationship for rivers in flood (Abril & Knight, 2004) have been investigated by numerous researchers using the SKM. The SKM was also applied to over-bank flow in straight rectangular compound channels (Tang & Knight, 2008). It was shown that this model gave better results in slightly shallower channels.

Knight, Omran and Tang (2007) presented a simple model to predict the depth-averaged velocity and the boundary shear stress distribution in trapezoidal channels based on the SKM. The predictions sometimes disagreed with the experimental data despite obtaining accurate averaged streamwise velocity because the secondary cells were modeled inappropriately.

On the one hand, the SKM is physically sound to give depth-averaged velocity and boundary shear stress distributions along the wetted perimeter. It can be regarded as an alternative method to the relatively traditional CFD approach, offering results for practical problems with much less computational effort and expense than CFD models. On the other hand, the SKM is essentially a simple one-dimensional (1D) approach with some 3D features, which means it is only useful for solving certain types of fluvial problems (Knight, Tang, Sterling, Shiono, & Mc Gahey, 2010) or steady flows analyses in prismatic flow (Rezaei & Knight, 2009). It is not effective in predicting the distribution of boundary shear in corner regions where the secondary flow effect is powerful.

2.3.4 Vorticity Equation Method

Zheng & Jin (1998) presented a semi-analytical approach to describe the lateral boundary shear stress distribution. It is applicable for the corner regions of rectangular ducts and open channels, but only the boundary shear stress in the corner regions can be determined. It was confined to a range of 0.5 H (rectangular ducts) to 0.65 H (rectangular channels). 'H' represented the flow depth of the ducts and channels. The results agree well with the experimental data in the corner region.

The effect of secondary flow on the lateral distribution of boundary shear stress was incorporated into the model. Prandtl's momentum transfer model was utilized to model the contribution of secondary flow to the transverse turbulent shear stress. The measured data of boundary shear stress in square ducts were used to quantify some empirical coefficients in the model.

Jin, Zarrati and Zheng (2004) used this model to calculate shear stress distributions in triangular ducts, rectangular and trapezoidal open channels. This model was able to predict shear stress distributions along the whole channel banks only in the trapezoidal cases by treating the free surface as a plane of symmetry.

Zarrati, Jin and Karimpour (2008) studied distributions of boundary shear stress in straight open channels, including rectangular, trapezoidal and compound cross sections. Different terms of the simplified vorticity equation were modeled and evaluated based on previous work and experimental data. Zarrati et al. (2008)'s work is an extension of the work of Zheng and Jin (1998). They thought to separate the wetted periphery into a corner region and an outer region that is not affected by the secondary flow. Equations for the distributions of boundary shear stress were obtained for both regions instead of only the corner regions. However, derived equations incorporating the secondary flow effect still included unknown coefficients, which were calculated based on boundary conditions and known experimental data. This model was proven to give bad results in the study of Kabiri-Samani et al. (2012). The deficiency of this model was considered as the consequence of the inappropriate graphical division technique without considering Einstein's idea mentioned in Section 2.3.2.

2.3.5 Laminar Flow Solution Method and Turbulent Kinetic Energy Method

In this section, other techniques to obtain the local shear stress are summarized. The Laminar Flow Solution Method was considered as a rough estimation of boundary shear stress. Estimation of local shear stress from turbulent kinetic energy yields unsatisfactory results.

2.3.5.1 Laminar Flow Solution

A solution to the laminar flow equations was found a long time ago. Olsen and Florey (1952) came up with an idea to apply the simplified laminar solution to the turbulent flow problem. Velocity

and shear stress distributions in a channel were expressed mathematically in the form of a partial differential equation. An analytical solution of this equation was a sum of a particular integral and a complementary function. Since the governing equation was taken as a 2D linear partial differential equation, it was considered well suited to the Finite Difference Method. Secondary flow effects were not deemed to obtain velocity distribution in the computed results, which caused discrepancies in the location of maximum velocity.

There was a slight discrepancy in the analytical solution due to using only three terms in an infinite series to obtain the complementary function. Since no experimental results were presented in the study, the results achieved by these methods were not convincing.

2.3.5.2 Turbulent Kinetic Energy

Tidal environment studies led to another method for obtaining the boundary shear stress distribution. Hopkinson and Wynn-Thompson (2012) examined the validity of a relationship in open channels that boundary shear stress is proportional to the turbulent kinetic energy (TKE) with a coefficient along sloping vegetated streambanks.

Experiments were conducted to obtain boundary shear stress in a sloping streambank. The coefficient was calculated using both measured boundary shear stress and boundary shear stress estimated from Reynolds stress. It is concluded that models based on Reynolds stress underestimated the boundary shear stress by a factor of three, because velocity data cannot be obtained very close to a boundary. In general, calculating the boundary shear stress based on the TKE led to a significant error in stream environments.

1D and 2D analytical models have been used to compute the open channel flow extensively. However, the lateral momentum transfer and the secondary circulation mean that the flows are highly 3D. Therefore, considerable difficulties would be encountered with the use of simple models (Krishnappan & Lau, 1986). The 3D numerical modeling could be a better complement to the experimental work since extensive numerical models could solve the sophisticated influential factors properly.

2.4 Numerical modeling

Accurate calculations of boundary shear stress in channels of arbitrary and complicated cross section geometry require the use of numerical methods. With the advent of high-speed computers, the studies of 2D and 3D flows in open channels have experienced a surge of interest in recent years. The potential to apply CFD techniques in such studies shows a promising prospect in terms of modeling and detailed flow analyses. Various models such as k-ε model, k-ω model, Reynolds Stress Model (RSM), Large Eddy Simulation (LES), and Direct Numerical Simulation (DNS) have been developed to simulate the complex flow structure in open channels. However, only a few researchers have focused on the distribution of boundary shear stress.

2.4.1 RANS based Turbulence Models

In turbulent flow, the quantities in governing equations can be decomposed into a mean part and a fluctuating part. The Reynolds-averaged Navier-Stokes (RANS) equations govern the mean flow. However, the velocity fluctuation appears in the form of Reynolds stress in the equations. The objective of turbulence models for RANS equations is to compute the Reynolds stress, so that the turbulence closure can be achieved. There are three main categories of RANS models: linear eddy viscosity models, non-linear eddy viscosity models, and the Reynolds Stress Model (RSM).

2.4.1.1 Linear Eddy Viscosity Models

In linear eddy viscosity models, the Reynolds stress is modeled by a linear relationship with the mean flow strain rate, known as the Boussinesq eddy-viscosity approximation. Depending on the number of transport equations needed to solve the eddy viscosity, the linear eddy viscosity models are composed of algebraic models (zero equation model), one-equation models, and two-equation models.

By far, the most popular two-equation model until the last decade of the twentieth century was the k-ε model. Straight compound channels have been extensively studied to understand turbulent flow behavior and to develop an accurate prediction method for the conveyance capacity. Krishnappan and Lau (1986) applied the 3D k-ε model to calculate shear stress distributions in asymmetric channels with compound cross sections. The maximum values of local shear stress are in the middle of the channel-bed and at the intersection of the floodplain and the main channel. No sign

of zero boundary shear stress can be found on the corner of the main channel because the calculating node picked in this research thesis was possibly not close enough to the wall.

The resolution of turbulence vertical distribution is rarely of interest in most cases in practical applications (Keller & Rodi, 1988). Therefore, a depth-averaged model was used in combination with the turbulence k-ε model to calculate the depth-averaged turbulent shear stress. Velocity and bed shear stress data taken from the literature in channels of compound cross sections were used to calibrate the model. The discrepancies of the predicted boundary shear stress and the experimental data was up to 15%. Errors arise when the model was used to predict flood events very different from the calibration data.

A 3D finite-volume model was used to predict the flow field in straight compound channels with the standard k-ε model (Rameshwaran & Naden, 2003). The boundary shear stress at the corner region in the main channel was not well predicted due to the significant secondary flow effects. Moreover, the predicted boundary shear stress was slightly over the experimental data at the main channel-bed far from the corners. The calibrated roughness height for a uniform flow simulation varies with flow depth, which reflects the fact that the interaction between the main channel flow and the floodplain flow was inadequately modeled with the standard k-ε model.

The free surface mentioned in the above cases was fixed or using rigid-lid assumption. Jazizadeh and Zarrati (2008) presented 3D shallow water equations to calculate flow in asymmetric compound channels with the help of a 3D k-ε model. The depth of the flow was divided into several layers, and governing equations were integrated over the thickness. The free surface level was then computed using the continuity equation and depth correction algorithm. They found a difference of 12% in velocity distribution with experimental data at the interaction region where the main and floodplain meet. Nevertheless, inflection points were shown in the distribution bed shear stress in the main channel near the corner, due to the effect of the bottom vortices. However, their locations were not correctly predicted because of the essential deficiency of the linear model.

The results obtained from the studies discussed above were all compared with experimental results in fair agreement and applied to specific conditions.

Zero-equation models, in which the eddy viscosity is prescribed as a function of channel depth, are more economical compared to complicated models, but they are unqualified as predictive tools for turbulent flows. This is because the function will vary from flow to flow, and from one cross section to the next. Two-equation models are inappropriate for predicting the occurrence of a secondary motion in cross-stream planes. Moreover, they do not reproduce the effects of the free surface on the turbulence structure. Therefore, models that are more sophisticated are required to accurately simulate the effect of secondary flow.

2.4.1.2 Nonlinear Eddy Viscosity Models

The eddy viscosity from the Boussinesq approximation depends on many factors, such as the shape of channel boundaries, the freestream turbulence intensity, and the flow-history effects. The flow-history effects on the Reynolds stress often persist for a long distance. Thus, the linear relationship is not reliable in some applications. Generally speaking, linear eddy viscosity models are not suitable for the following typical applications: flow with sudden changes in mean strain rate, flow over curved surfaces, flow in ducts with secondary motions, flow in rotating fluids, and 3D flows (Wilcox, 2006, p. 306).

One approach to approximating the Reynolds stress without introducing any additional differential equations is to use the Boussinesq approximation, which deals with only the leading term in a series expansion of functions. On this basis, numerous researchers have developed relations of different complexity, such as the nonlinear k-ε model and the Algebraic Stress Model (ASM). In the nonlinear k-ε model, the adding terms are solved using algebraic relationships, whereas for the ASM approximates, the convective and turbulent terms in the new Boussinesq approximation are resolved in the full Reynolds-stress equation as proportional to corresponding terms in the equation for the turbulence kinetic energy.

Turbulent flow in compound open channels was studied numerically with nonlinear k-ε turbulence models of Low-Reynolds type by Sofialidis and Prinos (1998). Most of the models at the same period were designed for High-Reynolds turbulence and wall functions were applied at the first node adjacent to the walls. Sofialidis and Prinos (1998) integrated the governing equations down

to the walls resolving the viscous sublayer. At each solid boundary, at least five nodes were located in the region with dimensionless wall distance smaller than two. Overestimations can be seen all over the channel-bed. In addition, the sharp corner region on the floodplain is not well estimated.

The Algebraic Stress Model (ASM) was applied to asymmetric compound rectangular open channels (Naot, Nezu & Nakagawa, 1993). Shao, Wang and Chen (2003) tried both the ASM and the nonlinear k-ε model to obtain boundary shear stress distribution in curved open channels with a simple rectangular open channel cross section.

2.4.1.3 Reynolds Stress Models

Alternatively, one can use Reynolds Stress Models (RSM), also called stress-transport model, to resolve the unknown turbulent stress directly from the solution of their differential transport equations. These are often referred to as second-order closure or second-moment closure models. They include the effects of streamline curvature, secondary motions, and sudden changes in strain rate and so on. Researchers used an exact differential transport equation to describe the behavior of specific Reynolds stress tensor and to correct some of the Boussinesq approximation's shortcomings (Wilcox, 2006, p. 322).

The closure approximations mentioned above are more elaborate than two-equation models since the terms modeled are tensors instead of simpler scalar and vector terms in the k-ε model. Reynolds equations are solved directly using RSM instead of simply including a nonlinear effect of generalizing the linear strain rate or using algebraic relationships derived, or simplified, from Reynolds stress transport equations to optimize the model. This is different from the non-linear k-ε model and the ASM, discussed in Section 2.4.1.2. As a result, RSM incurs higher computing costs than the non-linear k-ε model and the ASM. However, RSM provides better results when used in situations of turbulence-driven motions (Cokljat & Younis, 1995).

Cokljat and Younis (1995) used an RSM to predict the boundary shear stress distribution in open channels of both simple and compound cross sections. Their model is found to accurately reproduce the details of the turbulence-driven secondary motions that occur in the cross-stream

planes. There is a localized region of wall stress deficit that is perceived to move towards the sidewalls with increasing aspect ratio in rectangular channel simulations.

Kang and Choi (2006) studied a rectangular open channel of 0.2 mm wide and 0.1 m deep. The sidewall shear stress distribution showed almost uniform shear stress between the 10% depth and 90% depth. In the upper water column within 10% depth, the shear stress appeared to be about 60% higher than the mean uniform shear stress value. This is attributed to inner secondary currents occurring at the juncture of the free surface and sidewall (Kang & Choi, 2006; Broglia, Pascarelli & Piomelli, 2003). The inner secondary currents transfer high momentum from the center to the sidewalls near the free surface. RSM was also applied to other smooth rectangular open channels and compound meander channels (Jing, Guo & Zhang, 2009; De Cacqueray et al., 2009).

2.4.2 Direct Numerical Simulation

Direct Numerical Simulation (DNS) means a complete direct 3D and time-dependent solution of the Navier-Stokes and continuity equations without turbulence closure. Since DNS resolves flow motions of all scales, it is recognized to be the most precise simulation tool for the analysis of turbulence structures and wall effects (Launder, 1990).

Statistics computed from DNS results can be used to test proposed closure approximations in engineering models. It can also be used to obtain an understanding of turbulent structure and processes that can be of importance in developing turbulence-control methods or prediction methods. Furthermore, DNS can be viewed as an additional source of experimental data, taken with unobtrusive measurements. All comments assume the DNS is free of significant numerical error.

Mean flow properties and turbulent statistics for square duct flow have been studied using DNS in the recent decades. The main difference between a full duct flow and an open channel flow is that the flow in the duct is driven by pressure. The shear Reynolds number was 300 based on mean friction velocity and the duct width (Gavrilakis, 1992). The dimensionless wall distance was larger than one along the cross-sectional direction, so the no-slip wall condition used on the sidewalls should be reconsidered. Huser and Biringen (1993) continued the work to use slightly coarser

uniform mesh, and the shear Reynolds number was low at 600. They suggested the difference from the work of Gavrilakis (1992) was because of the Reynolds number difference. The higher the Reynolds number, the steeper the dimensionless wall shear stress drops near the corners. The maximum local shear stress values were both found on the bisector of the duct walls. For both cases, the no-slip condition applied on the sidewall is questionable.

Joung and Choi (2007) demonstrated the mechanism responsible for generating secondary flows in a square duct. The shear Reynolds number was equal to 300. Dimensionless wall distance was smaller than one. The results of the local shear stress distribution have some deviations in the middle and the corner regions of 10% and 20%, respectively, compared with the experimental data. However, it agreed pretty well with Gavrilakis's (1992) work using the same geometry. Therefore, the dimension of the geometry is of importance, because of the pattern of secondary flow changes in different geometries.

Since DNS incurs enormous computing cost, it has only been applied to simple flows at low Reynolds numbers. LES is a compromise between RANS models and DNS, which can be used to solve large-scale motions of flow. Only small-scale motions are modeled. As a result, the number of grids can be significantly reduced in LES, and the accuracy of the model can be kept to a satisfactory extent (Joung & Choi, 2007).

2.4.3 Large Eddy Simulation

The methodology of LES will be discussed in detail in Chapter 3. Its applications to open channels regarding boundary shear stress distributions will be discussed in this section. Table 2.1 summarizes basic information about these studies.

Table 2.1 Studies of distributions of boundary shear stress using LES

Research work	Geometry	Deficiencies	Boundary conditions
Thomas and Williams (1995)	Trapezoidal compound channel	Large y^+; Uniform mesh	Stress-free water surface; periodic boundary condition; stress boundary condition (wall)
Broglia et al. (2003)	Rectangular duct	Short of effective comparison data	Stress-free water surface; periodic boundary condition; no-slip wall condition
Shi et al. (1999)	Rectangular open channel	Large y^+; Uniform mesh	Stress-free water surface; periodic boundary condition; modified power law (wall)
Sterling et al. (2008)	Rectangular open channel	Large y^+	Stress-free water surface; periodic boundary condition; no-slip wall condition
Kara et al. (2012)	Compound open channel	Large y^+; Uniform mesh	Symmetry water surface; periodic boundary condition; no-slip wall condition
Xie et al. (2014)	Compound open channel	Large y^+; Uniform mesh	Stress-free water surface; periodic boundary condition; Modified power law (wall)

Broglia et al. (2003) studied fully developed turbulent open-duct flows at three shear Reynolds numbers using LES. They aimed to determine the influence of a free surface on the turbulence characteristics in a duct flow. The discretization with 10^5 or 10^6 grid points was uniform in the streamwise direction, whereas points were clustered towards the walls in the spanwise and normal directions. In particular, the first point close to the wall was placed at dimensionless wall distance equal to 0.5 and at least 13 points were in the near-wall region (dimensionless wall distance smaller than 10). Periodic boundary condition was used in the streamwise direction, and no-slip boundary condition was imposed on the walls. The boundary conditions enforced on the top surface of the computational domain were either the no-slip conditions or zero-stress boundary conditions to test

the influence of free surface. However, there were only comparisons with the DNS models involving some imperfect settings in the mesh.

Thomas and Williams (1995) utilized the LES technique with the standard Smagorinsky method to simulate a trapezoidal compound channel with extensive floodplains at a bulk Reynolds number of 430000, estimated from the hydraulic radius and the bulk velocity. The geometry of the simulation was similar to an experimental work and was discretized uniformly resulting in the dimensionless distance of $x^+ = 658$, $y^+ = 98$, and $z^+ = 240$. The flow field was periodic in the streamwise direction with a repeat length of 1.2 m. At the free surface, a stress-free rigid lid was added. Around the wetted perimeters, the stress boundary condition was applied meaning that the instantaneous stress was assumed to change with the instantaneous velocity linearly $\tau/\tau_a = U/U_a$. The subscript represented averages taken over a streamwise strip at a point on the channel perimeter. The main deficiency in the simulation was the coarse streamwise resolution. A double of the resolution in any one direction would have doubled the memory required. Cater and Williams (2008) studied the same case with a higher resolution. However, the mesh was still not fine enough to achieve the no-slip wall condition. The same boundary conditions were applied to this case. The insufficient development length in the experiments was considered the cause of differences in the comparison according to these authors.

Shi, Thomas and Williams (1999) investigated a turbulent flow in a rectangular open channel. The bulk Reynolds number was 90400. The aspect ratio was two and the length was six depths. The geometry was discretized using uniform mesh giving the dimensionless wall distance of $x^+ = 250$, $y^+ = 75$, and $z^+ = 75$. However, this resolution was insufficient to resolve the viscous sublayer and buffer region; a length damping function was used to reduce the dissipative effect of the mean shear. A periodic boundary condition was applied to the flow. External pressure and tangential stress were set to zero at the free surface. At the solid walls, a modified form of power-law boundary condition $U^+ = A(y^+)^{1/7}$ was utilized, and the first grid point fell on the wide-open channel log-law profiles. A greater degree of resolution was suggested to be used in future studies.

Sterling, Beaman, Morvan and Wright (2008) examined the possibility of using LES to obtain a database of instantaneous bed shear stress data, from which the behavior of extreme events could

be acquired. A significant variation of a fluctuating component of bed shear stress, around the time-averaged value of bed shear stress, was found by analyzing the standard variation. Large values of skewness suggested that the extreme or peak values of boundary shear stress would occur frequently. The behavior of instantaneous shear stress is complex and cannot necessarily be attributed to a single flow mechanism. In the simulation, the same geometry as one of the rectangular flumes that Knight, Demetriou and Hamed (1984) used was investigated. Periodic boundary condition was applied. Stress-free, no-slip boundary conditions were applied to the free surface and channel perimeters, respectively. The total number of mesh elements utilized was 572,000, with 160, 65, and 55 elements in the streamwise, lateral, and vertical directions, respectively. The mesh was created by specifying a first cell height to all walls ensuring $y^+ = 5$ with a growth factor of 1.3 for ten layers. The setting dissatisfied the requirement for a no-slip wall condition. The predicted boundary shear stress distributions generally agreed well with the experimental data. However, the values at the center regions on the channel-bed were over predicted by the LES, which was seen elsewhere in RANS simulations.

Kara, Stoesser and Sturm (2012) studied turbulent flow in a compound open channel with deep and shallow floodplain depths. The geometries were taken from the study of Tominaga and Nezu (1991). The mesh was discretized uniformly, which was not suitable for no-slip wall condition because of the large dimensionless wall distance of 6. Cyclic boundary condition was employed in the streamwise direction. The no-slip wall boundary condition was used for smooth walls. The free surface was treated as a plane of symmetry. Kara et al. (2012) reported that the inaccurate estimation of streamwise velocity profile was due to the insufficient flow development in the experiment. Furthermore, the erroneous predictions of bed shear stress on the floodplain were considered as the result of using the log-law to obtain the local shear stress in the experimental work of Tominaga and Nezu (1991).

Xie, Lin and Falconer (2014) studied the turbulent flow in an asymmetric compound open channel. The model was set up based on the previous laboratory model study. The bulk Reynolds and Froude numbers were 67000 and 0.39, respectively, based on the mean bulk flow velocity 0.349 m/s. The computational domain was discretized using a grid of 192×96×384 cells in the streamwise, vertical and spanwise directions, respectively. At the bed and on the sidewalls, a near

wall modeling approach was employed, as opposed to relating the shear stress to the velocity adjacent to the solid boundaries based on a time-averaged wall power law (A modified one over seventh law). The free surface was modeled as a free-slip rigid lid. The results of channel-bed shear stress have some deviations in comparison to the experimental data. They found that time-averaged results were similar at different cross sections, although there were significant temporal and spatial variations in the 3D turbulent flow fields.

Sinha, Das, Patel and Samtani (2014) applied a 2D two-layered model to a straight compound open channel using the LES approach. The non-uniform rectangular grid was generated. The wall function was specified on the boundaries, and zero shear stress was specified on the free surface. Water depth was equal to the depth of the lower layer and a small water depth was applied to the upper layer at the initial condition. Two cases, including symmetry and asymmetry compound channels, were simulated based on the experimental work of Fraselle, Bousmar and Zech (2010), and Tominaga and Nezu (1991). No local shear stress data are available from the experimental work of Fraselle et al. (2010). In Tominaga and Nezu (1991), the minor difference between experimental and numerical simulation was due to the depth-averaged assumption.

Constantinescu, Koken and Mccoy (2008) applied the LES technique to the study of a horseshoe vortex system at the base of groynes (also known as spur dikes, which are popular river-training structures) and the associated distributions of bed shear stress around isolated and multiple groynes placed in straight channels. The authors were interested in understanding how the structure and intensity of the horseshoe vortex system were affected by an evolving scour hole due to the presence of a second groin or due to submergence. Other LES applications reported in the literature include studies like turbulence characteristics in flow over dunes (Xie et al., 2014), sediment transport in open channel flows (Widera, Toorman & Lacor, 2009; Zedler & Street, 2006), and bedform evolution in turbulent flows (Chou & Fringer, 2010; Kraft, Wang & Oberlack, 2011).

The LES technique is a powerful tool to simulate turbulent open channel flows. In previous studies, the applications all have some deficiencies, such as coarse mesh close to the boundaries, the use of inaccurate wall boundary conditions, and the shortage of actual comparison data. In this research

thesis, these difficulties will be overcome using advanced meshing strategies and the no-slip wall condition. Moreover, the results will compare with well-cited effective experimental data.

2.5 Experimental Work

Section 2.2 shows basic methods to obtain wall shear stress using theoretical knowledge. In this section, attention is given to the feasible methods to obtain the local shear stress in realistic experimental studies.

As flow in the open channel is invariably turbulent, no analytical technique can be expected to yield more than an approximate solution. All analytical models and numerical methods are subject to experimental verification. Since it is difficult to analyze from a purely theoretical point of view, semi-empirical models have been proposed based on measurements.

In this section, different ways to measure local shear stress in laboratory flumes, including direct and indirect measurements, are summarized and discussed in the next few sections.

2.5.1 Indirect Measurements

A standard indirect technique involves measuring velocity and pressure profiles normal to the boundary, and then solving for the boundary shear stress. We begin with reviewing the two indirect measurement methods.

2.5.1.1 Velocity Profile Method

The Velocity Profile Method, elucidated in detail in Section 2.2.2, is developed based on logarithmic velocity distribution after Prandtl–Karman. It involves measurements of Reynolds-averaged velocity profiles along lines normal to the boundary.

The theoretical investigations by Prandtl–Karman result in rational formulas for velocity distribution and hydraulic resistance over flat plates, in circular pipes and even in open channel flows. Since the constants in the formulas change with roughness, aspect ratio, and unusual shape of channel sections, the values of these constants have been studied for a long time in rectangular and trapezoidal flumes (Ghosh & Roy, 1970) and rectangular open channels (Çiray, 1970).

Instead of directly fitting the measured velocity profile into the log-law (summarized in Section 2.2.2), another applied form of this method is called the Clauser Plot Method. They both are indirect tools that measure the wall shear stress in turbulent boundary layers with reasonable accuracy. The difference is that the Clauser Plot Method (Clauser, 1954) is a graphical method using the properties of the time-averaged velocity profile in the logarithmic portion of the boundary layer.

The attractive feature of the Velocity Profile Method is that velocity measurements in the viscous sublayer portion of the profile, which are often difficult to obtain, are not required. However, this method is inappropriate for flow conditions such as those with strong pressure gradients, low Reynolds numbers, and separation. Moreover, it is not suitable to obtain the wall shear stress near the sidewalls since the velocity profile near the sidewall deviates significantly from the logarithmic law (Broglia et al., 2003).

The accuracy of the Velocity Profile Method, including the Clauser Plot Method, and fitting Reynolds-averaged velocity profile into the log-law, is not only dependent on the selection of Karman constant κ and integration constant C (Equation [2.4]), but also the method of measuring the velocity profile itself. For example, significant errors can arise in Pitot tube measurements due to their sensitivity to large-amplitude velocity fluctuations, misalignment and Low-Reynolds-number effects at the tube opening (Tropea, Yarin & Foss, 2007, p. 881). The key point of this method is to obtain accurate time-averaged velocity profiles, so the choice of apparatus is critical. From now on, the remaining literature review in this section is divided according to the apparatus used.

2.5.1.1.1 Laser Doppler Anemometer (LDA)

LDA is a powerful measurement technique, which is especially suited for velocity measurements in water. This technique does not require any calibration and is capable of non-intrusive measurements of complex flows.

A two-color LDA can measure the longitudinal and vertical velocity component separately with high accuracy. A three-component system with a frequency-shifting device can measure all three

orthogonal components of velocity in complex flows with reasonable accuracy, including regions of separated reversed flow. However, very-near-wall measurements are especially challenging because of reflections and the refraction of the laser beams due to the proximity of the wall (Tropea et al., 2007, p. 898). This is especially the case if the sidewall is not perfectly transparent due to the sidewall roughness or if the sidewall is inclined.

A powerful two-color LDA was applied to obtain boundary shear stress by Nezu and Rodi (1985). The secondary patterns in open channels were quite different from those of closed channel flows because of the absence of free surface. Nezu and Rodi (1985) reported that the strong free-surface vortex produced due to the high anisotropy of turbulence was the cause of the velocity dip on the free surface and another vortex generated near the channel-bed.

Differences between the local shear stress distribution in a rectangular channel and a trapezoidal channel were studied by Imamoto and Ishigaki (1985). The sidewall shear stress was zero at the foot of the sidewall in a rectangular channel, but it showed a non-zero or maximum in a trapezoidal channel. A zero value appeared at the free surface in a trapezoidal channel, but a non-zero value appeared at the same position in a rectangular channel. Moreover, the distribution along the sidewall was wavy with two peaks in a trapezoidal channel with a gentle slope, confirming its relationship with the 3D structure of flow (Ghosh & Roy, 1970).

The complex nature of the hydraulic problem of flow in an open channel with varying boundary roughness was studied using the LDA and the Velocity Profile Method (Knight & Macdonald, 1979). The same apparatus was applied to a curved open channel (Jin, Steffler & Hicks, 1990) and a compound open channel (Tominaga & Nezu, 1991).

2.5.1.1.2 Hot-film technique

Researchers have widely used the Hot-wire or the Hot-film for measurements in the air. One of the major difficulties encountered when using this apparatus in water is the contamination of the wire because the impurities in water prevent stable operation of the hot-wire. Intrusiveness, calibration and optimum length of the active hot-element can bring imprecision to the

measurement. Also, bubble formation on the surface of heated sensitive element seriously affects the measurements.

The Hot-film technique is valuable for measuring wall shear stress fluctuations, although it is not very popular today. The measurement of wall shear stress using an electrically heated element set into the surface is a well established technique that relies upon the similarity between the velocity profile adjacent to the wall and the temperature profile of the thermal boundary layer generated by the element. Accurate calibration of this Hot-film probe is conducted depending on the water temperature and calibration coefficients of each measuring point.

Tominaga, Nezu, Ezaki and Nakagawa (1989) used the Hot-film to measure secondary currents in rectangular and trapezoidal open channel flows, and to study the effects of the aspect ratio, the side slope of a trapezoidal channel, and the boundary roughness on the secondary flow structures. They confirmed the foundings of Nezu and Nakagawa (1984), and Nezu, Nakagawa and Tominaga (1985). The local shear stress is closely associated with secondary flows, which increases in regions where the secondary current flows towards the wall, and decreases in regions where the secondary current flows away from the wall. In the smooth rectangular channel, an inflection point can be found at a distance of 0.8 H away from the sidewall because of the bottom vortices. The position of this inflection point corresponds to the spanwise scale of the bottom vortex rather than the roughness parameter (Figure 2.7).

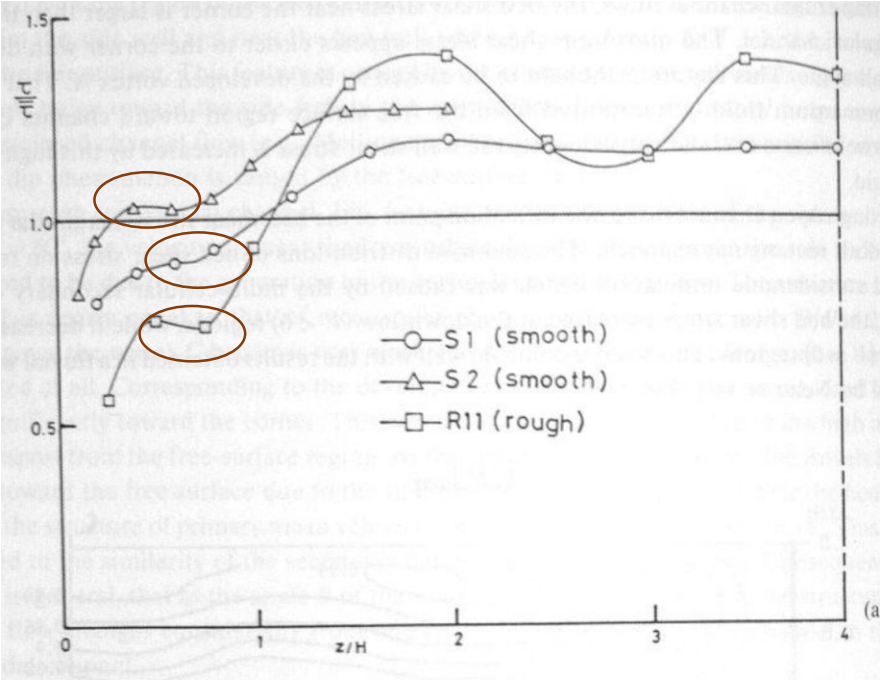

Figure 2.7 Inflection points on the distribution of bed shear stress (Tominaga et al. 1989)

The trapezoidal channel has a different secondary flow structure from the rectangular open channel, where the free surface includes a reverse rotation in the region between the sidewall and the free surface, causing no velocity dip phenomenon (Nezu & Rodi, 1985). The sidewall maximum shear stress position moves to the corner as the angle of the sidewall decreases, whereas it was at 0.6-0.7 *H* in the rectangular channel. Nezu and Rodi (1985) found that the normalized bed shear stress in the trapezoidal channel was larger than that of the rectangular channel in the corner regions.

In rough open channels, the distribution of bed shear stress showed considerable undulation because of the multi-cellular secondary currents, indicating that the bed shear stress increased at the downflow regions and decreased at the upflow regions (Nezu & Rodi, 1985). They found that roughness is an independent factor of boundary shear stress distribution.

2.5.1.1.3 Acoustic Doppler techniques

Profile measurements in the open channel flow are tedious and arduous. Most instruments fail when sediment transport occurs. The Acoustic Doppler Velocity Profiler (ADVP) is capable of

taking instantaneous, complete velocity profiles with a good resolution instead of point measurements.

Blanckaert (2010) investigated boundary shear stress and its interaction with main flow and secondary currents using the ADVP. The sidewall shear stress is obtained using the Velocity Profile Method, whereas the bed shear stress was obtained from the depth averaged velocity *Us* as:

[2.16] $$\tau_0 = \rho C_{f,bed} U_S^2$$

Chézy friction coefficient $C_{f,\text{bed}} = 0.53$ is approximately constant because the roughness of the bed is constant in the experiment. This technique is also called the Quadratic Stress Model (QSM) (Kostaschuk, Villard & Best, 2004), which offers a lower uncertainty of about 10% compared to 20% of the Preston Tube Method.

Rodríguez and García (2008) studied the local shear stress distribution in a rectangular channel over a rough, flat bed with smooth lateral walls using ADV. The patterns of streamwise velocity and secondary circulation presented a cellular structure that scales with flow depth. The shear stress value matched the downflow and upflow theory (Tominaga et al., 1989). The existence of differing roughness in bed and walls made the distribution of bed shear stress exhibiting a very marked oscillation, which is strong even away from the lateral walls. These results apply to urban streams, in which the bed is considerably rougher than the lateral walls.

2.5.1.1.4 Particle Image Velocimetry (PIV)

PIV is one of the well-established non-intrusive techniques for fluid velocity measurement. The PIV can provide the flow field, simultaneously at many points, whereas the LDV and the hot-film measure the velocity at a single point and do not supply the spatial structure of flow directly. The quality of data obtained from PIV technique is subject to the size of seed particles, image quality and size, camera frame rate, and processing software. PIV systems often use class IV lasers and high-resolution, high-speed cameras, which bring cost and safety constraints. Nguyen, Wells and Nguyen (2010) used this technique to obtain wall shear stress over inclined and curved boundaries.

As can be seen above, many instruments, working on a variety of principles, have been developed to measure velocity and turbulence in water flows. They all have special features. The Hot-film and the LDA can only provide single point measurements. The Hot-film is intrusive while the PIV can produce profile measurements but is inconvenient to deploy. Details of a comparison of the velocity measuring instruments based on different measurement techniques are given in Table 2.2.

Table 2.2 Comparison of standard velocity measuring instruments based on different principles [Modified from Lemmin and Rolland (1997), and Blanckaert and McLelland (2009)]

Purpose/factor	Instrument type			
	Hot-film	LDA	ADVP	PIV
Velocity calibration	Always needed	None needed	None needed	Always needed
Very low or inverse velocity	Impossible	Possible	Possible	Possible
Signal processing	Easy	Difficult	Easy	Easy
Seeding	No	Yes	Yes	Yes
Profile determination	Point by point	Point by point	In one acquisition	In one acquisition
Point measurement	1 mm	0.15 mm	5 mm	0.1 mm
Flow perturbation	Yes	No	No	No
Effect on measured Environment	Large effects	No effect	No effect	No effect
Mobility of instrument	Easily moved	Difficult to move	Easily moved	Safety constraints
Cost	Low	High	Low	High

2.5.1.2 Sublayer Profile Method

The Sublayer Profile Method involves accurately measuring the linear portion of the Reynolds-averaged velocity profile near the surface. The basic idea of this method is discussed in Section 2.2.4. Based on Equation [2.11], one can obtain the boundary shear stress.

Major challenges associated with determining τ_0 using Equation [2.11] are to find the region where the mean profile is linear, accurately and appropriately position the sensor in this region, and accurately calibrate the sensor for the measurements. This technique can only apply to flows over smooth walls.

Under the vast majority of flow conditions, the dimensions of the viscous sublayer region are small, typically a fraction of a millimeter. Therefore, the sensing dimension of the measurement probe must be small as well. Optical sensors such as the Laser Doppler Velocimetry (LDV) and the Molecular Tagging Velocimetry (MTV) can be used to measure the sublayer profile.

Steffler, Rajaratnam and Peterson (1985) used LDA to measure velocity profiles close to the boundary. They not only obtained boundary shear stress by fitting the velocity profile into the log-law but also used the distribution of Reynolds stress ($\tau_t = -\rho\overline{u'v'}$) directly. The latter is to use the theory mentioned in Section 2.2.3. The disadvantages of this theory are that errors of the Reynolds stress measurements become significant and that there is a need for extrapolation problems.

In Steffler et al. (1985), an initial estimate of shear velocity was obtained by first taking the maximum value from the Reynolds shear profile, and then using more data points within the viscous sublayer. The bed stress was determined directly by a linear curve fitting of these points. The shear velocity estimated from longitudinal velocity measurements in the viscous sublayer agreed well with that of the law of the wall.

Other researchers have obtained the shear velocity from the viscous sublayer. For example, Kirkgöz and Ardiçlioglu developed empirical equations for the boundary shear stress distribution as a function of the aspect ratio (Kirkgöz, 1990; Kirkgöz & Ardiçlioglu, 1997).

Table 2.3 presents a summary of studies reviewed in the Section 2.5.1 that used the Velocity Profile Method and the Sublayer Profile Method. In the table, the data in the brackets of the Depth and Width mean the values are flume sidewall heights (not the depth of flow) and bed widths. Null means the data is not available from the cited studies.

Table 2.3 A summary of studies that use the Velocity Profile Method and the Sublayer Profile Method to obtain the distribution of boundary shear stress

Research	Material	Length	Width	Depth	Discharge	Velocity	Channel shape		Location of measurement	Slope	Influencing factors				Velocity measurement
							Rectangular	Trapezoidal			Aspect ratio	Secondary flow	Roughness		
		(m)	(m)	(m)	(m^3/s)	(m/s)	Aspect ratio	Side slope	(m)				Smooth	Rough	
Steffler (1985)	Glass and steel	35.0	1.1	0.093-0.225 (0.5)	0.032-0.126	Null	5.08-12.3	×	21	1.2*10E-03, 2.3*10E-04	√	×	√	×	LDA
Nezu and Rodi (1985)	Null	20.0	0.6	0.04-0.195 (0.65)	Null	0.145-0.122	1-10	×	Null	Tiltable	√	√	√	×	LDA
Tominaga et al. (1989)	Iron and glass	12.0	0.4	0.03-0.19 (0.4)	0.002-0.051	0.186-0.397	2-8	32˚, 44˚, 60˚	6	Tiltable	√	√	√	√	Hot-film anemometer
Imamoto and Ishigaki (1989)	Null	5.9	0.2	0.0392-0.0405	0.0016-0.0085	0.014-0.028	5	0˚-4˚	3.9	Tiltable	√	√	√	×	LDA and micro-propeller currentmeter
Kirkgöz (1990)	Glass	12.0	0.3	(0.4)	0.0004-0.02	0.049-0.903	2.4-11.1	×	6	Tiltable	√	×	√	√	LDA
Kirkgöz and Ardıçlıoğlu (1997)	Glass	9.5	0.3	0.025-0.2 (0.4)	0.003-0.019	Null	1.5-12	×	6.5	Tiltable	√	×	√	×	LDA
Ardıçlıoğlu et al. (2006)	Glass	9.5	0.6	0.0353-0.1414 (0.6)	0.008-0.042	Null	4.42-21.6	×	6	0.0006-0.0050	√	×	√	√	Propeller-type velocity meter
Rodríguez and García (2008)	Null	12.2	0.9	0.0353-0.1414 (0.6)	0.05-0.11	0.48-0.72	6.3, 8.5	×	6	Tiltable	√	√	×	√	ADV
Blanckaert et al. (2009)	Null	9.0	1.3	0.11-0.21	Null	0.38-0.43	3.2-11.9	30˚-90˚	6.5	Tiltable	√	√	√	√	ADVP
Ardıçlıoğlu and Kırkgöz (2011)	Glass	10.0	0.3	0.025-0.2 (0.4)	0.0032-0.0195	Null	1.5-12	×	6.5	0.0005-0.002	√	×	√	×	LDA

2.5.2 Direct Measurements

Direct measurement methods have many advantages since they do not require pre-assumption. For example, they can supply time-resolved measurements of the instantaneous wall shear stress. Invaluable data from direct measurement can be used to check the efficacy of other indirect methods as well as other analytical theories. However, these methods require sensing systems that have a high-frequency response and are sufficiently small. Therefore, it is challenging to apply these methods for all kinds of flow configurations.

2.5.2.1 Preston Tube Method

Although the Preston tube technique is developed based on the log-law, it is considered a direct measurement technique because of its flexibility and efficiency (Ackerman & Hoover, 2001).

The technique has been frequently used to obtain the time-averaged wall shear in uniform flows. The wall function is suitable for describing flow characteristics near the wall. The function involves the wall shear stress, and the kinematic viscosity of water or the wall surface roughness. However, for non-uniform type flows, the log-law of the wall is not adequate. Also, the sizes of Preston tubes can be too large. They disturb the flow and therefore affect the results. Smaller sizes are more satisfactory than larges ones, in order to minimize the disturbances (Myers & Elsawy, 1975).

Ippen (1960) were the first to demonstrate the applicability of Preston tubes to open channels. The author investigated boundary shear stress distributions in curved trapezoidal channels under rough wall conditions. Davidian and Cahal (1963) studied the relationship between local boundary shear stress and Froude number. The distributions of boundary shear stress in a rectangular duct (Leutheusser, 1963) and a pipe (Replogle & Chow, 1966) have been measured using Preston tubes.

The aspect ratio was reportedly the only factor affecting the boundary shear stress on smooth boundaries (Cruff, 1965). The dimensionless wall shear stress decreases as the aspect ratio decreases at the same dimensionless location. For smooth rectangular channels, the region where the local shear stress is affected by the wall extends a distance about six flow depths laterally from the sidewalls. The shear stress is equal to γRS in the middle part as long as the aspect ratio is larger

than 12.5, compared to a threshold of 15 as reported in Rajaratnam and Muralidhar (1969). This is considered the threshold that the velocity distribution as well as other characteristics will not be affected by the sidewall in the middle region. The average shear stress at the channel-bed was much larger than that on the channel walls at large aspect ratios and the bed shear stress become increasingly uniform as the aspect ratio increases. Ghosh and Roy (1970) compared results from the Preston tube with the Float Element Technique and Prandtl-Karman's Velocity Profile Method in the rectangular flume and trapezoidal flume. The dispersion of the measured shear stress distribution on the mean value of various estimates was lowest for the Preston tube measurement. Therefore, due to its inherent simplicity and reliability, it was considered the ideal choice to explore the boundary shear stress distribution in open channels.

Wall roughness was shown to be another influence factor of the boundary shear stress distribution. The percentage shear force carried by the wall and the channel-bed was related to the roughness (Knight & Macdonald, 1979).

The secondary flow has huge influences on the flow characteristics (Knight et al., 1984). The distributions of wall and bed shear stress exhibit certain perturbations, which are called inflection points by subsequent researchers. This phenomenon depends on the number and distribution of the secondary flow cells within the cross section in a smooth channel of rectangular section. Moreover, the secondary flow influences the location of maximum sidewall shear stress, which occurs at a certain intermediate position between the water surface and the bed, as opposed to at the water surface. The secondary flow effect also displaces the maximum bed shear stress from the centerline position towards the corner at low aspect ratios.

The maximum sidewall shear stress and bed shear stress in a compound channel were studied by Ghosh and Jena (1971). The boundary shear stress distribution was affected by the secondary flow in a rectangular channel as discussed above. Also, the maximum shear stress locations are not at the free surface or the centerline of the channel-bed. For the floodplain, the maximum occurs at the junction with the internal wall. For rough boundaries, the maximum shear stress location changes with the depth of flow on the sidewalls and is at the centerline on the channel-bed (Ghosh & Jena, 1971).

The interaction mechanism between the main channel and the floodplain was studied thoroughly. The shear stress in the floodplain is much larger than its undisturbed value with no interaction with the main channel flow (Myers & Elsawy, 1975). Researchers have used the Preston-tube to study the transfer of longitudinal momentum from the main channel to the floodplain (Rajaratnam & Ahmadi, 1979), lateral momentum transfer (Knight & Demetriou, 1983), and the non-linear nature of Reynolds shear stress in the shear layer and local friction (Knight & Shiono, 1990).

The Preston tube has also been used to study the resistance effects of floodplain vegetation (Pasche & Rouvé, 1985), to test a numerical model (Rameshwaran & Naden, 2003), and to obtain velocity measurements in meandering or non-uniform compound channels (Rajaratnam & Ahmadi, 1983).

The Preston Tube Method is a single point variant of the Clauser Plot technique mentioned in Section 2.5.1. Section 2.2.5 gives theoretical information about the Preston tube.

Table 2.4 summarizes experimental studies about the distributions of boundary shear stress in various channels using the Preston tube. In the table, the data in the brackets of the Depth and Width mean the values are flume sidewall heights (not the depth of flow) and bed widths. Null means the data is not available from the cited studies.

Table 2.4 A summary of studies that used Preston tubes to obtain the distribution of boundary shear stress

Research	Material	Length	Width	Depth	Discharge	Velocity	Channel shape		Location of measurement	Slope	Influencing factors				Velocity measurement instrument	Prestontube size
							Rectangular	Trapezoidal			Aspect ratio	Secondary flow	Roughness			
		(m)	(m)	(m)	(m^3/s)	(m/s)	Aspect ratio	Side slope	(m)				Smooth	Rough		
Rajaratnam and Muralidhar (1969)	Glass	9.75	0.076-0.896	0.069-0.896	0.143-7.128	0.10-0.16	0.83-20	×	7.32	0.00636-0.0197	√	×	√	×	Pitot tube	3 mm
Ghosh and Roy (1970)	Glass	13.41	0.20	0.049-0.175	0.005-0.033	0.40-0.99	1.2-3.1	0.5-1.5	7.92	Adjustable	√	×	√	√	Pitot tube	0.125 in.
Cluff (1965)	Steel	24.38	1.06	（0.46）	0.011-0.207	0.84-8.44	4.76-33.3	×	21.34	Adjustable	√	×	√	×	Pitot tube	Null
Davidian and Cahal (1963)	Null	42.67	1.08	0.127-0.203	Null	Null	5.34-8.84	×	35.97	Adjustable	√	×	√	×	Null	Null
Knight and Macdonald (1979)	Perspex	15.00	0.46	（0.38）	0.003-0.114	Null	1.48-15	×	10.00	$9.58*10^{-4}$	√	×	√	√	Novar-stream flow miniature propeller meter	7 mm
Knight et al. (1984)	perspex	15.00	0.61	0.0319-0.223.7	0.00198-0.02866	0.0319-0.2237	0.3-20	×	11.97	$9.66*10^{-4}$	√	√	√	×	Novar-stream flow miniature propeller meter	7 mm

2.5.2.2 Membrane Analogy

Olsen and Florey (1952) used analytic, membrane analogy, and Finite Difference methods to obtain boundary shear stress and velocity distributions in different shapes of channels. These included three rectangular channels, five V-notch channels, and six trapezoidal channels that had side slopes of 2:1 (horizontal to vertical). The aspect ratio was up to eight. Eleven of these channels used the membrane analogy. Two used the Finite Difference Method. The last one used both approaches to compare with the analytical solution.

In their study, the velocity and shear distributions in a channel section were governed by partial differential equations, leading to the analytical solution discussed in Section 2.3.5. An equation for an elastic membrane was expressed mathematically in a similar way as the partial differential equations. This analogy adopted an opening in a flat plate with boundary geometry similar to the channel cross section with symmetry at the free surface. A thin rubber membrane was then stretched over the opening, and a uniform pressure was applied to deform the membrane. The solution involves measuring the elevation and slope of the membrane at selected grid points.

Independent solutions by the three methods applied to the simplest rectangular channel showed consistent results. In both rectangular and trapezoidal channels, the maximum dimensionless shear stress values began to level off at a distance of two flow depths to the sidewalls at the channel-bed.

2.5.2.3 Float Element Technique

Perhaps the simplest technique (in theory) for directly measuring wall shear stress is the floating element sensor. Unlike other sensors, which indirectly measure the shear stress, floating-element sensors are not dependent upon the veracity of correlating functions. Therefore, they are not affected by errors associated with the theoretical assumptions.

This Float Element Technique (also called shear plate sensor) has been used firstly by Kempf (1929). It involves measuring the force exerted by the bed shear stress on a small element of the wall that is separated from the rest of the boundaries with small gaps. Subsequently, the development of a floating element instrument was carried forward by Bagnold (1955). The author

used this technique because the depth of invisible channel-bed could not be determined. This technique was applied to obatin measurements of boundary shear stress in boundary layers (Pujara & Liu, 2014) and wave flows (Barnes, O'Donoghue, Alsina & Baldock, 2009).

Petryk and Shen (1971) used the Float Element Technique to measure the shear stress directly on the bottom of a laboratory flume floor. The values of shear stress are in good agreement with those obtained by the Preston tube technique. The surface area of the float plate exposed to the flow is 0.00205 m^2. Figure 2.8 shows a schematic diagram of the float element.

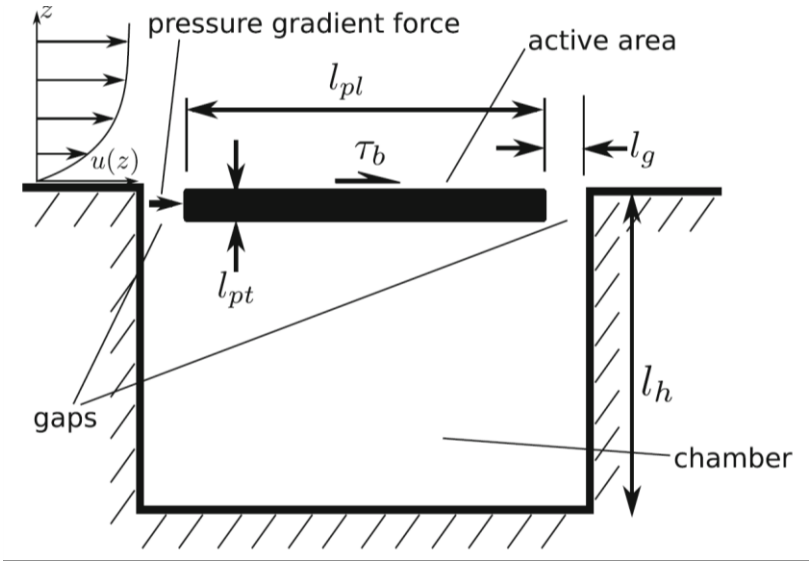

Figure 2.8 Schematic of the shear plate sensor used in the Float Element Technique (Pujara & Liu, 2014)

For measurement in open channels, Ghosh and Roy (1970) continued using the three-point suspension arrangement originally employed by Bagnold (1955). As shown in Figure 2.9, the stagnant pool of water outside the channel is connected with the steady flow inside the test section through gaps around the test section. The drag exerted by the flow tends to make the gap downstream of the trial section narrower and that of the upstream wider. The float element can be brought back to its initial position by the weight on the pan-pulley arrangement. The switching on of a glow lamp is the signal of the initial condition. Therefore, one can obtain the shear drag, as well as the boundary shear stress.

Their work presented the boundary shear distributions in both rough and smooth open channels, in which rectangular sections had aspect ratios ranging from 1.2 to 3.1 and trapezoidal sections had side slopes ranging from 0.5 to 1.5. The total inner channel length is 44 ft, and the width is 0.656 ft.

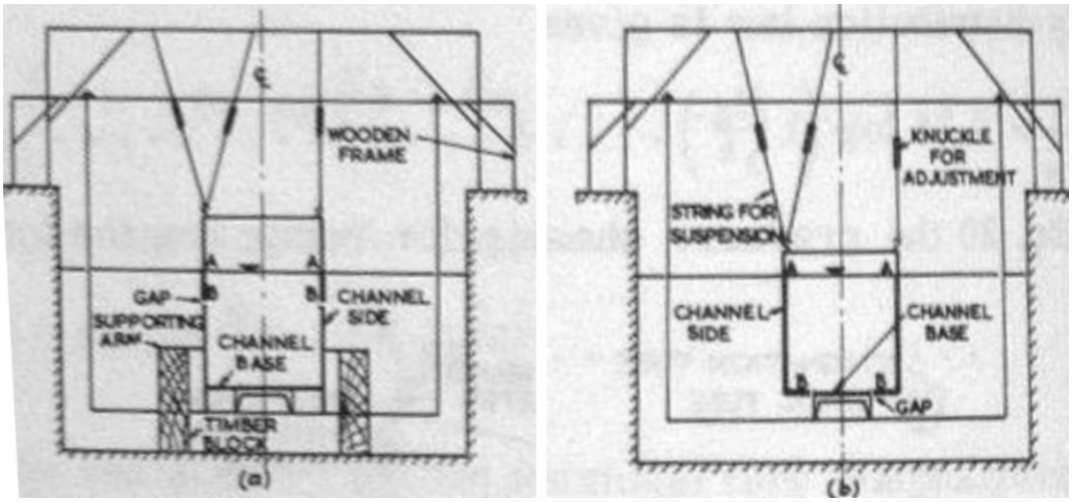

Figure 2.9 Scheme for measurements of boundary drag distribution in a rectangular channel using the Float Element Technique (Ghosh & Roy, 1970)

The maximum shear occurred at the top surface on the sidewalls and in the middle part of the channel-bed in a smooth rectangular channel, whereas on an artificially roughened surface, it neither occurs at the free surface nor the channel-bed centerline, but at some distance away from the top surface and the centerline towards the corners. In the case of a smooth channel, the degree of reliability of the three methods studied is in descending order starting with the Floating Element Method, the Velocity Profile Method, and the Preston Tube Method. In the rough channel case, it is in descending order starting with the Floating Element Method, the Preston Tube Method, and the Velocity Profile Method since the assumption of a constant Karman coefficient is no longer valid. The total drag per unit length of the channel is in close agreement among the three methods, but each of these methods gives varying results at different locations around the wetted perimeter. The influence of secondary flow on the boundary shear distribution was not completely clear in the absence of a dependable theory about secondary flow at that time.

2.5.3 Other techniques

2.5.3.1 Surface Coating Techniques

Tanner and Blows (1976) studied the motion of oil films on surfaces in airflow, with application to the measurement of skin friction. Measurement of the shear stress distribution over a surface by liquid-crystal coating was studied by Fujisawa, Aoyama and Kosaka (2003). Oil-film Interferometry and Liquid-crystal Method are both valuable techniques for direct measurements of shear stress, but so far, their applications have been limited to air flows.

2.5.3.2 Surface Fence Method

The surface fence or sublayer fence, used for measuring the magnitude and direction of the local shear stress, was first applied by Konstantinov and Dragnysh (1960). The fence height should ensure the dimensionless wall distance $y^+ \leq 5$ and thus remain within the viscous sublayer. Therefore, it is a device independent of the validity of the logarithmic law of the wall. This method applies to the turbulent boundary layer and has not been applied to open channels so far.

2.5.3.3 Mean-pressure Gradient Method

The Mean-pressure Gradient Method is a classic way for estimates of mean shear stress on the boundary of a pipe or a duct. Many textbooks discuss the Mean-pressure Gradient Method (Fox & McDonald, 1992, p. 340). It describes a relationship between the mean pressure drop ΔP over a length of a duct or a pipe and the average wall shear stress acting over the surface area in a control volume of a fully developed pipe or duct flow with a constant cross-sectional area:

[2.17] $$\bar{\tau}_0 = -\frac{R}{2}\frac{\partial P}{\partial x}$$

where R is the radius of pipe or duct half-height, $\bar{\tau}_0$ is the mean value of wall shear stress over a specific surface area, and x indicates the streamwise direction.

2.5.3.4 Momentum Integral Approach

The Momentum Integral Approach is useful for estimating boundary layer flows. If the fluctuating velocity variances in the streamwise direction are not significant, the local shear stress can be expressed using the momentum thickness θ and the displacement thickness δ^*, given by:

[2.18] $$\tau_0 = \rho U_e^2 \frac{d\theta}{dx} + (\frac{\delta^*}{\theta} + 2)\frac{\theta}{U_e}\frac{dU_e}{dx}$$

where U_e is the free stream velocity. This equation includes the effects of axial pressure gradient. The last term on the right hand side of this equation is zero for flat-plate boundary layer flow (Nagib, Chauhan & Monkewitz, 2005).

Unlike the Mean-pressure gradient method in ducts, the momentum integral approach does not require the flow to be fully developed. Considerable care must be given to ensure that the flow under investigation is adequately planar. Additional difficulties can arise from the need for accurate measurements of axial velocity (Tropea et al., 2007, p. 880).

Compared to indirect measurement techniques, methods for direct measurements are harder to implement in the laboratory environment and field conditions, although they are expected to produce more accurate results.

Advances in instrumentation for measurements of water velocity, including Preston tubes, Hot-film, LDV, ADV, and PIV, have increased the spatial and temporal resolutions, providing an opportunity to estimate the wall shear stress and to compute the Reynolds stress from velocity fluctuations. Some of these techniques have limitations such as intrusion when used in the field and near boundaries. Moreover, high costs of instrumentation, and the requirement of time and labor for CTA, LDV, and PIV have limited their application in field conditions (Ackerman & Hoover, 2001). Experimental as well as field studies are important, producing invaluable data for an improved understanding of turbulent flow characteristics.

2.6 Field Measurement

It takes significant efforts to measure the boundary shear stress in field directly. Therefore, researchers usually estimate boundary shear stress from the observation of velocity profiles in practice similar to the Velocity Profile Method described in Section 2.5.1.1.

2.6.1 Current meter

Conventional equipment (current meters mounted on hand-held rods) was used by Wilcock (1996) under typical field conditions in a large gravel-bed river (the Trinity River in U.S.). The discharge was constant and maintained a steady flow condition. Replicate observations were made to evaluate the precision of three methods for estimating local bed shear stress from velocity observations. The essential idea is to fit velocity values into the logarithmic vertical velocity profile. It is possible to use a single near-bed velocity (lower 20% depth of the flow), the depth-averaged velocity, and the gradient of near-bed velocity profile (the least squares fit to at least six observations). The first two choices need estimates of bed roughness. The most accurate estimation is to use the depth-averaged velocity.

Nezu, Tominaga and Nakagawa (1993) used an electromagnetic flow meter to study secondary currents in a wide river and a narrow river. They identified multicellular secondary currents in the wide river and a velocity dip phenomenon, caused by a free-surface vortex in the narrow river. The features of these secondary currents coincide well with those obtained in laboratory experiments (Nezu & Nakagawa, 1984) and numerical calculations. 3D turbulent structures associated with secondary currents are almost universally independent of the Reynolds number through a comparison of field data and laboratory data.

Afzalimehr and Rennie (2009), using a micro-current propeller meter, measured velocity profiles at 24 cross sections in the Ghamasiab River in Iran. They tested a new method for determining the shear velocity in non-uniform flows over gravel-bed channels based on the boundary layer displacement thickness and the momentum thickness.

2.6.2 Acoustic Doppler Profiler (ADP) or Acoustic Doppler Current Profiler (ADCP)

ADP has advantages over conventional current meters. First, the ADP relies on acoustic profiles and positioning from a Differential Global Positioning System (DGPS) instead of using an anchor, and therefore it can be used from a moving launch. Second, the ADP provides 3D velocity profiles to describe flow structures, whereas single-point current meters require continuous repositioning of the meter at different elevations above the bed and reanchoring the launch at various positions,

which may take several hours (Kostaschuk & Villard, 1996). Last, each profile contains many observations along a vertical line measured over a short time.

The most serious limitation of the ADP is the loss of data close to the boundary. The costs are also a concern but are usually dwarfed by the expense of the ship required to ensure a safe and professional deployment.

Kostaschuk et al. (2004) used a Sontek 1.5 ADP for measurements of velocity profiles over dunes in the Fraser River estuary in Canada. They recommended using the QSM (discussed in Section 2.5.1.1.3) for the calculation of boundary shear stress over the Velocity Profile Method.

Sime, Ferguson and Church (2007) tested the three ways suggested by Wilcock (1996) to obtain local shear stress using the Velocity Profile Method (discussed in Section 2.6.1). They used a moving boat ADCP and obtained velocity profiles in the lower Fraser River in Canada. The depth-averaged velocity was proved the most precise matching Wilcock's (1996) conclusion.

Pieterse, Puleo, McKenna and Aiken (2015) used ADP in narrow tidal channels in a salt marsh of the St. Jones River in U.S. The bed shear stress was estimated from the velocity profiles using three methods: the log-law, the Reynolds stress, and the TKE. The Reynolds stress and the TKE method gave similar results, while the log-law method led to smaller bed shear stress values during ebbing tide.

2.6.3 Acoustic Doppler Velocimeter (ADV)

The main difference between ADV and ADCP is that the former one uses focused beams to measure with high sampling rates in only one small point, whereas the latter produces a vertical profile using a diverging beam pattern.

Biron, Lane, Roy, Bradbrook and Richards (1998) studied the uncertainty of using the law of the wall in shallow streams since most measuring devices used in the field do not allow flow velocity to be measured very close to the bed. The selection of measurement heights for the estimation of bed shear stress using a fitted logarithmic profile was unknown. Therefore, they investigated this

problem using a Sontek field ADV that measures instantaneous flow velocity in three dimensions. The measuring volume was 0.125 cm^3, and it was situated 5 cm below the sensor head. The instrument could sense the distance between the bottom of the measuring volume and the bed surface to a high degree of 1 millimeter. Data were sampled at three field locations of different roughness in shallow clear water tributaries of a braided river. The results indicate that using the full flow depth instead of the bottom 20% of the profile generates an underestimation of the shear stress in uniform flow.

The effects of secondary currents on the erosion of cohesive riverbanks were studied by Papanicolaou, Elhakeem, and Hilldale (2007) using ADV measurements. They made the measurements from the Union Flat Creek with irregular cross sections. They reported that the presence of the secondary flow increased the depth-averaged sidewall shear stress. Hilldale and Baird (2002) also studied the secondary flow effects and collected 3D velocity data at three cross sections with plane beds or dunes in the Low Flow Conveyance Channel of the Middle Rio Grande using a SonTek ADV. They reported that the velocity dip phenomenon is pronounced, and the distribution of bed shear stress is sinusoidal under plane bed conditions, in comparison to dunes. The phenomenon of wavy distributions of bed shear stress also showed consistency in the study of rough boundary flumes (Nezu et al., 1993). However, the authors showed a contradiction with published data of Nezu and Rodi (1985) in that the velocity dip only occurs below a critical aspect ratio of between five and six.

Liu and Wu (2015) used both a PC-ADP and an ADV to estimate bed shear stress in the Pearl River estuary. The Velocity Profile Method was reportedly the most suitable way to estimate the bed shear stress in non-stratified homogeneous flows among all tested methods, including the Reynolds Stress Method (Section 2.2.3), the Turbulent Kinetic Energy Method (Section 2.3.5), and an Inertial Dissipation Method.

Ackerman and Hoover (2001) described the use of a Preston-static tube to measure the local shear stress in Torpy River watershed of the McGregor Mountains in Canada. It is possible to measure local shear stress quickly, consistently, and inexpensively in the field using this technique with high spatial resolution.

2.7 Ice-covered rivers

Most of the rivers in Canada are covered with ice during the winter season, and the ice covers have a thickness more than 0.6 m for at least four months of the year. Ice covers may persist much longer periods with a depth exceeding 0.9 m in northern regions (Robert & Tran, 2012). The presence of ice cover on a river results in considerable changes in the structure of the flow. The principles, which used to be suitable for open channel flows, are no longer effective in the prediction of streamwise velocity distribution, the calculation of discharge, the estimation of local boundary shear stress, and the transport of sediment. Investigations of these processes have practical and scientific interest.

2.7.1 Velocity Profiles in Ice-Covered Flows

It is difficult and expensive to obtain field measurements of water velocities from ice-covered rivers. It is desirable to obtain a proper expression for velocity profiles for applications in ice-covered hydraulics.

Ice-covered flow may be considered a two-layer flow, one of which forms near the channel-bed and the other under the ice cover. There is a maximum velocity layer with zero velocity gradient (also with zero shear stress) at the intersection of the two flow layers (Dolgopolova, 1998). The vertical location of the maximum velocity depends on the relative magnitudes of the channel-bed and ice cover underside roughness, and the location steers towards the rougher surface (Robert & Tran, 2012). However, the plane of zero shear stress is reportedly not coincident with the maximum velocity plane (Parthasarathy & Muste, 1994; Chen, Gu, Huai & Zhang, 2015). The plane of zero shear stress is slightly displaced towards the smoother surface compared to the maximum velocity plane.

Tsai and Ettema (1994) developed a simple two-power law expression for the velocity profile in ice-covered flows. The effectiveness of the two-power law was verified using measured velocity profiles obtained from rivers and a laboratory flume (Teal, Ettema & Walker, 1994). This two-power law function is simpler compared to the logarithmic law of the wall. It is continuous and differentiable between the ice cover and the riverbed. The logarithmic law has also been applied

to ice-covered flows, leading to overestimates of velocities over a large portion of the depth close to the location of maximum velocity plane (Lau, 1982).

Healy and Hicks (2004) used the two-power law to obtain curve fits to all observed data, which helped to minimize the distorting effects of some measurement errors. Suitable exponents and coefficient of a two-power law for ice-covered flows were determined using a multi-parameter regression analysis (Attar & Li, 2012).

The two-power law is the most widely used expression for the vertical distribution of streamwise velocity in ice-covered flows. However, more 3D flow measurements of improved spatial and temporal resolutions from ice-covered rivers are needed to compare with laboratory-based findings, and to verify numerical results. Therefore, measurements of streamwise velocity profiles under ice-covered conditions in the field and laboratory are reviewed below.

Commonly used instruments [Pulse Coherent Acoustic Doppler Profiler (PC-ADP) and Mini-ADPs] were used to measure velocity distributions through the ice at Fort Simpson in the North West Territories by Mudge and Sloat (2004). The functioning and features of the two apparatus were investigated. Unique velocity profiles, including the near-ice and the near-bottom boundary layers, were acquired with two different Mini-ADPs, which were considered as the right tool for measurements under ice. It has the advantages of small size, working under harsh environment, and high resolution. The PC-ADP was able to acquire 50 cm long, high-resolution (1.6 cm) profiles of the near-ice boundary layer. It gave the friction velocity within the boundary layer and the roughness scale of ice underside, which was highly dynamic and complex.

A series of experiments for the incipient motion of frazil particles were carried out in ice-covered flows in the laboratory (Jueyi, Jun, Yun & Faye, 2010). Small wood pieces were added to the floating foam to generate an ice cover with different roughness and frazil particles were made of wax. Under the same flow condition, the shape of the relative flow velocity profile appeared to be identical, independent of flow depth and bulk mean velocity.

Two series of experiments were performed using an Acoustic Doppler Velocimeter (ADV) under the open channel condition and the rough ice-covered condition (Robert & Tran, 2012). Ice-covered flows were studied in a flume of 8 m long, 50 cm deep, and 0.6 m wide. The cover was constructed using 12 mm thick plywood. It showed that the introduction of an ice cover increased the depth of average flow by 10%.

2.7.2 Discharge Estimation in Ice-Covered Flows

Flow discharge is a key hydrologic parameter that largely controls river regime, hydraulic extremes such as flooding or low flows, and many water-dependent ecological processes (Beltaos, 2011).

Ice-cover formation increases flow resistance and flow depth for a given discharge and a channel slope. The presence of an additional boundary almost doubles the wetted perimeter for wide channels. Consequently, a stage-discharge relationship developed for the open channel flow may not be accurate for ice-covered flows.

To minimize time, costs and discomfort of working under difficult weather conditions, the mean discharge is usually estimated by measuring only a few points using the velocity-area approach. Teal et al. (1994) evaluated point-measurement methods for estimating the vertical distributions of streamwise velocity in ice-covered rivers. The evaluation used profiles generated numerically based on the two-power law (Tsai & Ettema, 1994). The two-point method (20% and 80% depth) was the most preferred method with the bias of approximately 2%.

Healy and Hicks (2004) explored the viability of using an index velocity approach for winter discharge estimation based on limited actual point velocity measurements in the cross section. This index velocity could be the maximum point velocity for the entire cross section, the maximum vertically averaged panel velocity for the cross section, the maximum point velocity for the panel of maximum flow depth, and the vertically averaged velocity for the panel of maximum flow depth. Velocity profiles from the laboratory and field measurements were fitted into the two-power law to facilitate the determination of the index velocity. An examination of the data suggested the existence of a unique relation between the index velocity and the mean velocity.

Accurate determination of river discharge under an ice cover requires direct measurements. Beltaos (2011) investigated the feasibility of using slope-area hydraulics and the quasi-uniform flow concept to develop discharge-stage rating relationship at two stations in the Peace River and the Mackenzie River in Canada. The author reported that slope-area methods (Manning's equation) would be the most effective when combined to sporadic winter flow measurements during the ice season. The key premises are that the quasi-uniform flow concept applies and slush is not severe.

2.7.3 Boundary Shear Stress in Ice-Covered Flows

The boundary shear stress, especially the local boundary shear stress in ice-covered flows, is poorly understood since the presence of an ice cover makes the structure of the flow more complex, compared with that in an open channel of the same geometry.

The ice-covered flows are usually considered fully developed asymmetric turbulent channel flows. Such flows are characterized by different boundary shear stress on the two opposite surfaces, which are the ice cover and the channel-bed. A widely used two-layer theory divides the cross-sectional area of an ice-covered channel into an upper ice layer and a lower bed layer at a plane of zero shear stress. The plane of zero shear stress does not coincide with the plane of maximum velocity except for the symmetric channel flow and the open channel flow, which are respectively at the middle depth and the free surface (Tsai & Ettema, 1994). Numerous attempts have been made to obtain the mean bed shear stress and mean ice cover shear stress.

Lau and Krishnappan (1985) compared experimental data under open channel condition and ice-covered condition. They concluded that the lower layer in an ice-covered flow could be treated as a free-surface flow for calculating the bed load transport. Mean bed shear stress was obtained using the theory discussed in Section 2.2.1.

Velocity measurements were made using a 2D-LDV in turbulent channel flows over a flat stationary sediment bed of different roughness (Parthasarathy & Muste, 1994). The measured normalized mean streamwise velocity agreed well with the log-law. Therefore, the shear velocity can be estimated using the Velocity Profile Method. The lateral change of boundary shear stress and the sidewall effect, however, were not included in their study.

Einstein's graphical division theory discussed in Section 2.3.2 can also be applied to the ice-covered condition. Chen et al. (2015) continued Guo and Julien (2005)'s study, and adopted the two-power law for describing vertical velocity profiles in asymmetric channels to determine the location of zero shear stress. The conformal mapping technique was used to obtain the functional relationship for the division curves within each flow layer. Based on the force balance in each flow subsection, Chen et al. (2015) developed an analytical model for the mean shear stress of channel-bed, ice cover, and sidewall.

Aghaji Zare, Moore, Rennie, Seidou, Ahmari and Malenchak (2015) provided estimates of boundary shear stress on ice cover and channel-bed during stable ice cover and the important stage of ice cover breakup based on continuous field measurements of velocity profiles, obtained with ADCP in the Nelson River in Canada. The boundary shear stress was obtained by fitting velocity profiles into the log-law. Boundary shear stress varied dynamically with the transformation of the ice cover, including the presence and removal of slush ice and formation of the ice jams. Their study focused on the mean shear stress. The bed shear stress during the ice cover period is lower than during the open water condition, meaning that the presence of the upper boundary layer has a diminishing effect on the bed shear stress.

The mean boundary shear stress in ice-covered flow has been studied considerably in recent years, but the local shear stress has barely been investigated. The work of Yamashita, Shimizu and Hohjo (1992) was perhaps the only study related to the local shear stress distribution under the ice-covered condition. They continued the Ray-isovel Approach discussed in Section 2.3.1 and proposed a 2D model, which can determine the complete velocity and boundary shear stress structure in a cross section covered with ice. The 2D model was verified by experimental data obtained from a straight flume covered with a board representing the ice cover. The experiment was conducted using a straight acrylic flume of 7 m long and 0.4 m wide, with well-sorted sand all over the bed and walls. The Laser Doppler Current Meter and Pitot tubes were adopted to measure velocity and boundary shear stress, but the boundary shear stress was only measured at three locations: one near the ice cover, and two close to the channel-bed. The effect of sidewalls is limited to a region of only 15% width from the sidewalls. The calculated bed shear stress showed good agreement with the observed values except for the values close to the sidewalls.

The effects of ice cover on sediment transport have attracted some research interest. For a given flow rate and bed slope, the water depth increases due to the resistance added by the ice cover. The primary effect of this phenomenon is a reduction to the bed shear stress, thereby a reduction to the bed-load transport rate (Smith & Ettema, 1997). The existing open-water procedures for estimating rates of sediment transport were extended to include the effects of ice-covered in alluvial channel flow (Ettema, Braileanu & Muste, 2000).

Ice-covered flows with complex geometries have also been investigated using numerical models. Yoon and Patel (1996) used the k-ω numerical model to describe the flow structure in a dune-bed channel under ice-cover condition. Inkratas, Gharabaghi, Beltaos and Krishnappan (2009) studied distributions of ice-covered flow velocity and the bed shear stress using the k-ε model for a 30 m deep hole in the East Channel of the Mackenzie River.

The formation of ice cover complicates gauging of flow in streams and rivers, causing flow records for many North American streams to contain either gaps or inaccurate winter-flow information (Teal et al., 1994). Cold and miserable working conditions exacerbate measurement difficulties. Moreover, the distribution of ice-covered boundary shear stress has not been thoroughly studied before. Therefore, numerical modelling in this research thesis will be helpful for the understanding of ice-covered flows characteristics.

2.8 Summary

This chapter summarizes five basic methods for determining the boundary shear stress in Section 2.2. Several theories, dating back to the 1930s, about the distributions of local boundary shear stress are discussed in Section 2.3. The development of theoretical ideas has been in progress for almost one hundred years. Researchers are continuously making considerable efforts to develop and improve analytical and numerical models. Most of the existing models cannot incorporate the effects of secondary flow properly. There are still significant discrepancies between model results and experimental data near the corner regions.

Section 2.4 discusses many numerical studies to obtain distributions of boundary shear stress using different CFD techniques, including the traditional RANS models, the most accurate but

computationally expensive DNS, and the LES technique. LES is the core content of this section; most of the existing LES applications in open channel hydraulics have used uniform mesh with coarse resolutions. Uniform mesh is not desirable because of low computation efficiency. The use of coarse resolutions adjacent to the channel-bed and sidewalls impedes resolving the viscous sublayer and prevents the implementation of no-slip condition on boundary surfaces. These are significant deficiencies in current boundary shear stress studies using the LES technique.

All analytical models and numerical methods are subject to experimental verification. Researchers have conducted experimental work extensively in the last few decades. The selection of measurement techniques has always been a tough task. Direct measurements are more accurate but difficult to acquire. Indirect measurements usually involve issues such as intrusive apparatus, expensive costs, and poor mobility. Section 2.5 provides a summary of features of boundary shear stress based on measurements.

Boundary shear stress in the field generally cannot be measured using direct measurements, but can be estimated from the observation of velocity profiles. Section 2.6 describes measurements using different types of equipment. Current meters, ADV, and ADP are common instruments for obtaining velocity profiles. It is understandable that the acquisition of field measurements requires considerable labour and financial resources.

Ice-covered river flows are poorly understood and need further investigations. The distribution of local shear stress along the wetted perimeter under ice-covered condition is almost an unknown domain. The presence of an ice cover makes flow structures more complex. Cold and miserable working conditions make field measurements extremely difficult. Numerical studies, therefore, could be an efficient way for an improved understanding of the distribution of boundary shear stress in ice-covered channels. Section 2.7 contain some details about ice-cover river flows.

We make a new attempt in this research thesis, using the LES technique to obtain distributed boundary shear stress in rectangular and trapezoidal channels under open channel and ice-covered conditions, while avoiding deficiencies seen in previously published studies.

Next chapter gives the modeling methodologies used in this research thesis.

3. Methodologies

3.1 Model channels

This research thesis focuses on computations of shear stresses distributed along the wetted perimeter of a channel cross section (Figure 2.6). Both ice-covered and free surface flow conditions are considered. The former reflects the typical condition of Canadian rivers during the winter season (Figure 3.1), whereas the latter reflects the river flow condition during the other seasons. When a channel cross section is covered with ice, the wetted perimeter consists of the channel-bed, the two sidewalls and the ice cover underside. In the absence of ice cover, it consists of the bed and sidewalls.

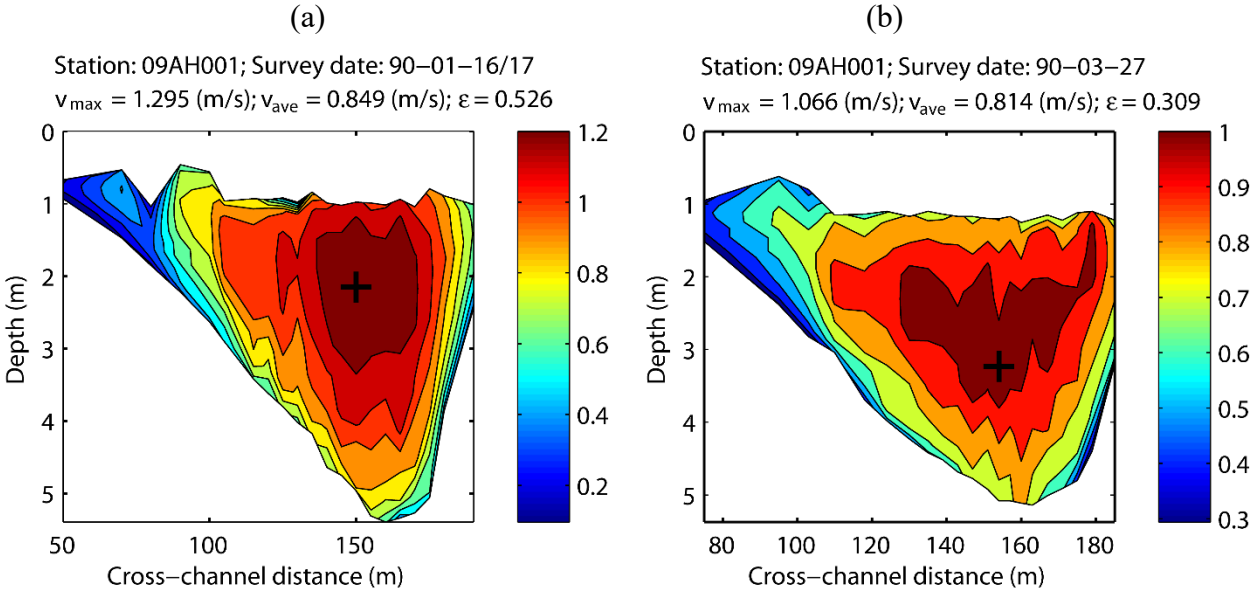

Figure 3.1 Velocity contours showing a single core of high streamwise velocities in a cross section of the Yukon River in Canada, measured in: (a) January 1990; (b) March 1990. The maximum velocity occurred at the location marked by the symbol '+'. The ice cover extended from the zero depth line to the upper edge of the contour region

For shear stress computations, this research thesis uses rectangular and trapezoidal channels of five different geometric configurations that are shown in Figures 3.2 to 3.6, respectively. The rectangular computational channels match Knight et al.'s (1984) experimental channels in cross sectional dimensions. Thus, we can make a comparison of boundary shear stress between computer simulations and laboratory experiments.

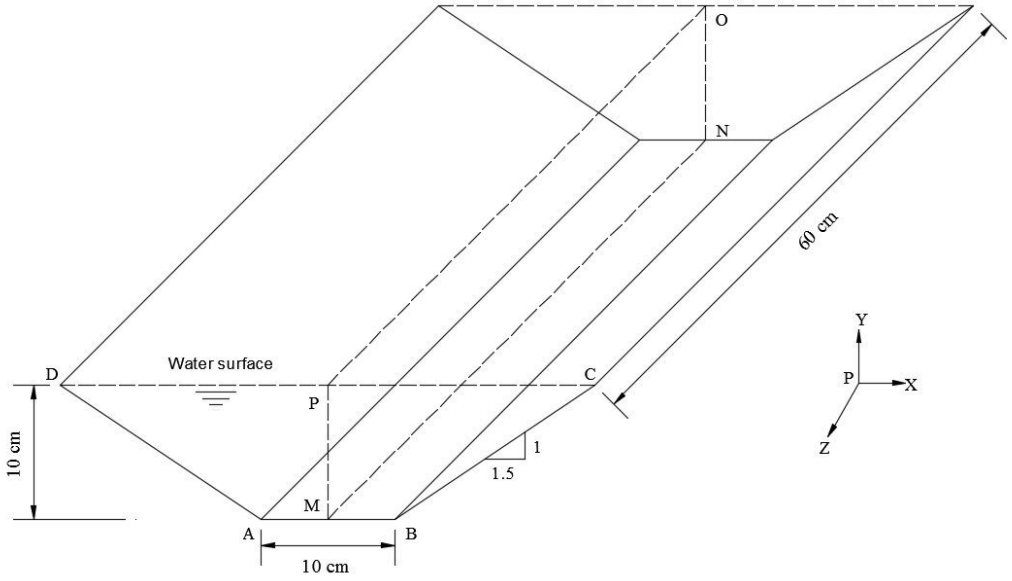

Figure 3.2 An open channel of trapezoidal shape, for large eddy simulation (LES) of the flow field, and boundary shear stresses at the channel-bed and sidewalls. The length of the computational channel is taken as six times its depth

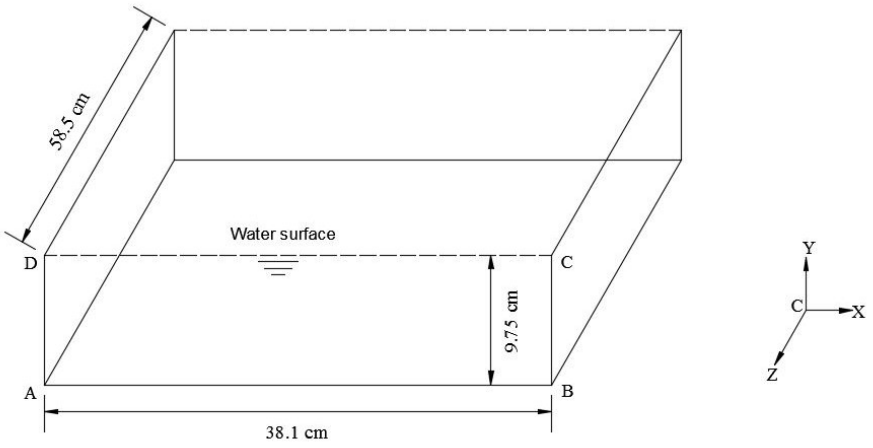

Figure 3.3 An open channel of rectangular shape, for LES of the flow field, and boundary shear stresses at the channel-bed and sidewalls. This computational channel matches Knight et al.'s (1984) experimental channel in cross-sectional dimensions, which allows a data comparison. The length of the computational channel is taken as six times its depth

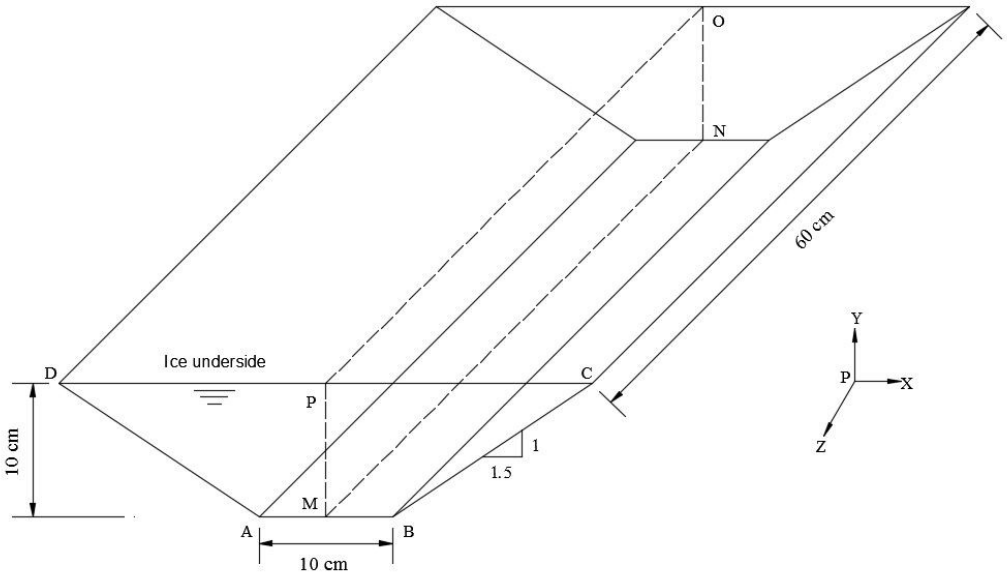

Figure 3.4 An ice-covered channel of trapezoidal shape, for LES of the flow field, and boundary shear stresses at the channel-bed and sidewalls. This channel has the same dimensions as the channel shown in Figure 3.2

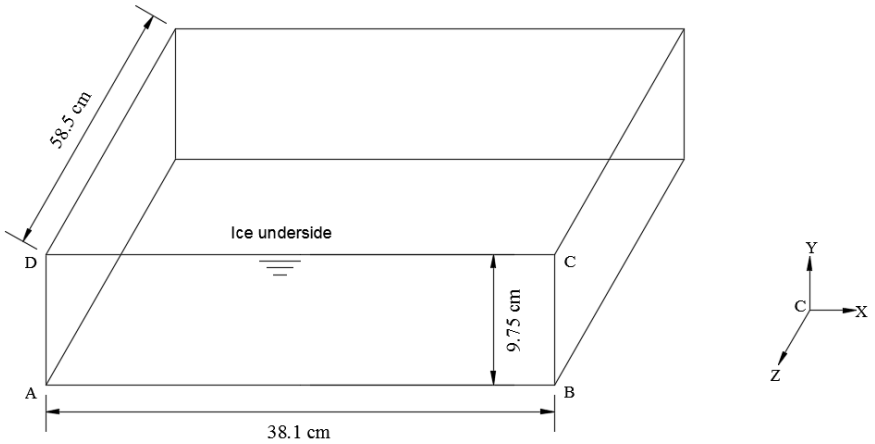

Figure 3.5 An ice-covered channel of rectangular shape, for LES of the flow field, and boundary shear stresses at the channel-bed and sidewalls. This channel has the same dimensions as the channel shown in Figure 3.3

(a)

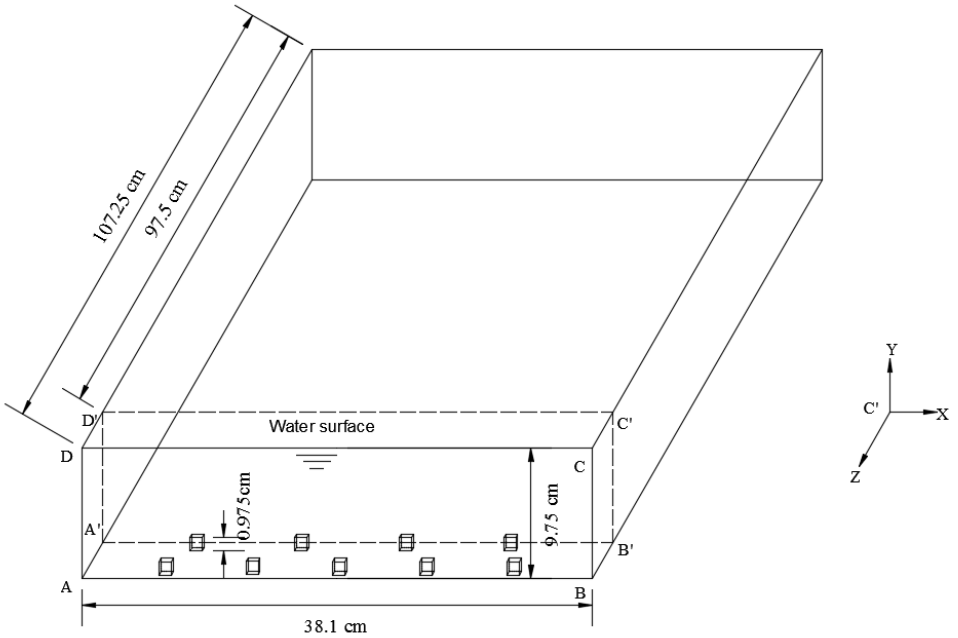

(b)

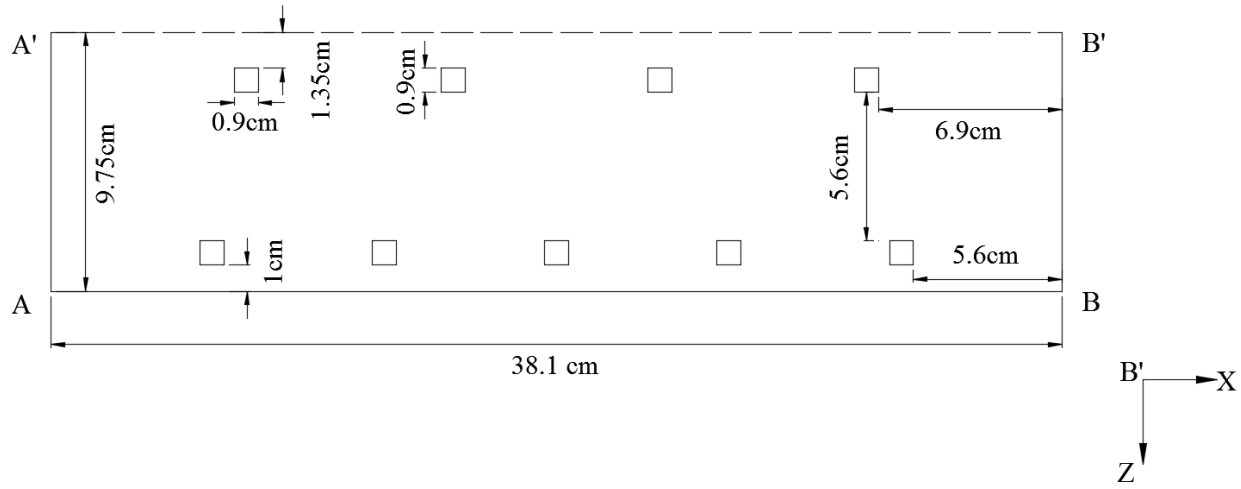

Figure 3.6 A rectangular channel for LES of the flow field and boundary shear stresses: (a) 3D view of the channel; (b) top view of blocks attached to the bed near the upstream end of the channel. This channel matches Knight et al.'s (1984) experimental channel in cross-sectional dimensions

The geometric configurations shown in Figures 3.2 to 3.6 are referred to as Cases 1 to 5, respectively. For these cases, the setup for shear stress computations is summarised in Table 3.1. Case 1 and Case 3 assume domain symmetry, meaning that the flow field is considered

symmetrical about the vertical plane OPMN (Figure 3.2 and Figure 3.4) through the channel centreline. Accordingly, computations need to be performed for only half of the model channels. The symmetry assumption reduces computing costs. For all the cases, the lengths of the computational channels are taken as multiple times the depth of flow. The idea is to minimise possible end effects caused by the upstream and downstream lateral open boundaries of the water channels. The inlet velocity imposed at the upstream boundary, discharge, and cross section dimensions match Knight et al.'s (1984) experimental conditions.

Table 3.1 A summary of channel geometry and setup for LES. Cases 1 to 5 correspond to the model channels shown in Figures 3.2 to 3.6, respectively

Case	Channel shape	Ice	Domain symmetry	Length-to-depth ratio	Inlet velocity (cm/s)	Discharge (litre/s)	Reynolds number	Boundary condition
1	trapezoidal	no	yes	6	5.0	1.25	10^4	UDF
2	rectangular	no	no	6	49.5	13.30	10^5	UDF
3	trapezoidal	yes	yes	6	5.0	1.25	10^4	UDF
4	rectangular	yes	no	6	49.5	13.30	10^5	UDF
5	rectangular	no	no	11	49.5	1.25	10^5	periodic

The Reynolds number, Re_L, is expressed as $\mathrm{Re}_L = \frac{U_o L}{\nu}$, where U_o is the characteristic velocity, L is the characteristic length, and ν is the kinematic viscosity of water. Re_L can be evaluated by taking the inlet velocity as U_o, and twice the depth (Figures 3.2 to 3.6) as L. The Re_L values are of the order of 10^4 to 10^5, which indicate turbulent flow in the model channels.

With regard to the condition imposed at the upstream boundary of the channel in question, we test both a user defined function (UDF) and a periodic boundary condition (Table 3.1, Case 5).

In summary, Case 1 is an open channel of trapezoidal shape (Figure 3.2). Case 2 is an open channel of rectangular channel (Figure 3.3). Cases 3 and 4 (Figures 3.4 and 3.5) consider the presence of a smooth ice cover in the model channels for Case 1 and Case 2, respectively. The ice underside is

a solid, no-slippery wall. Case 5 (Figure 3.6) extends the model channel for Case 2 by five times the depth of flow. In the model channel for Case 5, small cubical obstructs are placed on the channel-bed near the upstream boundary, in order to enhance the level of turbulence. Their dimensions are 10% of the depth of flow. Turbulent flow and shear stresses in the above-mentioned channels are obtained through LES. Pertinent model equations are described in the next section.

3.2 Model Equations

Fluid flows are governed by a coupled set of partial differential equations, known as the Navier-Stokes equations. Computational fluid dynamics (CFD) models numerically solve these equations of different forms, depending on the types of numerical techniques used. For example, direct numerical simulation (DNS) numerically solves the instantaneous Navier-Stokes equations of transient form by means of spectral technique. Reynolds-averaged Navier-Stokes (RANS) equation models separate an instantaneous flow variable into a mean part and a fluctuating part, and apply temporal averaging to the Navier-Stokes equations. These models require to parameterise unresolved fluctuations with the help of Boussinesq approximation, and to use appropriate turbulence closure schemes.

3.2.1 Filtered Navier-Stokes Equations

LES uses filtering techniques to filter out motions of scales smaller than the mesh size used. In other words, motions of sub-grid scales are separated from those of resolvable scales. This is the first step in realising LES. A general expression for a filtered variable $\overline{\Phi}(x)$ (denoted by an overbar) is given by:

[3.1] $$\overline{\Phi}(x) = \int_D \Phi(x')G(x,x')dx'$$

where x represents is the location where $\overline{\Phi}(x)$ is to be determined; x' is the location where $\Phi(x)$ is considered in the spatial integration; D donates the flow domain; G is the filter function that determines the scale of the resolved eddies (Rodi, Constantinescu, & Stoesser, 2013, p.17). Many filters have been proposed in the literature, including the simple volume-average box filter of Deardorff (1970), and the Fourier cutoff filter and Gaussian filter of Ferziger and Shaanan (1976).

This LES study uses the Fluent software package (ANSYS, 2013b, p. 702). The finite-volume discretisation itself implicitly provides the filtering operation. After the filtration, the governing equations become the filtered Navier-Stokes equations for mass conservation and momentum balance, given by:

[3.2] $$\frac{\partial \overline{u}_i}{\partial x_i} = 0$$

[3.3] $$\frac{\partial \overline{u}_i}{\partial t} + \frac{\partial}{\partial x_j}\left(\overline{u_i u_j}\right) = -\frac{1}{\rho}\frac{\partial \overline{p}}{\partial x_i} + \nu \frac{\partial}{\partial x_j}\left(\frac{\partial \overline{u}_i}{\partial x_j}\right) + \rho g_i$$

where $\overline{u}_i$ denotes the resolvable-scale filtered velocity; x_i represents the Cartesian coordinates; i = 1, 2 and 3 corresponds to the spanwise (x), the vertical (y) and the streamwise (z) directions, respectively (Figures 3.2 to 3.6); t is the time; $\overline{p}$ is the resolvable pressure; and g_i is the gravitational acceleration. For a channel-bed with an angle θ to the horizontal, g_i = (0, $-g\cos\theta$, $-g\sin\theta$).

In Equation [3.3], on the left hand side, the first term expresses the rate of change of resolved velocity. The second term is a convection term. These two terms can be interpreted as the inertial forces. On the right hand side, the first term represents the pressure gradient. The second term is a diffusion term, associated with viscous forces. The third term is external forces applied to the fluid.

The convective flux is given by:

[3.4] $$\overline{u_i u_j} = \overline{u}_i \overline{u}_j + L_{ij} + C_{ij} + R_{ij}$$

which contains the Leonard stress term:

[3.5] $$L_{ij} = \overline{\overline{u}_i \overline{u}_j} - \overline{u}_i \overline{u}_j ;$$

the cross-term stress term:

[3.6] $$C_{ij} = \overline{\overline{u}_i u'_j} + \overline{\overline{u}_j u'_i} ;$$

and the subgrid-scale Reynolds stress term:

[3.7] $$R_{ij} = \overline{u'_i u'_j}$$

where u_i', u_j' are Subgrid-scale velocities in tensor notation. These three quantities (Equations [3.5] – [3.7]) describe the interaction of fluctuations of the larger-scale resolvable field, the interaction

of resolvable and unresolvable fluctuations, and the interaction of unresolvable fluctuations, respectively. What is important is to obtain accurate estimates of their sum. This can be expressed using the subgrid-scale stress tensor, defined as:

[3.8] $$\tau_{ij} = \overline{u}_i \overline{u}_j - \overline{u_i u_j}$$

Physically, Equation [3.8] represents the effect of the unresolved fluctuations on the resolved motion. The subgrid-scale stresses are analogous to the Reynolds stresses. The difference is that the latter represents the effect of entire turbulent fluctuations on the mean motion, whereas the former only represents the effect of the small-scale motions.

Equation [3.3] can be rewritten as:

[3.9] $$\frac{\partial \overline{u}_i}{\partial t} + \frac{\partial}{\partial x_j}\left(\overline{u}_i \overline{u}_j\right) = -\frac{1}{\rho}\frac{\partial P}{\partial x_i} + \frac{\partial}{\partial x_j}\left(\nu \frac{\partial \overline{u}_i}{\partial x_j} + \tau_{ij}\right)$$

where $\tau_{ij} = -(Q_{ij} - Q_{kk}\delta_{ij}/3)$; $P = \overline{p} + \rho Q_{kk}\delta_{ij}/3$, δ_{ij} being equal to one for $i = j$ and zero for $i \neq j$; $Q_{ij} = R_{ij} + C_{ij}$. The subgrid-scale stress tensor τ_{ij} is split into an isotropic component and an anisotropic component. The isotropic part $Q_{kk}\delta_{ij}/3$ contains the sum of the subgrid-scale normal stresses which is twice the kinetic energy of the subgrid scale fluctuations and acts like a pressure. This component is therefore usually added to the filtered pressure term, which leads to a new pressure variable P.

3.2.2 Sub-grid Model

Clearly, a fundamental problem of LES is to establish a satisfactory model for the subgrid scale stresses as represented by the stress tensor Q_{ij}. Previous researchers have proposed a number of models, including the simple gradient diffusion model of Smagorinsky (1963), the one-equation model of Lilly (1966), the second order closure model of Deardorff (1973), and the nonlinear stress-strain rate relationships of Bardina et al. (1983).

This research thesis uses the Smagorinsky-Lilly model (Smagorinsky 1963; Lilly 1966) for estimates of the subgrid scale stresses. Smagorinsky (1963) assumed that τ_{ij} followed a gradient-diffusion process similar to molecular motion. In analogy to the viscous stress in laminar flows (Equation [2.9]), τ_{ij} is approximated by relating it to the resolved strain rate, S_{ij}, which involves

velocity gradients via an artificial eddy viscosity ν_τ, called Smagorinsky eddy viscosity, expressed as:

[3.10] $$\tau_{ij} = 2\nu_\tau S_{ij}$$

where $S_{ij} = \frac{1}{2}\left(\frac{\partial \overline{u}_i}{\partial x_j} + \frac{\partial \overline{u}_j}{\partial x_i}\right)$. Here, the eddy viscosity ν_t is not a fluid property but characterises the unresolved sub-grid-scale fluctuations and depends on the resolved velocity field, $\overline{u}_i$.

On the basis of dimensional analysis, the eddy viscosity can be expressed as:

[3.11] $$\nu_\tau = L_s q$$

where L_s is the mixing length; q is the velocity scale of sub-grid scale motions. The selection of L_s in LES is simple and straightforward. The largest scales of the unresolved turbulence, which interact most actively with the resolved motion, are of the size of the filter width Δ. This parameter is also known as the grid scale. It is an overall scale of the subgrid-scale motion, equal to $(\Delta_1\Delta_2\Delta_3)^{1/3}$ if the grid dimensions in the three coordinate directions are different. Hence, the characteristic length-scale in the Smagorinsky model is expressed as:

[3.12] $$L_s = C_s\Delta$$

where C_s is the Smagorinsky coefficient, whose value can be obtained from theoretical considerations.

The determination of q can use analogy to Prandtl's mixing length theory, with the advantage that in LES the length scale is known already. Combined with Equation [3.12], this leads to:

[3.13] $$q = L_s\left|S_{ij}\right| = C_s\Delta\left|S_{ij}\right|$$

where $\left|S_{ij}\right| = \sqrt{2S_{ij}S_{ij}}$. Combining Equations [3.11] and [3.13] yields

[3.14] $$\nu_\tau = (C_s\Delta)^2\sqrt{2S_{ij}S_{ij}}$$

The model has only one adjustable parameter, the Smagorinsky constant C_s, whose effect on the statistics of the flow vanishes when decreasing the filter width. An improved formulation of ν_τ incorporating the dynamics of the subgrid scales presented by Lilly (1966) is given by:

[3.15] $$\nu_\tau = C_L \Delta q$$

where C_L is a closure coefficient, and q^2 is the subgrid-scale kinetic energy. A partial differential equation for q^2 is derived from a moment of the Navier-Stokes equation. This partial differential equation contains several terms that need to be modelled. The treatment is very similar to Prandtl's one equation model.

In this research thesis, the form of Equation [3.14] for Smagorinsky eddy viscosity is rewritten as:

[3.16] $$\nu_\tau = L_s^2 \sqrt{2 S_{ij} S_{ij}}$$

[3.17] $$L_s = \min(C_s V^{1/3}, \kappa d)$$

where d is the distance to the closest wall, and V is the volume of the computational cell. According to Rogallo and Moin (1984), C_s values range from 0.10 to 0.24. Lilly (1966) suggested a C_s value of 0.17. A C_s value of 0.1 has been found to yield the best results for a wide range of flows, this value is used for all the simulations in this research thesis.

3.3 Numerical Techniques

This section gives a description of the numerical techniques used in order to obtain numerical solutions to governing equations [3.2] and [3.9] on the model domains shown in Figures 3.2 to 3.6. For this purpose, the governing equations, along with all the auxiliary relations involved, as well as the model domains must be discretised.

3.3.1 Discretization Methods

The governing equations are discretised using the finite volume method (FVM), which is one of the most versatile discretisation techniques in CFD. It involves dividing the computational domain into a number of control volumes or cells. As an example, the discretisation of the model channel plotted in Figure 3.2 for Case 1 (Table 3.1) is shown in Figure 3.7. The cells are non-staggered, or co-located grids, meaning that variables of interest like pressure and velocity components are stored at the centroid of each control volume or cell. The governing equations of differential form (Equations [3.2] and [3.9]) are integrated over each cell to yield algebraic equations for the discrete dependent variables such as velocities and pressure. Then, interpolation profiles are applied to

describe the variation of variable between cell centroids. The resulting solution must satisfy the conservation of mass and momentum.

An advantage of the FVM is that it only needs to evaluate fluxes through cell boundaries. For transient simulations, the governing equations need to be discretised in both space and time. A proper mesh is critical for the success of LES. We divide the individual model channels into a number of smaller elements and increase the local accuracy by refining the mesh. Note that a coarse mesh with few nodes may lead to a quick solution but inaccurate results, whereas a dense mesh might provide fairly good results but incurs excessively high computational costs and difficulties. In this research thesis, we achieve a balance. We generate dense mesh in the areas of interest, including corners and near-wall areas (Figure 3.7) where large variations of fluid properties are expected, and generate coarse mesh in other areas where there is not much variation expected in the fluid properties.

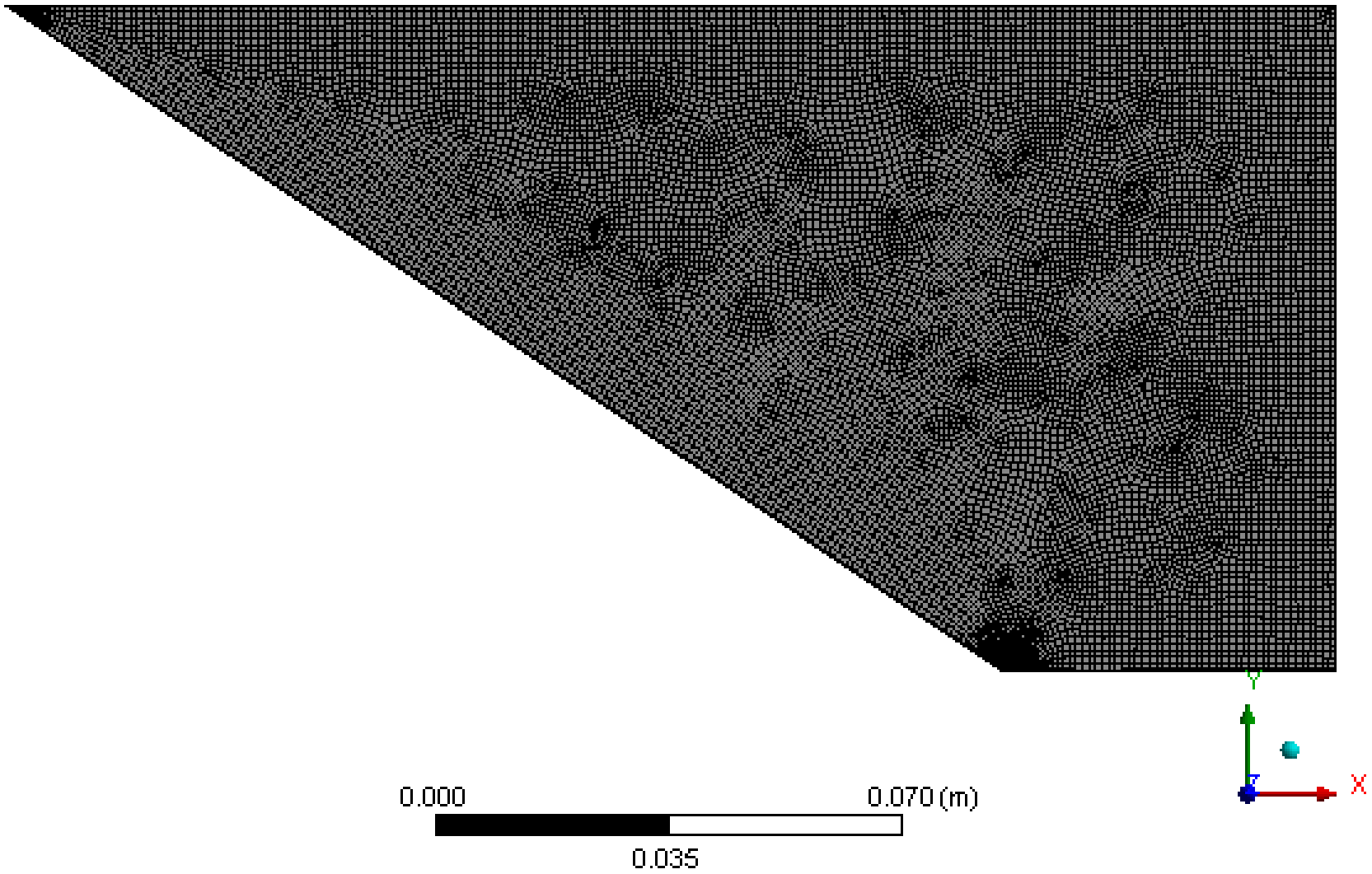

Figure 3.7 Cross-sectional view of the finite volume mesh that covers the model channel (Figure 3.2) for Case 1 (Table 3.1). The flow of water in the model channel is considered symmetrical about the vertical plane OPMN (Figure 3.2)

In this research thesis, we use both structured and unstructured mesh for different cases, and pay close attention to the quality of the mesh. A structured mesh has regular connectivity, with cells arranged in rows and columns. The type of elements includes hexahedron for 3D geometry. An unstructured has irregular connectivity. The type of elements includes tetrahedrons for 3D geometry. Unstructured tetrahedral mesh might use up to several times as many elements as structured hexahedral mesh, and thus is more computationally expensive for the same geometry. A structured mesh is highly space efficient and offers better convergence and higher resolution, but may be difficult to cover a complicated computational domain. An unstructured mesh is generally more flexible because the connectivity pattern is not fixed. We test the sensitivity of LES predictions to slight changes in mesh size and configurations.

Temporal discretisation involves the integration of every term in the model equations over a time step Δt. We use a time step small enough to achieve numerical stability and to enhance prediction accuracy, capturing key flow features in each cell. We estimate the appropriate time step based on the Courant number, *C*, defined as

[3.18] $$C = \frac{U_3 \Delta t}{\Delta}$$

where U_3 is the streamwise bulk mean velocity, Δt is the maximum time step, and Δ is the spacing of the grid in the numerical model parallel to the direction of flow. For all the simulations, we choose a time step that satisfies the restriction that the Courant number is smaller than unity.

3.3.2 Solution Algorithm

In this study, we solve the integral form of Equation [3.2] and Equation [3.9] using the FVM technique. The discrete values of dependant variables are stored at the cell centers (c_0 and c_1), as illustrated in Figure 3.8 (ANSYS, 2013a, p. 632). The solution procedures involve the pressure field, and the spatial gradients of all the variables at the faces of the cell in question. The procedures also require the selection of the appropriate convection scheme. Thus, it is necessary to estimate interfacial values of the involved variables from their cell central values.

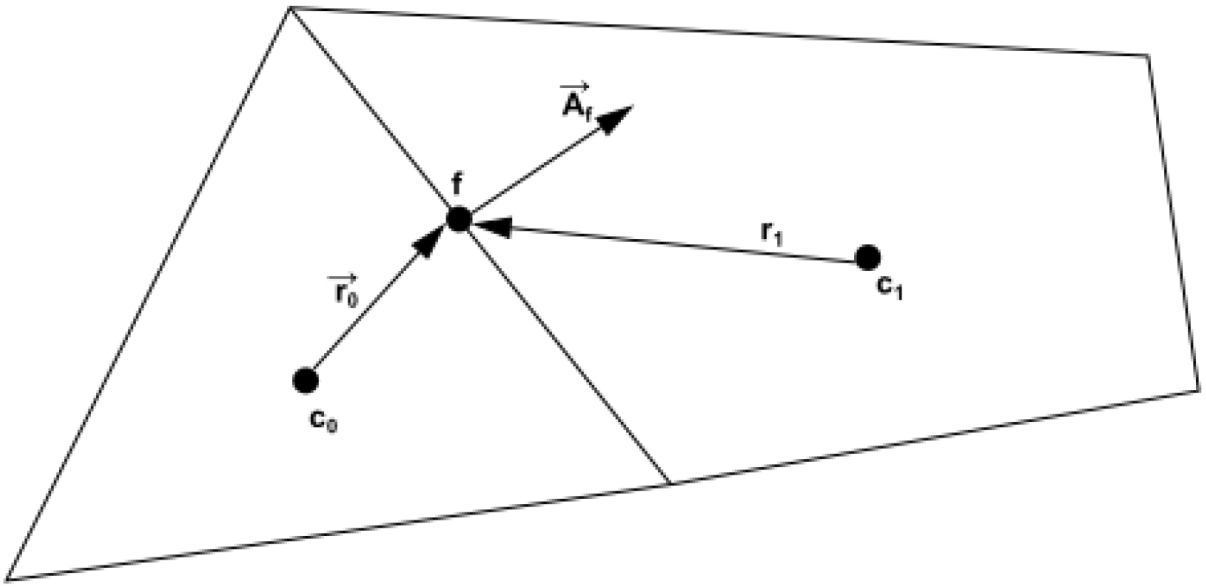

Figure 3.8 Control volume used to illustrate discretisation of a scalar transport equation, where c_0 and c_1 mark the locations of the centres of two adjacent cells, and *f* denotes the interface between them (ANSYS, 2013a, p. 632)

The gradients are used to construct values of a scalar at cell faces (e.g. face *f* in Figure 3.8), and to compute secondary diffusion terms (e.g. $\nu \frac{\partial}{\partial x_j}\left(\frac{\partial \overline{u}_i}{\partial x_j}\right)$ in Equation [3.9]) and velocity derivatives (e.g. $\frac{\partial \overline{u}_i}{\partial x_i}$ in Equation [3.2]). The accuracy of the least squares cell based method is satisfactory and is relatively less expensive. Therefore, this method is used for the calculation of gradients in this research thesis.

The face values of variables such as velocities and pressure are needed for the calculation of convection terms (e.g. $\frac{\partial}{\partial x_j}\left(\overline{u}_i \overline{u}_j\right)$ in Equation [3.9]). We use the second order scheme to reconstruct the face pressure. This is a central differencing scheme, which improves the accuracy of computations.

We use the bounded central differencing scheme to solve the momentum equations (Equation [3.9]) in this research thesis. This method produces face values for all the variables except the pressure field in the equations.

Because of the temporal development, we use the unsteady solver, the bounded second-order implicit method is used to integrate the differential equations over time (e.g. $\frac{\partial \overline{u}_i}{\partial t}$ in Equation [3.9]). This method has the advantage of maintaining unconditional stability with respect to time step.

The flow is incompressible. Accordingly, we select the pressure-based solver to interpolate and solve the discretised equations generated by the FVM. In the pressure-based approach, the constraint of mass conservation (Equation [3.2]) of the velocity field is achieved by solving a pressure equation. This equation is derived from Equation [3.2] and Equation [3.9]. The velocity field such obtained, corrected by the pressure, satisfies the continuity principle. As a result, the governing equations (Equation [3.2] and Equation [3.9]) are nonlinear and coupled to one another.

The solution to these nonlinear equations involves iterations until the convergence criterion is met (10^{-6}). To save computing costs, we use the pressure-velocity coupling method to solve the governing equations in a coupled manner (simultaneously). LES usually requires a small time step. For fast convergence, we choose the SIMPLE algorithm, which is one of the pressure-velocity coupling methods. It is possible to adjust under-relaxation factors to facilitate convergence (ANSYS, 2013b, p. 1418).

The solution is considered converged when residuals (measures of the overall conservation of the flow properties) are very small. A large number of iterations are usually required to reach a converged solution. At each iteration, the residual sum for each of the conserved variables is computed and stored, giving a convergence history. The residuals decrease to small values and no longer change.

This study aims to produce high resolution results. With the limitation of computing power, the convergence criteria of all equations are set to 10^{-6}, and the minimum number of iterations is set to 120. A summary of solution methods is given in Table 3.2.

Table 3.2 Solution methods used in LES computations

Solution methods		
Pressure-velocity coupling method	Simple algorithm	
Spatial discretization scheme	Gradient	Least squares cell based method
	Pressure	Second order scheme
	Momentum	Bounded central difference scheme
Transient formuation scheme	Bounded second-order implicit method	

3.4 Boundary Conditions

At the boundaries of the model channels (Figures 3.2 to 3.6), conditions of flow variables must be specified. These boundaries include the channel-bed, sidewalls, the underside of ice if it exists, the free surface in the absence of ice, the inlet at upstream, and the outlet at downstream.

3.4.1 Boundary Condition at the Channel-bed and on the Sidewalls

The channel-bed is a solid wall. For all the five cases (Table 3.1), no-slip condition is specified at the wall. The fluid sticks to the wall and moves with the same velocity as the wall. Because the channel-bed and sidewalls are stationary, the fluid velocity at the wall is zero:

[3.19] $$\overline{u}_i = 0$$

where $\overline{u}_i$ is the resolved velocity in tensor notation, and i = 1, 2 and 3 corresponds to the spanwise (x), the vertical (y) and the streamwise (z) directions, respectively. Note that we resolve the viscous sublayer in this LES study. The wall shear stress is obtained from the linear stress-strain relationship given in Equation [2.11]. Combining this equation with Equation [2.1], gives a resultant a relationship between the velocity gradient and the wall shear stress:

[3.20] $$\tau_0 = \mu \frac{\overline{u}_3}{y}$$

where $\overline{u}_3$ is the resolvable filtered velocity in streamwise direction (Figure [3.2]). The no-slip wall condition [3.19] is also applied on the sidewalls.

3.4.2 Boundary Conditions at the Ice Underside

The underside of ice (Figure 3.1) is treated as a solid wall. Thus, the no-slip wall condition [3.20] is applied at the ice underside.

3.4.3 Boundary Condition at the Free Surface

For Case 1, Case 2, and Case 5 (Table 3.1), the *x*, *y*, and *z* components of the shear stress specified at the free surface (Figures 3.2 to 3.4) are zero:

[3.21] $$\tau_{ij} = 0$$

where τ_{ij} is the shear stress anywhere in fluid. Essentially, the streamwise and lateral velocities of the fluid near the free surface are not retarded by the boundary.

For Case 5 (Table 3.1), a symmetry condition is imposed at the free surface. This is to say that there is a zero flux of all quantities across the boundary. The velocities normal to the free surface are set to zero, and values of all other properties outside the model domain are equated to their values at the nearest node just inside. Zero normal gradients of all variables are set at the symmetry plane.

3.4.4 Boundary Condition at the Inlet

At the inlet (Figures 3.2 to 3.6), inflow velocities are defined. The inflow is normal to the inlet. For Cases 1 to 4 (Table 3.1), the inflow is given in terms of velocity profiles as user defined functions (UDF). This treatment accelerates flow development and reduces computing time. We test the performance of a 1/7 power law for free surface flow and a two-power law for ice-covered flow:

[3.22] $$\frac{\overline{u}_3}{U_3} = \left(\frac{y}{h}\right)^{1/7} \qquad \text{(UDF for free surface flow)}$$

[3.23] $$\frac{\overline{u}_3}{U_3} = k_0\left(\frac{y}{h}\right)^{1/m_i}\left(1-\frac{y}{h}\right)^{1/m_b} \qquad \text{(UDF for ice-covered flow)}$$

where U_3 is the bulk mean velocity in the streamwise direction, and h is the depth of flow; k_o is a parameter related to per-unit-width discharge; m_i is a parameter associated with the frictional effect of ice; m_b is a parameter associated with the frictional effect of the bed. According to Attar and Li (2012), for a smooth ice cover, m_i is equal to 1/7, and m_b is equal to 1/4.

The value of bulk mean velocity U_3 in Equations [3.22] and [3.23] is estimated as

[3.24] $$U_3 = Q / A$$

where Q is the discharge; and A is the cross-sectional area.

To reflect the condition of turbulence at the inlet, we specify the magnitude of fluctuations in velocity components. We adopt the spectral synthesizer to generate fluctuating velocity components. The intensity of turbulence and the turbulent viscosity ratio are both set to 10%.

The Cartesian coordinates system is used, with the z-axis pointing positively in the streamwise direction (along the channel-bed) against the main flow, the y-axis pointing positively upward in the vertical direction (perpendicular to the bed), and the x-axis in the lateral direction (Figures 3.2 to 3.6). Ten vertical profiles of the streamwise velocity component at selected lines are plotted in Figures 3.9 to 3.13 for Cases 1 to 5, respectively. These selected lines are the central lines at the middle of the inlet and outlet cross sections for all five cases (plotted in red and blue colours, respectively).

In Figure 3.9 (Case 1), Figure 3.10 (Case 2) and Figure 3.13 (Case 5), the streamwise velocity profiles at the inlet planes use the 1/7 power law (Equation [3.22]) for open channels. In ice-covered cases (Case 3 and Case 4), we specify the two-power law Equation [3.23] for the vertical distributions of streamwise velocities at the inlet planes (Figure 3.11 and Figure 3.12). In comparison to rectangular channel sections, trapezoidal channel sections show stronger spatial fluctuations in velocity components at the inlet planes.

Figures 3.9 to 3.13 also show streamwise velocity profiles at the outlet planes. For Cases 1 to 4, the velocity profiles change along the channel as a result of the boundary conditions. The velocity profiles between the inlet and outlet planes have some differences in pattern. However, the velocity

profiles for case 5 are the same between the inlet and outlet planes by definition, and only the vertical coordinate changes slightly because of the slope of the channel geometry.

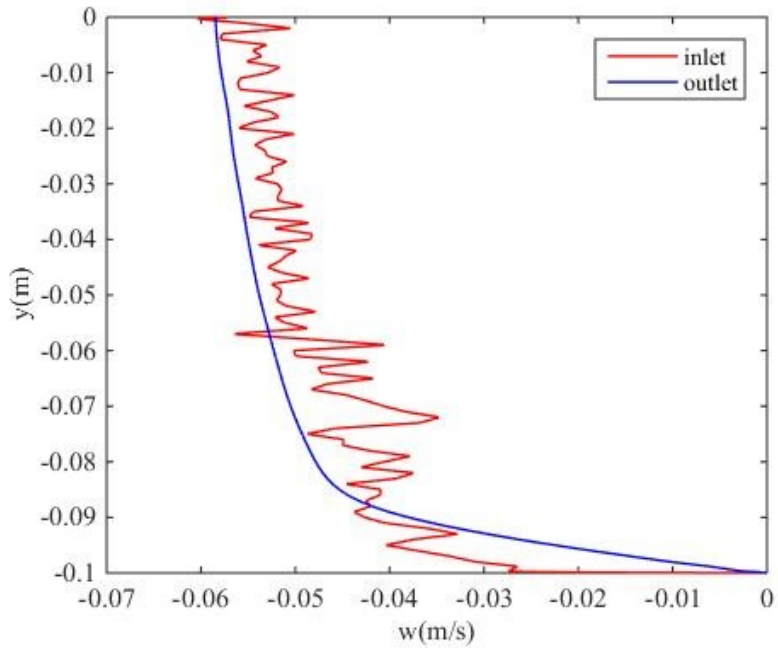

Figure 3.9 Vertical profiles of the streamwise velocity component at an inlet location (the red curve) and an outlet location (the blue curve) for Case 1

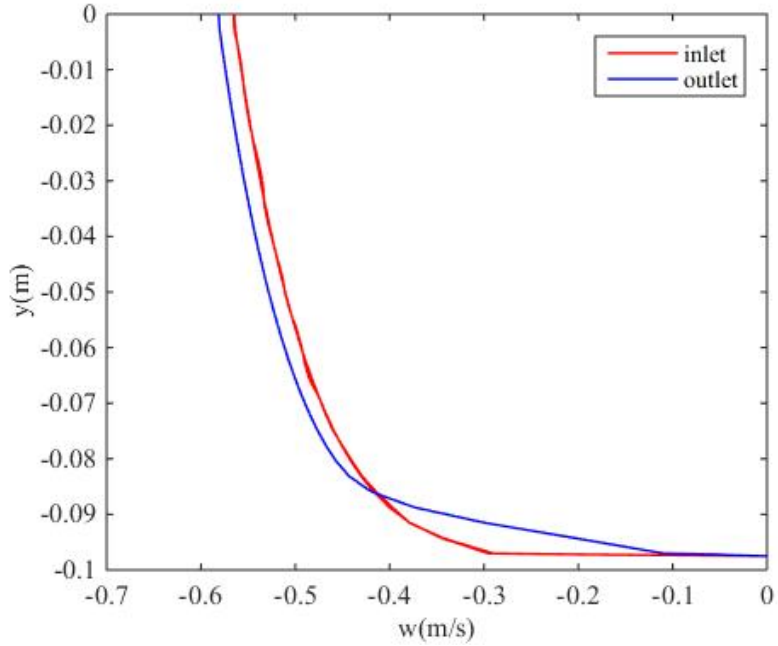

Figure 3.10 Vertical profiles of the streamwise velocity component at an inlet location (the red curve) and an outlet location (the blue curve) for Case 2

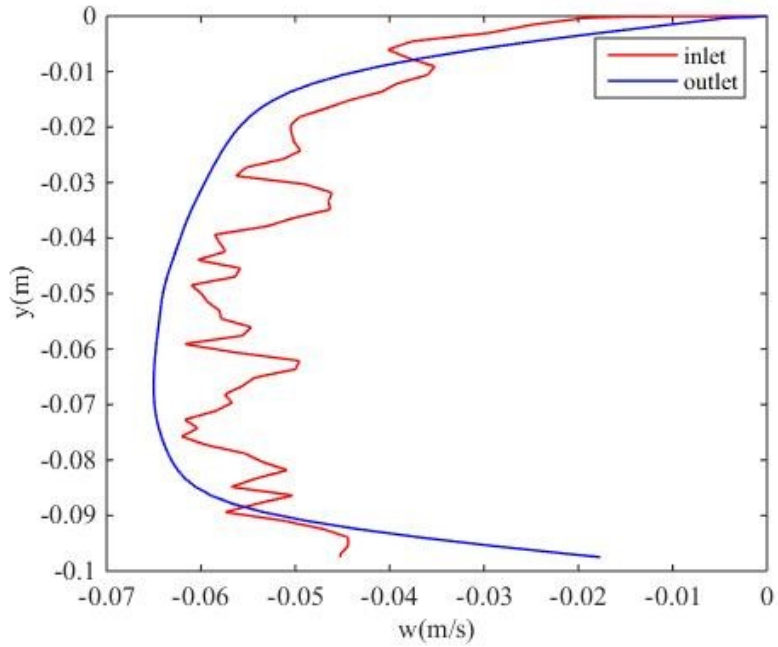

Figure 3.11 Vertical profiles of the streamwise velocity component at an inlet location (the red curve) and an outlet location (the blue curve) for Case 3

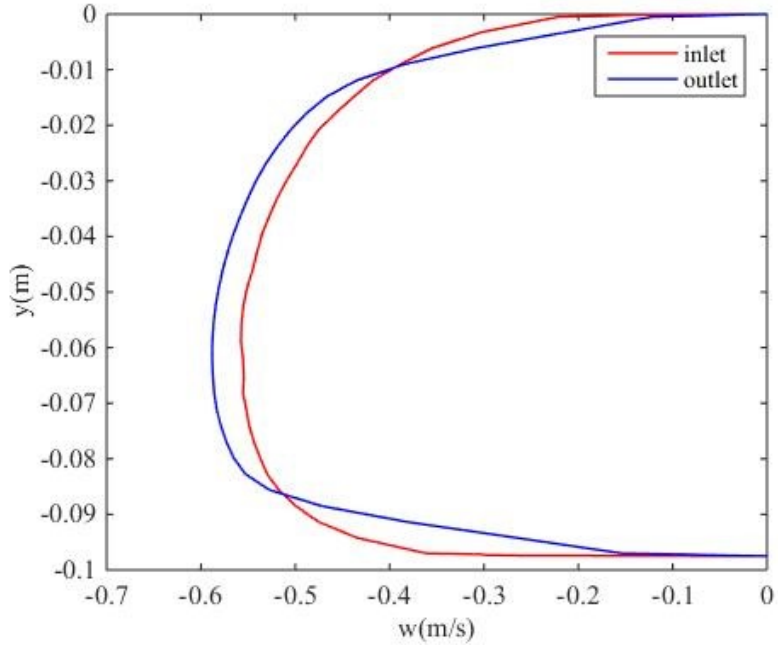

Figure 3.12 Vertical profiles of the streamwise velocity component at an inlet location (the red curve) and an outlet location (the blue curve) for Case 4

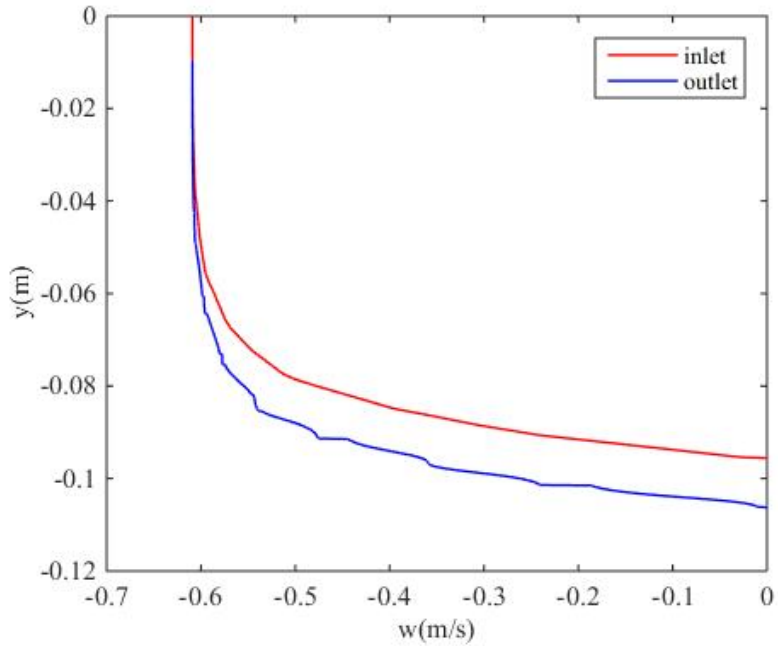

Figure 3.13 Vertical profiles of the streamwise velocity component at an inlet location (the red curve) and an outlet location (the blue curve) for Case 5

3.4.5 Boundary Condition at the Outlet

It is very important to place the outlet at an appropriate location such that the conditions downstream have no influence on the solution for the interior of the model domain. At the outlet, the gradients of all variables (except pressure) are zero in the flow direction. Pressure outlet boundary condition is applied at the outlet for Case 1 to Case 4. This requires the specification of a static (gauge) pressure at the outlet boundary. This pressure is set to zero. It means that the pressure distribution is hydrostatic at the downstream lateral open boundary (or the outlet).

3.4.6 Periodic Boundary Condition

For Case 5, a periodic boundary condition is applied between the inlet and outlet. The periodic type is translational. The idea is to achieve fully developed flow more efficiently. A mass flowrate of 18.34 kg/s is specified, to express the flow in the channel, as estimated based on the discharge (Table 3.1). An initial guess of the pressure gradient is zero. The sub-iterations number is set to two to help the pressure correction and improve the value of pressure gradient. The relaxation factor used is an under-relaxation factor that controls convergence of this iteration process. This factor is set to 0.5. On the coordinates shown in Figure 3.6, the flow direction is specified as (0, −0.0299, −0.999), as estimated from the slope of 0.01.

A prerequisite for the application of periodic boundary condition is that the mesh with translationally periodic boundaries should be parallel to each other and equal in size. This prerequisite is not fulfilled for Case 5, where the nodes on the inlet and outlet are not coincident because the nine blocks added near the inlet change the mesh configuration. We overcome the difficulty by, first, changing the boundary type of inlet and outlet boundaries into interfaces, and then making the interfaces into a non-conformal periodic zone.

3.5 Initial Conditions

In a simulation of transient flow, initial conditions are given to indicate the state of fluid flow at the time when the computation starts. At model time of $t = 0$, initial values of flow variables are specified to all computational volumes in the geometry. The specification of proper initial values can accelerate the simulation considerably. For Cases 1 to 4, we estimate the initial values from the inlet velocity profile as:

[3.25] $\bar{u}_1 = 0;\ \bar{u}_2 = 0;$

[3.26] $\bar{u}_3 = 0.050\,(\text{m/s})$ for Case 1 and Case 3

[3.27] $\bar{u}_3 = 0.495\,(\text{m/s})$ for Case 2 and Case 4

For Case 5 (Figure 3.6, Table 3.1), the sloping bed surface has an angle θ to the horizontal axis, and the corresponding gravity components are g_i = (0, $-g\cos\theta$, $-g\sin\theta$). At time t = 0, the initial flow velocities in all the grids are set to the mean flow velocity, whose components are (0, −0.0299, −0.9995), as estimated from the slope of 0.01. It is understood that the calculations for the periodic zone are less accurate.

3.6 Summary

In this LES study, the computational procedures involve creating the channel geometry, generating mesh for the channel, setting up initial and boundary conditions, performing iterations, and post-processing output results. The motions of large eddies are computed using adequately fine grids, whereas the motions of the small, subgrid-scale eddies are modelled. The large eddy motions must be computed, because they are directly affected by boundary conditions, and carry most of the Reynolds stresses. The small eddies are expected to be isotropic and relatively weak. They have nearly universal characteristics, and contribute less to the Reynolds stresses. As a result, their motions are less critical and more amenable to modelling. Some highlights of the differences in behaviour between large and small eddies are given in Table 3.3

The LES technique is essentially a compromise between RANS and DNS approaches. LES solves the 3D time-dependent flow equations much like DNS, but the solutions are limited to the large-scale motions. In contrast to the RANS model, which must account for the effect of the entire spectrum of the turbulent motions, LES uses a subgrid-scale model only for small-scale motions. LES is computationally expensive to obtain reliable statistics. The length scale of turbulence decreases with increasing Reynold number near a solid wall. Thus, to resolve near-wall regions, LES incurs very high computing costs. As a result, it is practically difficult to apply the LES technique at high Reynolds numbers. This research made use of the powerful computing infrastructure of Calcul Québec, with multiple nodes.

Table 3.3 Differences between large and small eddies (Wolfgang 2013, p.15)

Large Eddies	Small Eddies
Produced by the mean flow	Produced by large eddies
Depending on geometry and boundaries	Universal
Ordered motion	Random motion
Requiring a deterministic description	Modelled statistically
Inhomogeneous	Homogenous
Anisotropic	Isotropic
Long living and energetic	Short living and non-energetic
Diffusive	Dissipative
Carrying most of the Reynolds stress	Contributing less to the Reynolds stress
Difficult to model	Easier to model
Universal model impossible	Universal model possible

4. Results

4.1 Meshing Strategies

The model channels (Figures 3.2 to 3.6) are discretized into finite elements. An overall view of the model channels is shown in Figures 4.1(a) to 4.5(a), respectively. Configurations of the face sizing on the plane AMPD (Figure 3.2 and Figure 3.4) and the plane ABCD (Figure 3.3, Figure 3.5, and Figure 3.6) are shown from Figures 4.1(b) to 4.5(b), respectively. Meshing strategies will be discussed in more detail, as shown in Figures 4.1 to 4.5. The meshing strategies were implemented in order to achieve fine mesh in areas of interest while reducing computing costs. Information regarding the mesh size used in different techniques is summarised in Table 4.1.

4.1.1 Face Sizing and Sweep

Face sizing is applied to the inlet plane for Cases 1 to 4 [Figures 4.1(b) to 4.4(b)]. This technique is a preparation for the construction of structured mesh in relatively regular geometries. Therefore, by using the sweep technique, the control volume in the center of the model domain can be set to hexahedrons. The mesh configuration on the inlet plane of the model domain is swept consistently in the along-channel direction, generating 3D elements between the upstream and downstream open boundaries [e.g. Figure 4.2(a)]. A cell length of the hexahedron can be set to three times its own width to save even more computing power, as the streamwise change of flow characteristics is not as sensitive as that of the cross-sectional change during the simulation.

The size of mesh on the inlet boundary is set to 1×10^{-3}, 3×10^{-3}, 1.5×10^{-3}, and 3×10^{-3} m for Cases 1 to 4 [Figures 4.1(b) to 4.4(b)], respectively. These settings create mesh that is fine enough to determine the turbulent features.

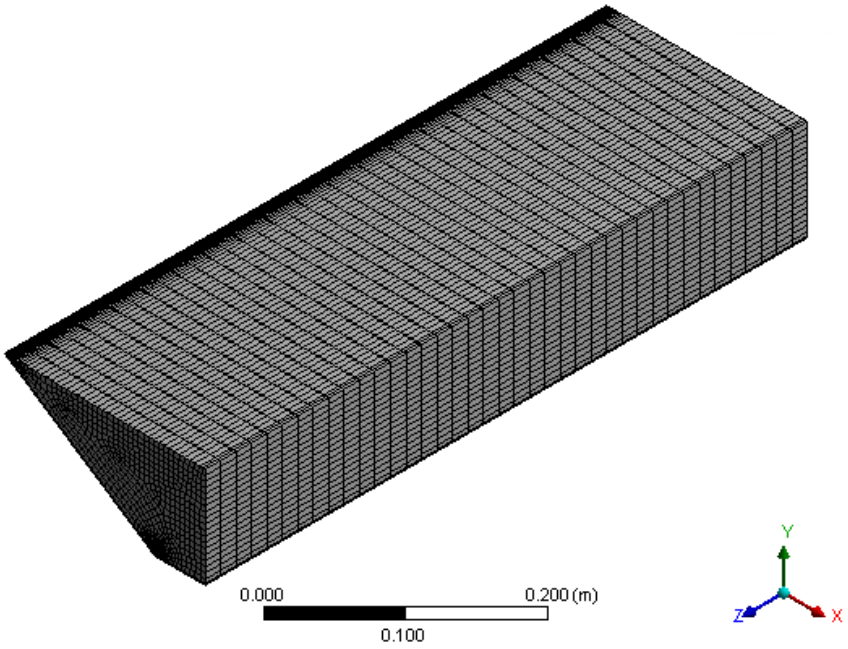

(a)

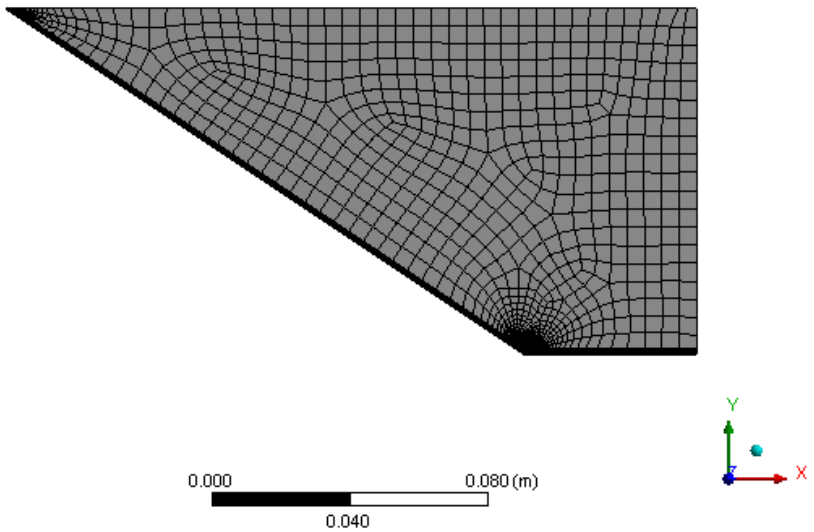

(b)

Figure 4.1 Mesh configuration of Case 1: (a) Overall view; (b) Cross-sectional view. For clarity, the mesh size for the middle portion and for regions near the boundaries shown is, respectively, 5 and 10 times larger than the actual mesh size used in LES (Table 4.1)

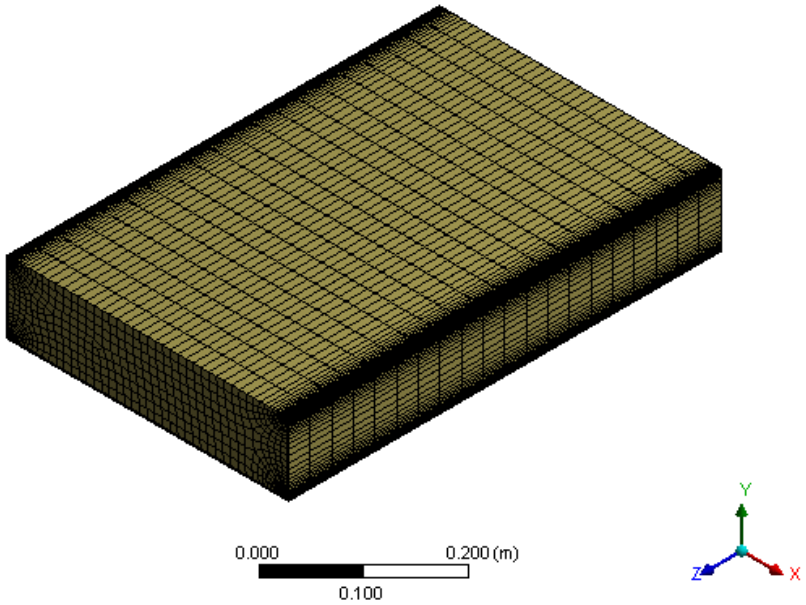

(a)

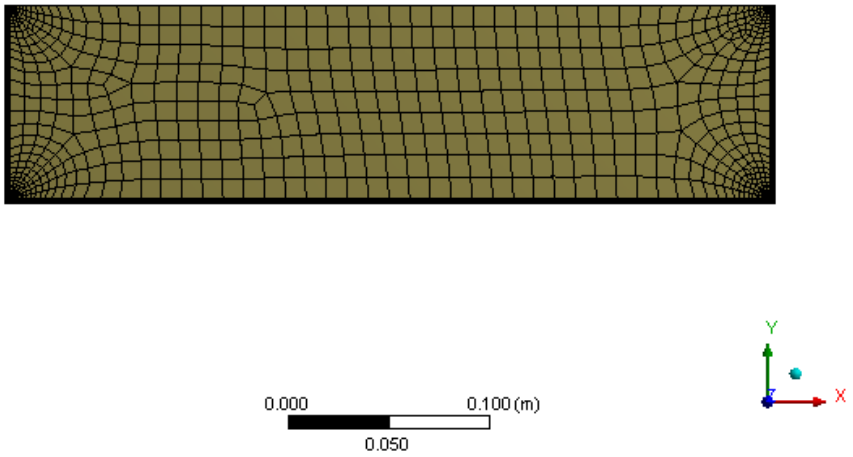

(b)

Figure 4.2 Mesh configuration of Case 2: (a) Overall view; (b) Cross-sectional view. For clarity, the mesh size for the middle portion and for regions near the boundaries shown is, respectively, 5 and 10 times larger than the actual mesh size used in LES (Table 4.1)

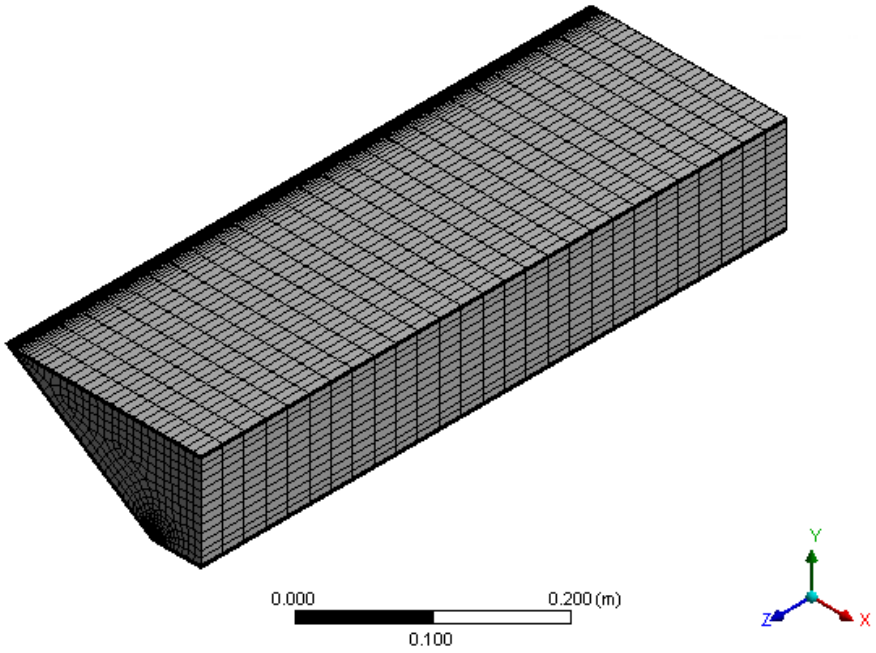

(a)

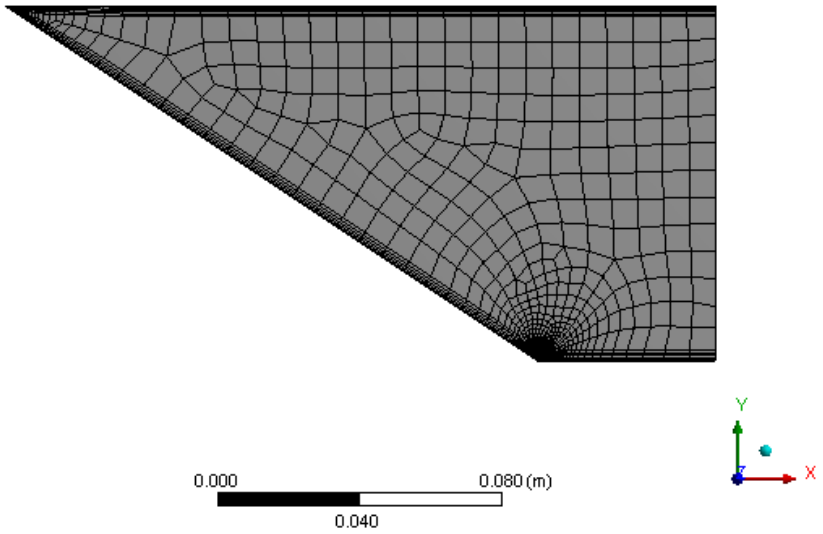

(b)

Figure 4.3 Mesh configuration of Case 3: (a) Overall view; (b) Cross-sectional view. For clarity, the mesh size for the middle portion and for regions near the boundaries shown is, respectively, 5 and 10 times larger than the actual mesh size used in LES (Table 4.1)

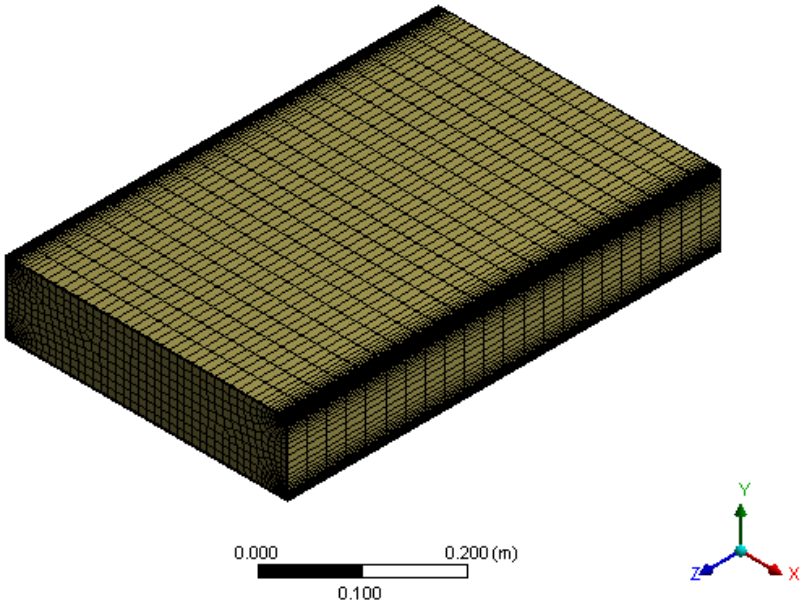

(a)

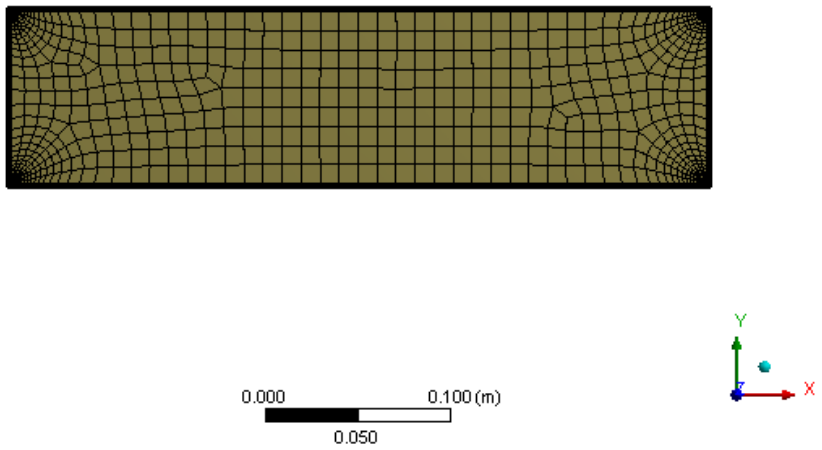

(b)

Figure 4.4 Mesh configuration of Case 4: (a) Overall view; (b) Cross-sectional view. For clarity, the mesh size for the middle portion and for regions near the boundaries shown is, respectively, 5 and 10 times larger than the actual mesh size used in LES (Table 4.1)

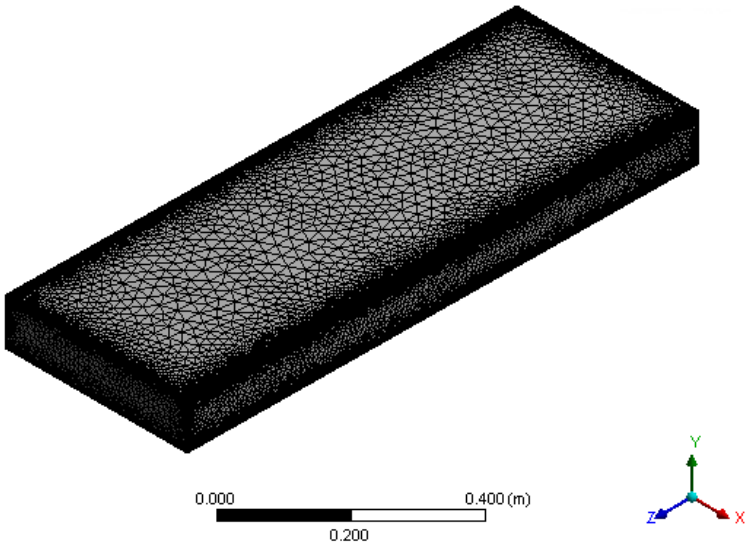

(a)

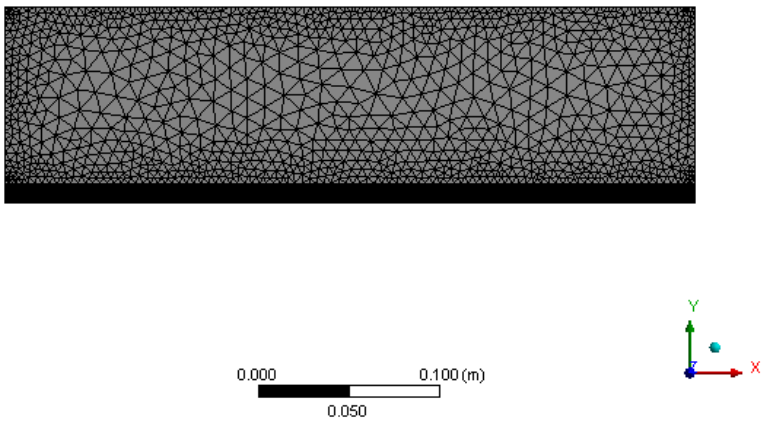

(b)

Figure 4.5 Mesh configuration of Case 5: (a) Overall view; (b) Cross-sectional view

4.1.2 Body Sizing

For an irregular geometry for Case 5 [Figure 4.5(b)], unstructured mesh is used to better fit the complicated regions around the blocks near the inlet, and body sizing is applied to the whole model domain in order to generate the mesh while controlling the mesh size. The mesh size used for flow computations should be fine enough to give good results, and model results should be independent of the configurations of mesh used. The independence of the mesh configuration is verified through comparisons of the results of runs tested under the same flow condition settings.

For Case 5, the body sizing is set to 4×10^{-3}. Although it is relatively coarse compared to other cases, this is the optimum condition for the currently available computing power.

4.1.3 Inflation

For all model channels, an inflation of five layers was applied adjacent to the channel-bed, sidewalls (Cases 1 to 5), and ice cover underside (Case 3 and Case 4). The first layer of any solid wall had a thickness of 3.14×10^{-4} m for the trapezoidal channels [Figure 4.1(a) and Figure 4.3(a)] and 3.76×10^{-5} mm for the rectangular channels [Figure 4.2(a), Figure 4.4(a), and Figure 4.5(a)]. The use of such fine mesh resolutions ensures that the dimensionless wall distance y^+ of the first node off a wall does not exceed one (1). The growth rate of the layer thickness was set to 1.1 for a smooth transition. In this research thesis, the mesh is fine enough to resolve the viscous sublayer. The following paragraphs will illustrate how to estimate the first layer's thickness.

For fluid flow of characteristic velocity U_0 over a flat surface of characteristic length L, the Reynolds number can be defined as:

[4.1] $$\mathrm{Re}_L = \frac{U_0 L}{\nu}$$

A Reynolds number based on x as well as its relationship with Re_L can be expressed as follows:

[4.2] $$\mathrm{Re}_x = \frac{U_0 x}{\nu} = 0.5\,\mathrm{Re}_L$$

In this expression, x is the distance along the plate from the leading edge.

An empirical correlation between the skin friction coefficient C_f and the Reynolds number based on distance from the leading edge Re_x is given by:

[4.3] $$C_f = 0.027\,\mathrm{Re}_x^{-\frac{1}{7}}$$

The relationship between the skin friction coefficient and wall shear stress is:

[4.4] $$C_f = \tau_0 / (\frac{1}{2})\rho U_0^2$$

With the help of Equation [2.1], the dimensionless wall distance can be estimated as:

[4.5] $$y^+ = \frac{y\nu}{U_*}$$

In Equation [4.5], we can substitute U_* from Equation [2.1], then combine Equation [4.3] and Equation [4.4] to express τ_0 using Re_x. We can then replace Re_x by Re_L and substitute the expression for τ_0 into Equation [4.5]. Finally, the first layer wall distance can be estimated as:

[4.6] $$y = y^+ \times L \times \mathrm{Re}_L^{-13/14}$$

4.1.4 Body of Influence

The Body of Influence technique is applied to the corner regions in order to refine the mesh configuration in all five cases.

For Case 1, Case 3, and Case 5, only one arc is specified at each corner region [Figures 4.1(b), 4.3(b) and 4.5(b)]. The radii of these arcs are 0.5, 0.5, and 0.2 cm, respectively. The mesh sizes refined within the arcs are 3.14×10^{-4}, 3.14×10^{-4}, and 2×10^{-3} m, respectively.

Four arcs of different radius are specified at each corner for Case 2 and Case 4 [Figures 4.2(b) and 4.4(b)]. The radius of the four arcs are, respectively, 0.2, 0.5, 0.9, and 1.4 cm. The radius gradually increases in 0.2, 0.3, 0.4, and 0.5 cm increments. The mesh sizes refined within the sub-regions are, respectively, 7.52×10^{-5}, 1.32×10^{-4}, 1.9×10^{-4}, and 2.74×10^{-4} m.

The mesh size at the corners is smaller than in the center, and, if possible, it will be set to the first inflation layer mesh size. However, it is hard to achieve this for Case 5 with the currently available computing power. After drawing the arcs in various sketches, they are extruded to be frozen bodies

[Figures 4.1(a) to 4.5(a)], which will help refine the corner regions without added influence on the boundary conditions.

The size and quantity of the arcs at each corner and the mesh size between arcs in each case are summarised in Table 4.1. In addition, the parameters for face sizing at the inlet for Cases 1 to 4, the body sizing in the center of Case 5, and the first layer thickness in each case are included. The value of cell length is null for Case 5 because the sweep technique cannot be applied. The face size for Case 5 is the body size for the middle portion of the model domain.

The total nodes and elements in different cases are summarised in Table 4.2. Note that structured mesh is used in the first four cases, and unstructured mesh is used for Case 5. Time step varies from case to case, even for similar geometries, because the cell length is different. The total number of time step in each case is high enough to simulate three flow-through times for the first four cases and ten flow-through times for Case 5. The maximum number of iterations is set to 120, in order to achieve high accuracy of calculations. Computing time varies for each case, depending on the number of tasks in the queue and the processors requested. The results that are presented in Section 4.2 and Section 4.3 are for the last time step of the simulation in question. The results that are presented in Section 4.4 and Section 4.5 include three different model times.

Table 4.1 Parameters used in mesh generation

Case number	Number of arcs	Radius of arcs (cm)	Mesh size between arcs (m)	First layer thickness (m)	Face sizing (m)	Cell length (m)
Case 1	1	0.5	3.14×10^{-4}	3.14×10^{-4}	1×10^{-3}	3×10^{-3}
Case 2	4	0.2, 0.5, 0.9, 1.4	7.52×10^{-5}, 1.32×10^{-4}, 1.9×10^{-4}, 2.74×10^{-4}	3.76×10^{-5}	3×10^{-3}	6×10^{-3}
Case 3	1	0.5	3.14×10^{-4}	3.14×10^{-4}	1.5×10^{-3}	4.5×10^{-3}
Case 4	4	0.2, 0.5, 0.9, 1.4	7.52×10^{-5}, 1.32×10^{-4}, 1.9×10^{-4}, 2.74×10^{-4}	3.76×10^{-5}	3×10^{-3}	9×10^{-3}
Case 5	1	0.2	2×10^{-3}	3.76×10^{-5}	4×10^{-3} (body sizing)	null

Table 4.2 A summary of total nodes, elements, and other model parameters used in five cases

Parameter	Case 1	Case 2	Case 3	Case 4	Case 5
Total nodes	3351876	1790316	1129005	1352736	1128209
Elements	3362000	1717744	1232934	1296100	5729313
Mesh type	Structured, Hexahedron				Unstructured, Tetrahedron
Time step size (s)	0.02	0.003	0.02	0.01	0.008
Criterion for convergence	10^{-6}				
Number of time steps	1800	1500	2100	360	2720
Model time period (s)	36	4.5	42	3.6	21.76
Max iterations per time step	120				
Simulation time (hr)	47	8	29	4	91

4.2 Velocity Profiles

The Cartesian coordinates system is used, with the z-axis pointing positively in the streamwise direction (along the channel-bed) against the main flow, the y-axis pointing positively upward in the vertical direction (perpendicular to the bed), and the x-axis in the lateral direction (Figures 3.2 to 3.6). The streamwise velocity profiles of Cases 1 to 5 are shown in Figures 4.6 to 4.10, respectively. In the first four cases, the velocity profiles are plotted for the central line at the middle of the cross section at a distance of 75% of the total channel length or $z = -0.450$, -0.439, -0.450, and -0.439 m, respectively. These distances are measured from the inlet plane (Figures 3.2 to 3.5). For Case 5, the velocity profile is plotted for the vertical line at the middle of the cross section at $z = -0.813$ m from the inlet plane (Figure 3.6).

4.2.1 Trapezoidal (Case 1) and Rectangular (Case 2) Open Channels

As shown in Figure 4.6 (Case 1) and Figure 4.7 (Case 2), the streamwise velocity profiles are similar to a typical velocity profile of flow over a flat plate.

The velocity profiles show gradual changes between the free surface and a depth about 85% of the total flow depth below the surface. The 85% depth is seen as a transition point. Further below, the

profiles show a large drop in velocity magnitude. The velocity profiles have large spatial gradients below the 85% depth, and relatively small spatial gradients above. In other words, the upper profiles show smoother transitions. At the transition point, the velocity has a magnitude of slightly lower than the bulk mean velocity (equal to 0.05 and 0.495 m/s for Case 1 and Case 2, respectively) of the channel flow.

The maximum velocity has values of 5.76×10^{-2} and 5.78×10^{-1} m/s, for Case 1 and Case 2 (Table 4.3), respectively. The maximum velocity occurs near the free surface.

The velocity changes only gradually over the depth range of 70 to 90% of the total flow depth in the trapezoidal open channel (Case 1, Figure 4.6).

4.2.2 Trapezoidal (Case 3) and Rectangular (Case 4) Ice-Covered Channels

In ice-covered cases (Table 4.2, Case 3 and Case 4), the vertical distributions of streamwise velocities are characterised by a parabolic shape (Figure 4.8 and Figure 4.9). This is the same pattern as the two-power law reported in the literature (Dolgopolova, 1998). The velocity profile in an ice-covered channel can be considered two velocity profiles: one associated with the ice cover, and the other associated with the channel-bed. The two profiles meet at a certain point in the water column, where the shear stress is zero (or where the velocity reaches the maximum value).

For both Case 3 and Case 4 (Table 4.2), the velocity profiles show a core of relatively strong flow between the 15 and 85% flow depths. The flow velocities drop quickly above the core because of the ice underside influence and below because of the bed influence. Within the core of high velocities, there are only gradual changes in flow velocity, in comparison to the regions outside. In other words, the velocity profiles have large spatial gradients in the vicinity of the upper and lower boundaries. The spatial gradients in the middle depth are small.

The maximum velocity has a value of 6.39×10^{-2} m/s for Case 3, and 5.82×10^{-1} m/s for Case 4 (Table 4.3). The maximum velocity occurs at a depth of about 40% the total flow depth above the channel-bed for both cases. The presence of ice (Case 3 and Case 4) has increased the maximum

velocity in the water column, as clearly shown by a comparison to the corresponding maximum velocity for Case 1 and Case 2.

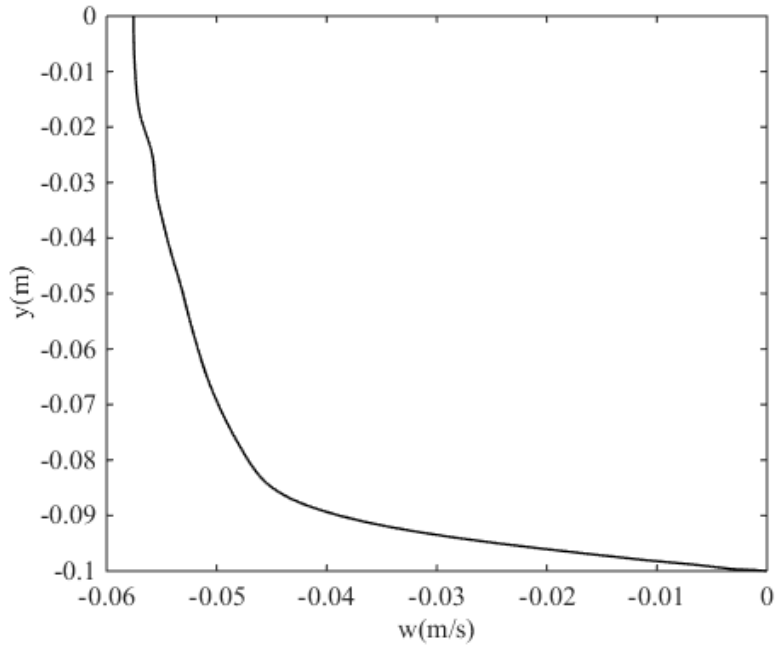

Figure 4.6 Streamwise velocity profile at a selected vertical line for Case 1

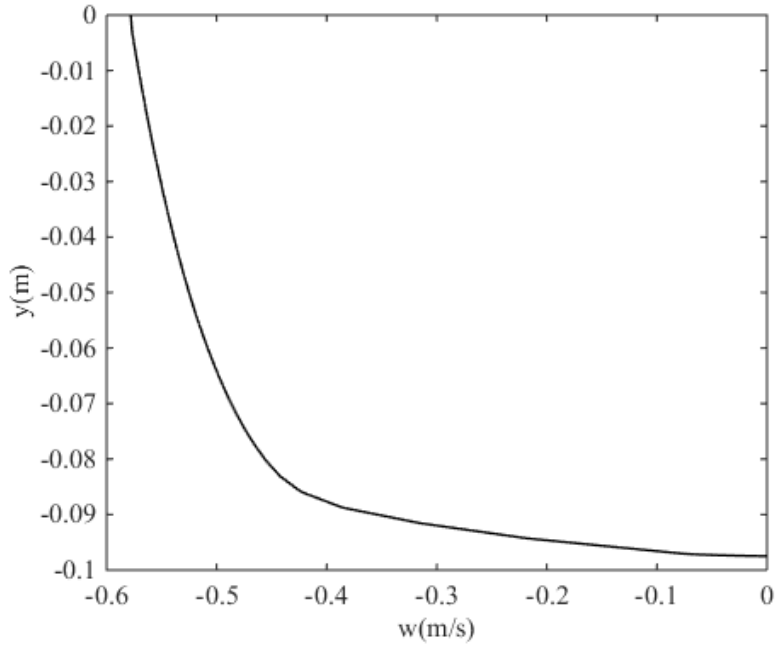

Figure 4.7 Streamwise velocity profile at a selected vertical line for Case 2

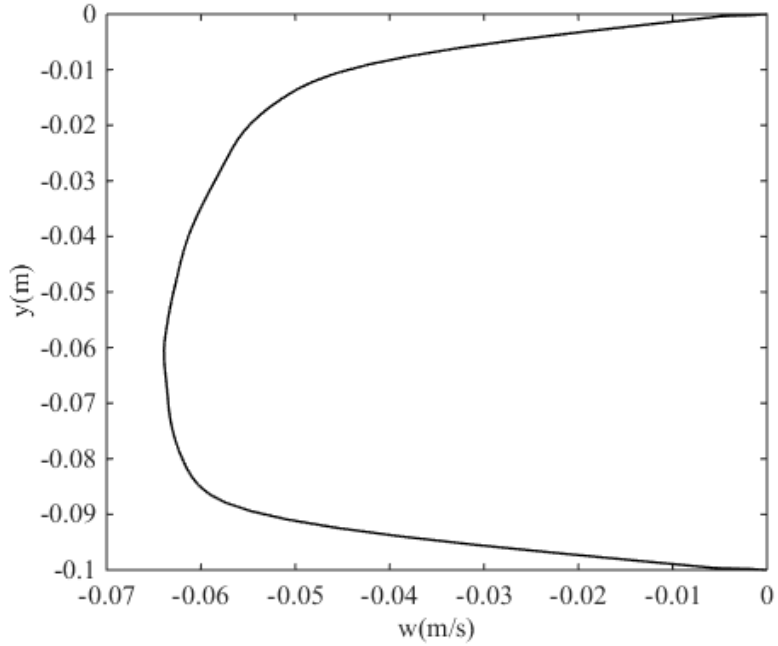

Figure 4.8 Streamwise velocity profile at a selected vertical line for Case 3

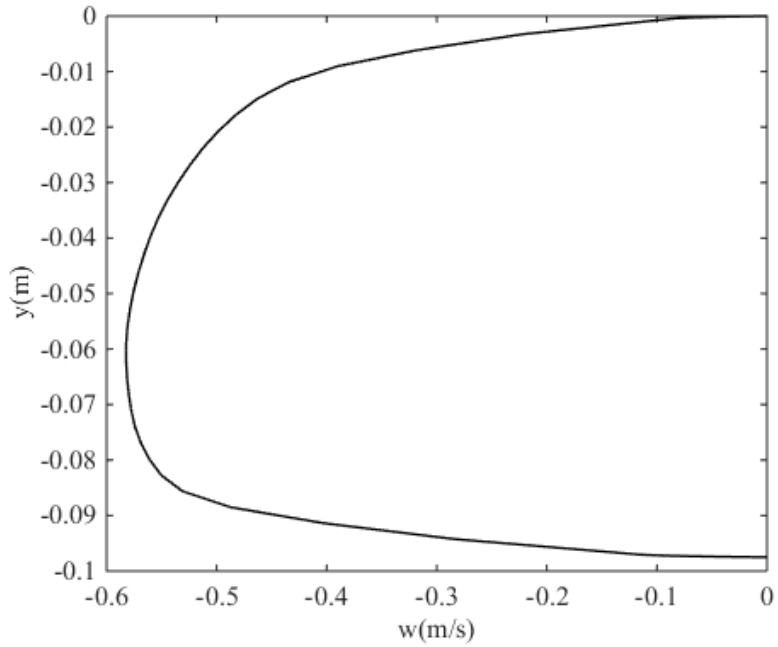

Figure 4.9 Streamwise velocity profile at a selected vertical line for Case 4

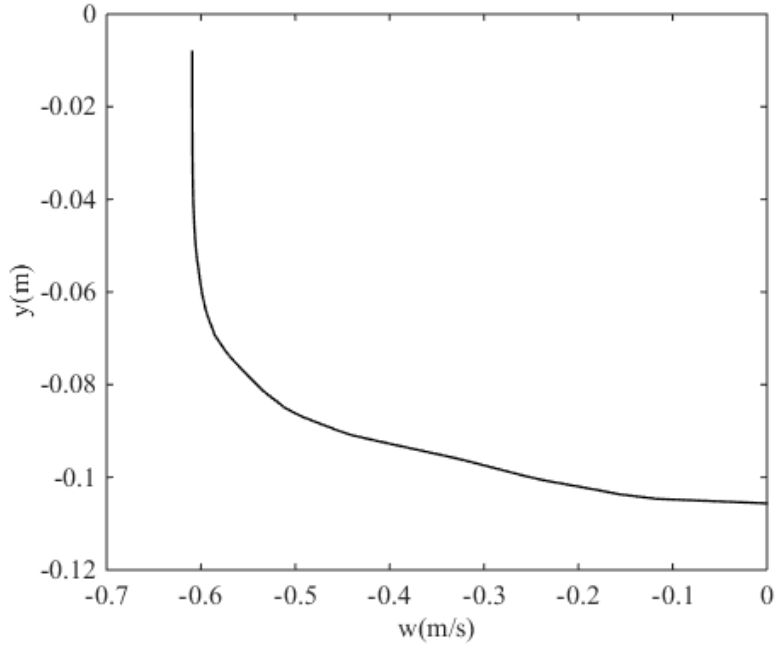

Figure 4.10 Streamwise velocity profile at a selected vertical line for Case 5

4.2.3 Rectangular (Case 5) Open Channel with Blocks at the Channel-bed

The velocity profile for Case 5 is shown in Figure 4.10. Case 5 (Figure 3.6) has the same cross-sectional geometry as Case 2 (Figure 3.3), but with nine blocks being added to the channel-bed within one flow-depth from the inlet plane. The channel length was extended to 11 times the total flow depth. The channel-bed has a small longitudinal (1 horizontal to 0.03 vertical). At the longitudinal location of about $z = -0.813$ m (Figure 3.6), the free surface is located at $y = -8.13\times10^{-3}$ and the channel-bed at $y = -1.06\times10^{-1}$ m.

For Case 5 (Figure 4.10), the transition point (as discussed in Section 4.2.1) is located at approximately 40% the total flow depth above the channel-bed. Between the free surface and the transition point, the velocity profile shows insignificantly small spatial gradients.

The maximum velocity has a value of 6.09×10^{-1} m/s (Table 4.3). In fact, this value is applicable to about 70% the total flow depth below the free surface. The maximum velocity is much higher for Case 5 than for Case 2 (without blocks, Figure 4.7).

The maximum and mean velocities for the five cases are listed in Table 4.3, along with the maximum and mean boundary shear stresses. To determine the bulk mean velocity of the channel flow, we divide the flowrate by the cross-sectional area.

Table 4.3 The maximum and mean boundary shear stresses and velocities for the five cases

Case Number	Maximum bed shear stress (Pa)	Mean bed shear stress (Pa)	Maximum sidewall shear stress (Pa)	Mean bed sidewall stress (Pa)	Maximum velocity (m/s)	Mean velocity (m/s)
Case 1	5.96×10^{-3}	5.66×10^{-3}	8.86×10^{-3}	7.45×10^{-3}	5.76×10^{-2}	5.00×10^{-2}
Case 2	3.51×10^{-1}	3.16×10^{-1}	6.44×10^{-1}	4.35×10^{-1}	5.78×10^{-1}	4.95×10^{-1}
Case 3	9.71×10^{-3}	9.17×10^{-3}	1.14×10^{-2}	8.99×10^{-3}	6.39×10^{-2}	5.00×10^{-2}
Case 4	5.78×10^{-1}	5.24×10^{-1}	8.23×10^{-1}	5.27×10^{-1}	5.82×10^{-1}	4.95×10^{-1}
Case 5	2.71×10^{-1}	1.49×10^{-1}	2.61×10^{-1}	1.57×10^{-1}	6.09×10^{-1}	4.95×10^{-1}

4.3 Velocity Contours

Contours of the predicted streamwise velocity, w, are shown in Figures 4.11 to 4.15 for the five cases. The corresponding longitudinal positions are $z = -0.450$, -0.439, -0.450, -0.439, and -0.813 m (Figures 3.2 to 3.6). The contour values in Figures 4.11 to 4.15 are negative because the z-axis points positively in the direction opposite to the main flow direction. The contour plots show 100 contour levels.

4.3.1 Trapezoidal (Case 1) and Rectangular (Case 2) Open Channels

The velocity contours for Case 1 (Figure 4.11) and Case 2 (Figure 4.12) exhibit a number of common features. First, the maximum velocity occurs slightly below the free surface, and the flow velocities drop to almost zero at the channel-bed and on the sidewalls. These predictions are realistic. Second, in the central part of the trapezoidal and rectangular open channel sections, there is a core of relatively high velocities near the free surface; the velocity magnitude gradually decreases as an increasing distance from the core centre. Third, due to the frictional effects of the channel-bed and sidewalls, the flow velocities drop quickly toward the solid boundaries.

For both channel sections (Figure 4.11 and Figure 4.12), the contours of flow velocity reflect boundary layer dynamics, with typical velocity profiles (Figure 4.6 and Figure 4.7), in spite of spatial fluctuations in velocities in the corner regions and just below the free surface. These fluctuations are probably a result of local turbulence effects. For example, there are crowded velocity contours in some small areas in the vicinity of the free surface (Figure 4.12, for Case 2).

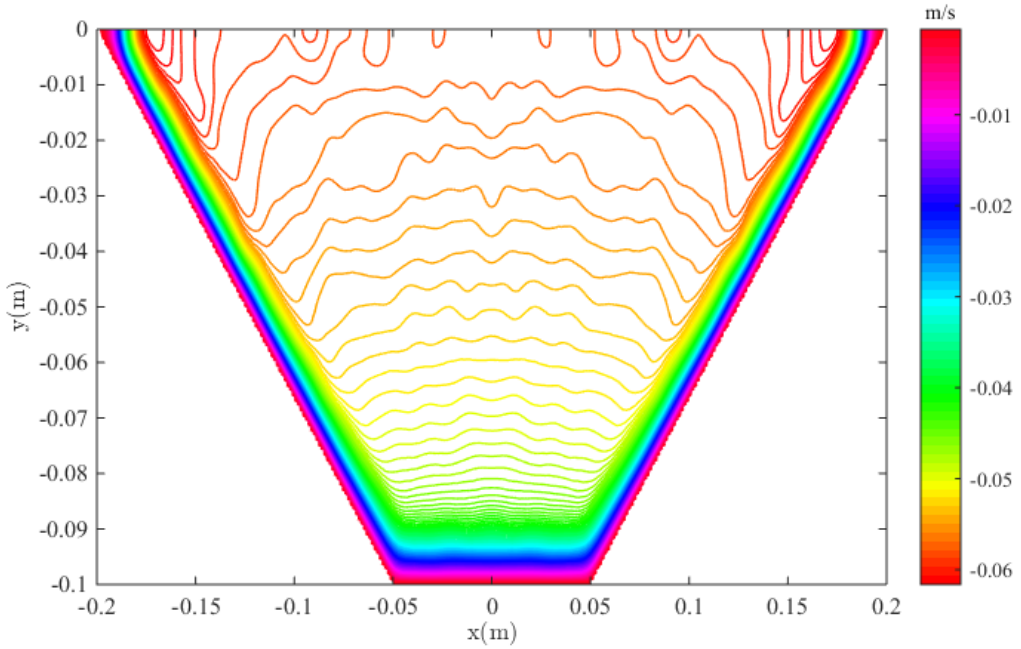

Figure 4.11 Contours of streamwise velocity, *w*, at a selected cross section for Case 1

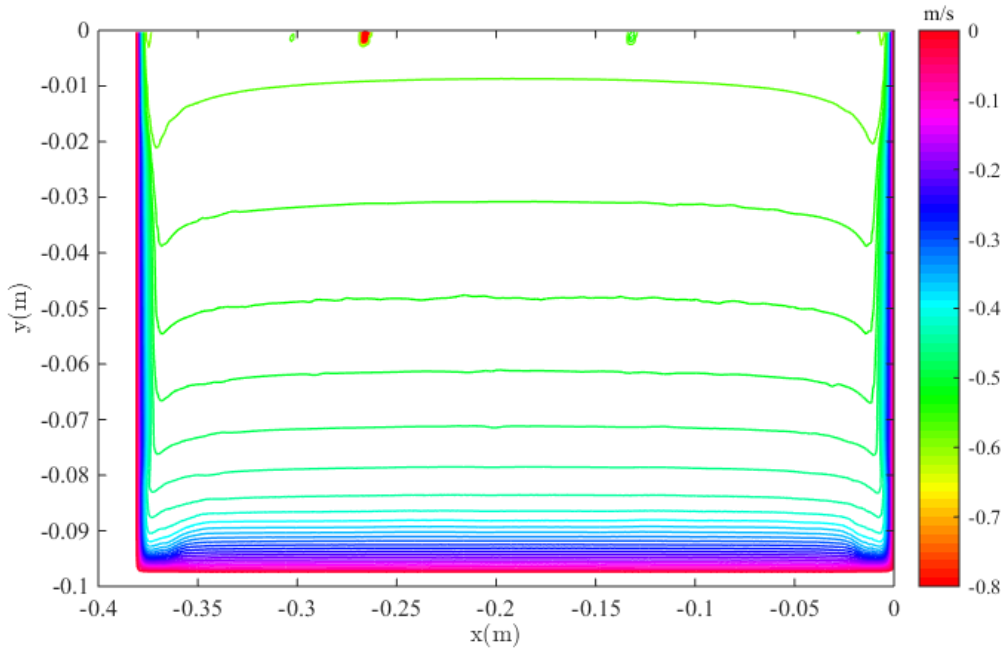

Figure 4.12 Contours of streamwise velocity, *w*, at a selected cross section for Case 2

4.3.2 Trapezoidal (Case 3) and Rectangular (Case 4) Ice-Covered Channels

These two cases differ from Case 1 (Figure 4.11) and Case 2 (Figure 4.12), in which an ice cover is added to the water channels. The ice underside is treated as a no-slip boundary (Figure 4.13 and Figure 4.14). Contours of the water velocity for Case 3 (Figure 4.13) and Case 4 (Figure 4.14) exhibit some features similar to Case 1 (Figure 4.11) and Case 2 (Figure 4.12). For example, there is a significant difference in velocity magnitude between the flow in the central region of the cross section and the flow in the boundary layer. The densely distributed contours near the channel boundaries correspond to a sharp decrease in velocity magnitude.

The maximum velocity occurs at approximately 40% the total flow depth above the channel-bed for both Case 3 (Figure 4.13) and Case 4 (Figure 4.14). This is different from the results for Case 1 (Figure 4.11) and Case 2 (Figure 4.12), where the maximum velocity occurs at the free surface. There is a core of relatively high velocities surrounding the maximum velocity in the central region of the channel cross section (away from the solid boundaries). The velocity contour values decrease slowly in this region. Small fluctuations of velocity contours occur near the boundaries.

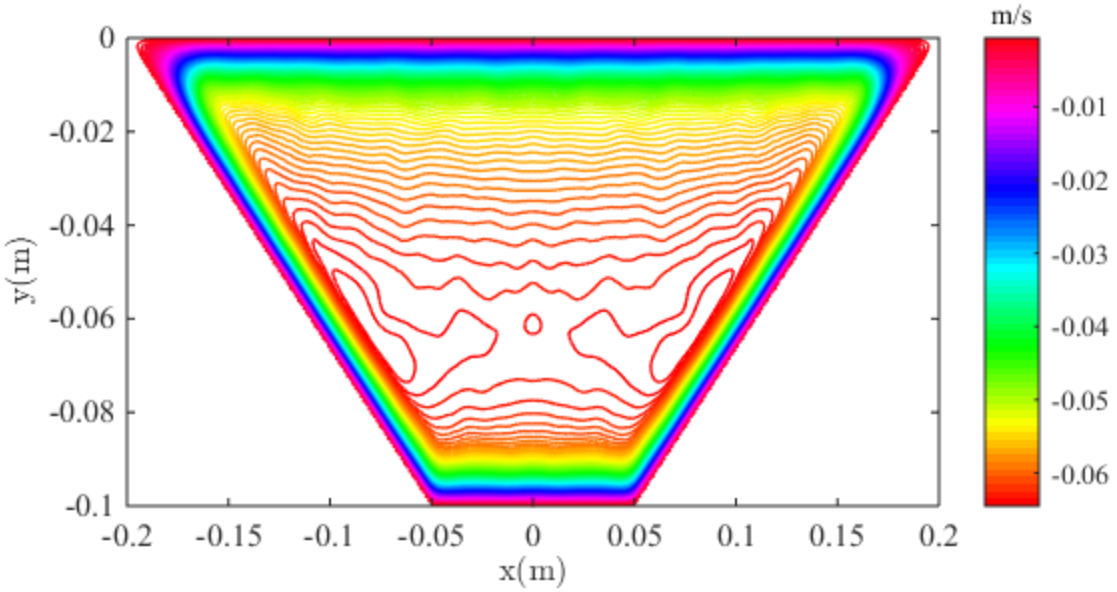

Figure 4.13 Contours of streamwise velocity, *w*, at a selected cross section for Case 3

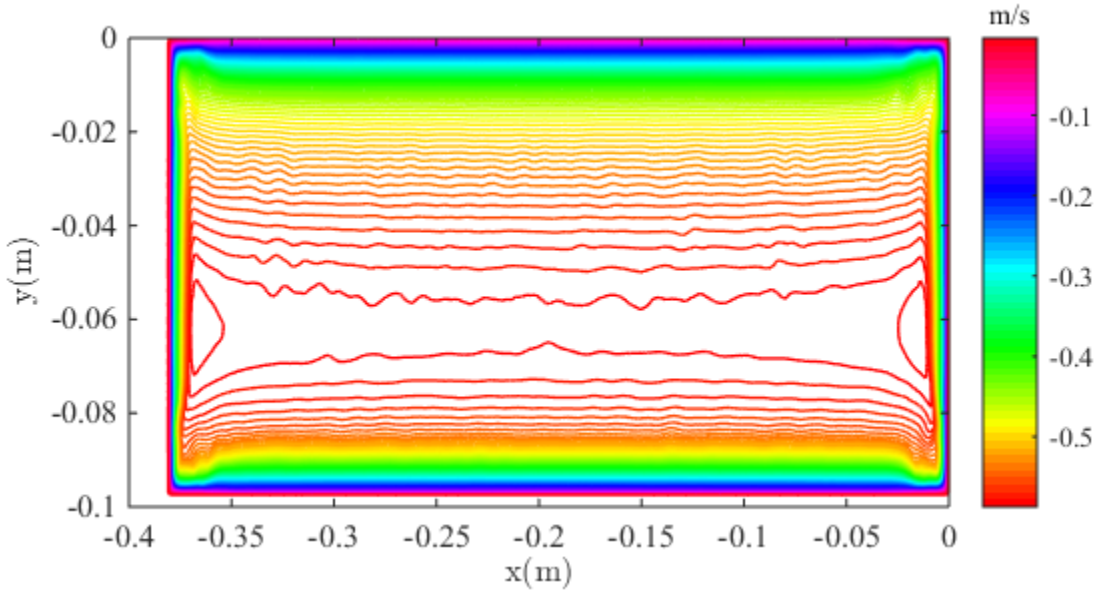

Figure 4.14 Contours of streamwise velocity, *w*, at a selected cross section for Case 4

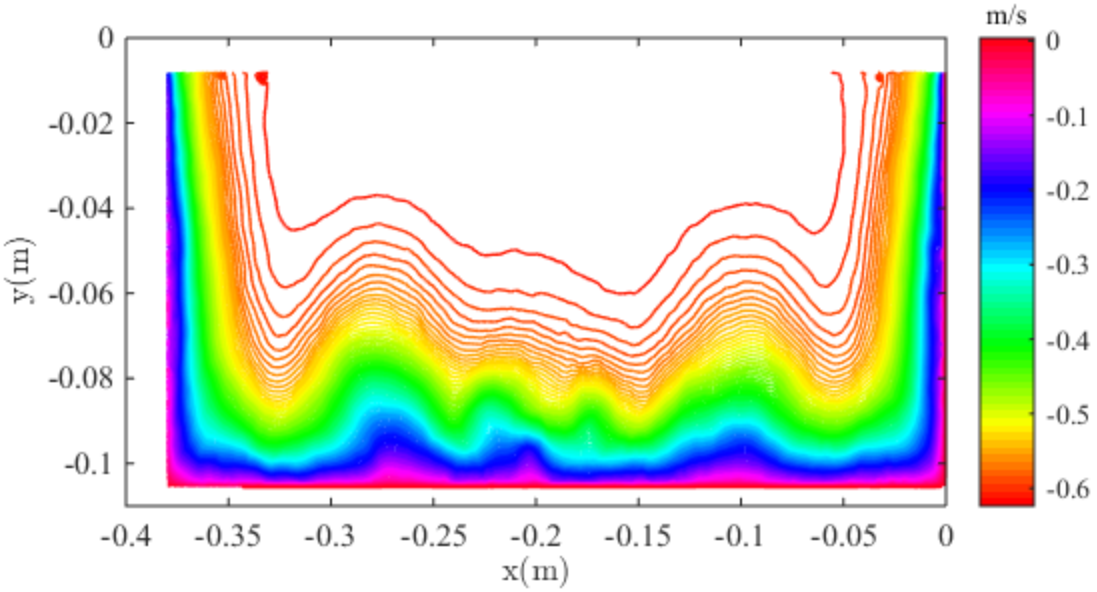

Figure 4.15 Contours of streamwise velocity, *w*, at a selected cross section for Case 5

4.3.3 Rectangular (Case 5) Open Channel with Blocks at the Channel-bed

Distributions of the velocity contours for Case 5 (Figure 4.15) are different from those for Case 2 (Figure 4.12). The differences are due to the presence of blocks being added to the channel-bed near the inlet plane. These blocks make velocity contours less regular, compared to the velocity contours for Case 2 (Figure 4.12). The irregular contours contain wavy patterns.

In the centre of the channel cross section, within the core of high velocities, the velocities change little in magnitude. The high velocity core occurs immediately below the free surface. The velocity contour values decrease gradually from the irregular fringe of the high velocity core, and drop quickly to a low value toward the solid boundaries. The area of densely distributed contours near the boundaries for Case 5 (Figure 4.15) is larger than Case 2 (Figure 4.12).

The lower boundary of the high velocity core shows wavy patterns across the channel width for Case 5 (Figure 4.15). The wavy fluctuations show a vertical displacement as large as 20% flow depth. Clearly, the blocks (Figure 3.6) result in asymmetric patterns of velocity contour.

4.4 Distributions of Bed Shear Stress

The wall shear stress is obtained from the linear stress-strain relationship given in Equation [2.11]. Combining the equation with the relationship between the shear velocity and boundary shear stress (Equation [2.1]) gives the bed shear stress, τ_w, (Equation [3.20]), which is similar to the definition of viscous shear. The cross-channel distributions of τ_w are plotted in Figures 4.16(a)-(c) to 4.20(a)-(c) for Cases 1 to 5, respectively. The corresponding longitudinal positions of the plots are z = −0.450, −0.439, −0.450, −0.439, and −0.813 m (Figures 3.2 to 3.6). Panels (a), (b) and (c) of the individual figures correspond to three different model times. In each of the plots, the local bed shear stresses have been normalised by the mean bed shear stress $\bar{\tau}_{cb}$. The horizontal axis shows the normalised distance (across the channel-bed from the left corner) by the channel-bed width. Table 4.3 summarises the mean and maximum bed shear stresses. For Cases 1 to 5, the channel-bed width (Figures 3.2 to 3.6) is equal to 10.0, 38.1, 10.0, 38.1, and 38.1 cm, respectively.

4.4.1 Trapezoidal (Case 1) and Rectangular (Case 2) Open Channels

Note that the boundary shear stress refers to the tractive force exerted by the flowing water on the boundary in question. From this study, values of local bed shear stress, τ_w, are relatively high within the largest central portion of the channel-bed and drop rapidly to zero toward the corners. This is in consistence with the results reported in Chow (1959, p. 169). Chow's (1959) results are partly based experimental data and membrane analogy analysis. It can be argued that the shear stresses at the corners must be equal to zero. Non-zero shear stresses at the corners will lead to the unphysical condition that the local shear forces approach infinity.

For Case 1, Figure 4.16(a)-(c) show the distributions of bed shear stress at model times of t = 32, 34, and 36 s, respectively. Between panels (a), (b), and (c) of Figure 4.16, at the dimensionless distance (normalised by the channel bed-width) of 0.21, there are differences in shear stress as large as 0.019 $\bar{\tau}_{cb}$. For Case 2, the model times are 4.2 [Figure 4.17(a)], 4.35 [Figure 4.17(b)], and 4.5 s [Figure 4.17(c)]. Between panels (a), (b), and (c) of Figure 4.17, the differences in shear stress are small. The maximum difference is 0.0026 $\bar{\tau}_{cb}$ at the normalised distance of 0.007. More discussions of panels (c) of the figures are given below.

The normalised bed shear stresses in the corner regions have different distributions between the trapezoidal channel section [Case 1, Figure 4.16(c)] and the rectangular channel section [Case 2, Figure 4.17(c)].

For Case 2 [Figure 4.17(c)], the predicted bed shear stresses across the channel-bed width are in reasonable agreement with the experimental data of Knight et al. (1984). The distributions of bed shear stress have two inflection points. From these points toward the corners, the bed shear stresses decrease dramatically [Figure 4.17(c)]. The inflection points are symmetrical about the central line of the channel. They are located at a horizontal distance of 5% the bed width from each sidewall corner. At the inflection points, the bed shear stresses have a value of around 60% the mean bed shear stress. According to Tominaga & Nezu (1991), secondary flow plays an important role in generating inflection points. For Case 1 (trapezoidal channel), no inflection point occurs [Figure 4.16(c)].

For both Case 1 and Case 2 [Figure 4.16(c) and 4.17(c)], the distributions of bed shear stresses show small local peaks before their dramatic drop to lowest values toward the corners. These local peaks are located at a horizontal distance of approximately 20% [Case 1, Figure 4.16(c)] and 10% [Case 2, Figure 4.17(c)] the total channel width from the sidewall corners.

(a)

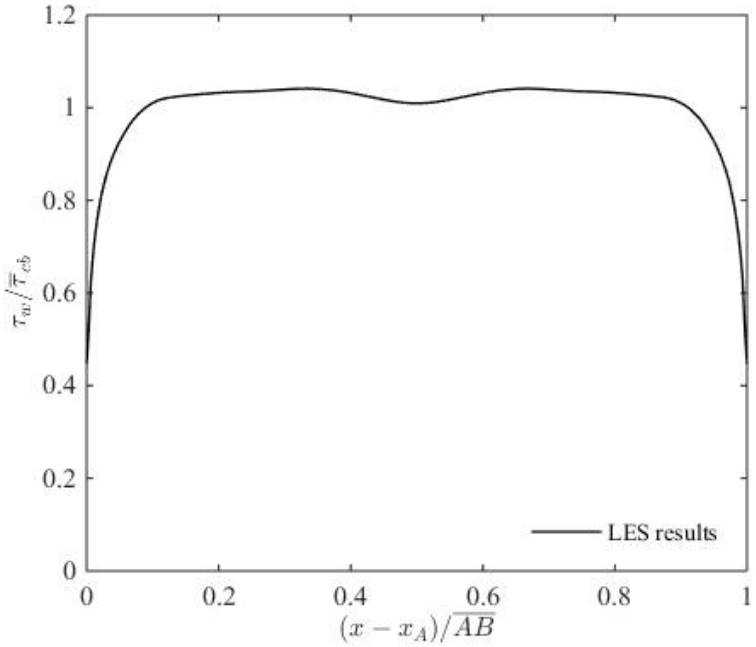
1.2
1
0.8
0.6
0.4
0.2
0
$\tau_w/\overline{\tau}_{eb}$
LES results
0
0.2
0.4
0.6
0.8
1
$(x - x_A)/\overline{AB}$

(b)

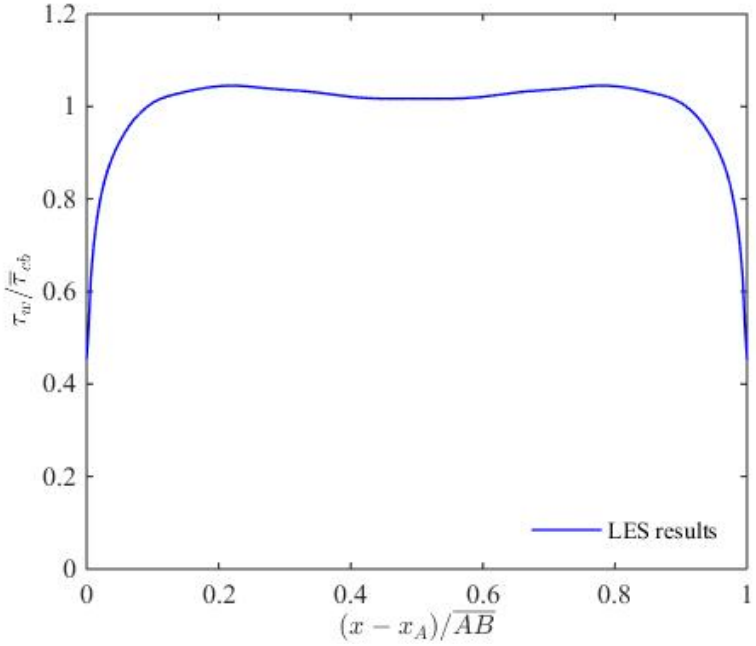
1.2
1
0.8
0.6
0.4
0.2
0
$\tau_w/\overline{\tau}_{eb}$
LES results
0
0.2
0.4
0.6
0.8
1
$(x - x_A)/\overline{AB}$

(c)

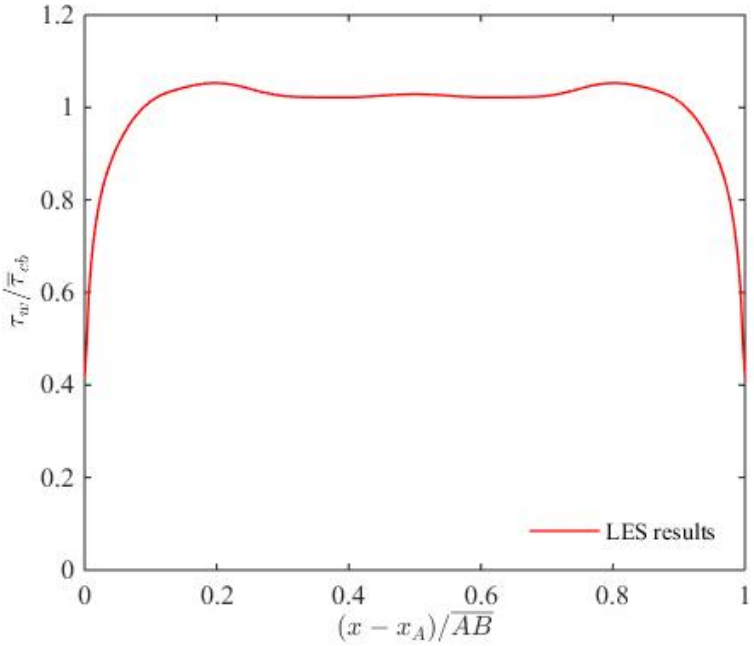

Figure 4.16 Distribution of predicted bed shear stress for Case 1, where x is the dimensionless cross-channel coordinate relative to the corner marked as A (Figure 3.2), and $\overline{AB}$ is the channel-bed width (Figure 3.2). Model times are t = 32 [panel (a)], 34 [panel (b)], and 36 s [panel (c)]

(a)

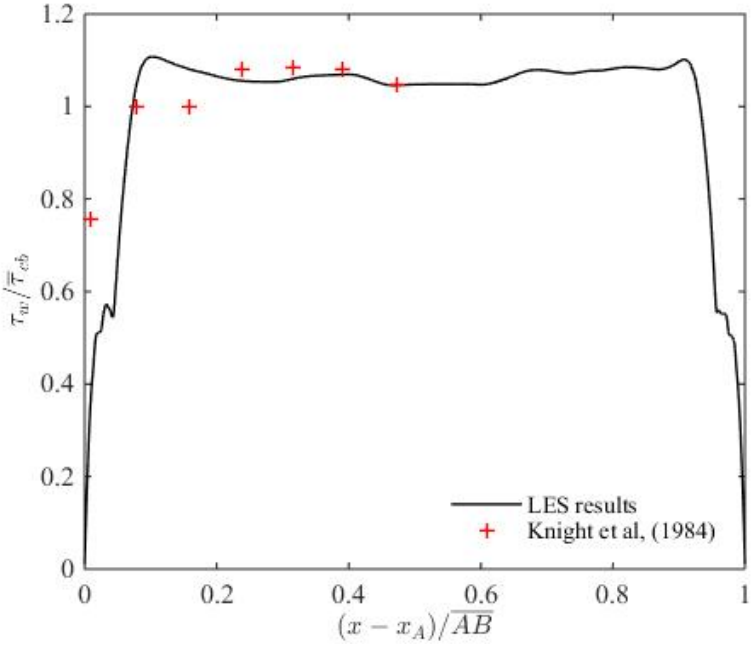

(b)

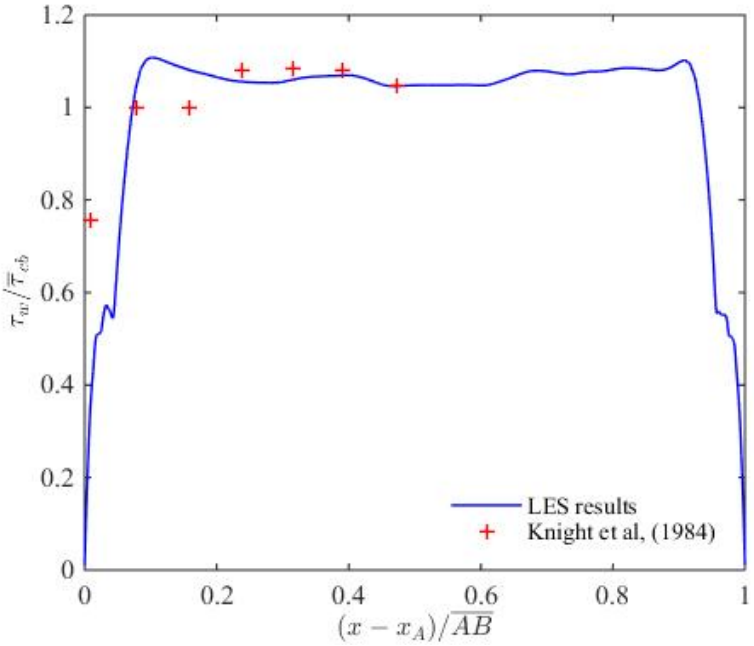

(c)

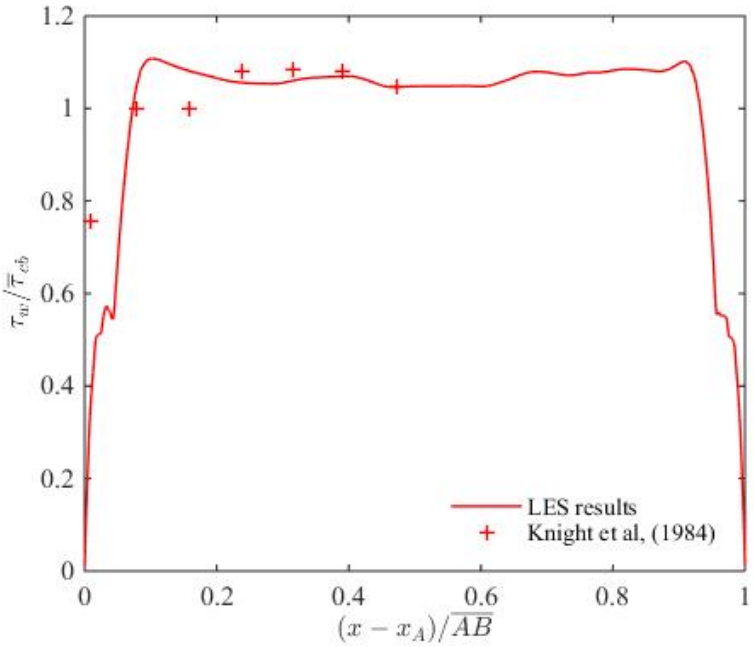

Figure 4.17 Distribution of predicted bed shear stress for Case 2, where x is the dimensionless cross-channel coordinate relative to the corner marked as A (Figure 3.3), and $\overline{AB}$ is the channel-bed width (Figure 3.3). Knight et al.'s (1984) measurements are shown as the symbols '+' for comparison. Model times are t = 4.2 [panel (a)], 4.35 [panel (b)], and 4.5 s [panel (c)]

4.4.2 Trapezoidal (Case 3) and Rectangular (Case 4) Ice-Covered Channels

For Case 3, Figure 4.18(a)-(c) show the distributions of bed shear stress at model times of t = 38, 40, and 42 s, respectively. Between panels (a), (b), and (c) of Figure 4.18, at the dimensionless distance (normalised by the channel bed-width) of 0.65, there are differences in shear stress as large as 0.014 $\bar{\tau}_{cb}$. For Case 4, the model times are 2.8 [Figure 4.19(a)], 3.0 [Figure 4.19(b)], and 3.2 s [Figure 4.19(c)]. Between panels (a), (b), and (c) of Figure 4.19, at the normalised distance of 0.94, there are differences in shear stress as large as 0.04 $\bar{\tau}_{cb}$. More discussions of panels (c) of the figures are given below.

Under ice-covered condition [Case 3, Figure 4.18(c); Case 4, Figure 4.19(c)], the distributions of bed shear stresses have some similar features as open water condition [Case 1, Figure 4.16(c); Case 2, Figure 4.17(c)]. The local bed shear stresses have relatively high values within the largest central portion of the channel-bed. They decrease dramatically toward the lower corners of the channel section. In the corner regions, the normalised bed shear stresses have different distributions between the trapezoidal channel [Case 3, Figure 4.18(c)] and the rectangular channel section [Case 4, Figure 4.19(c)].

The inflection points for Case 4 [Figure 4.19(c)] have lower values of bed shear stress than for Case 2 [Figure 4.17(c)]. No inflection point occurs in the trapezoidal channel section [Case 3, Figure 4.18(c)].

For Case 4, the distributions of bed shear stress [Figure 4.19(c)] show small local peaks before the dramatic drop. These peaks occur at the same locations for Case 2 [Figure 4.17(c)]. For Case 3, the distribution of bed shear stress [Figure 4.18(c)] has strong spatial fluctuations, making it difficult to identify any peaks.

The presence of ice cover (Case 3 and Case 4) is seen to intensify the mean and maximum bed shear stresses (Table 4.3) by a factor of approximately 1.65, in comparison to those under open water condition (Case 1 and Case 2).

(a)

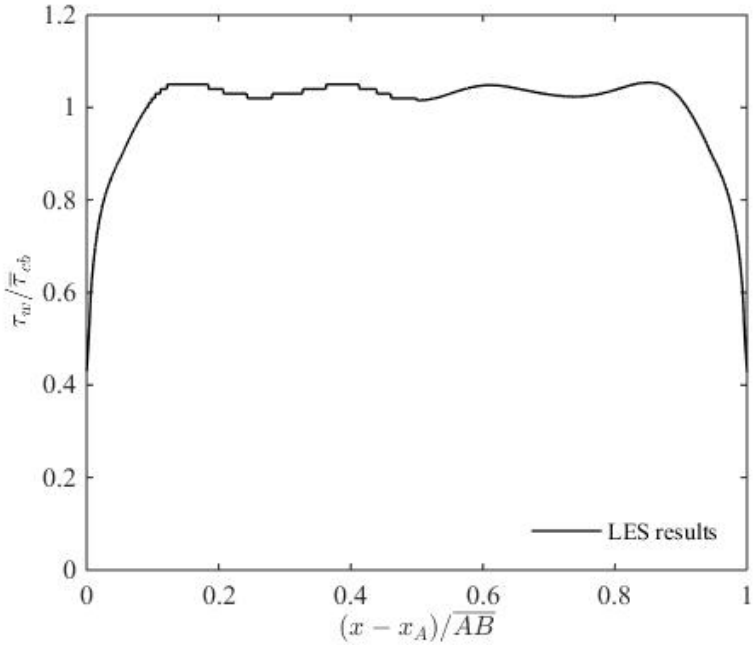
1.2
1
0.8
0.6
0.4
0.2
0
0
0.2
0.4
0.6
0.8
1
$\tau_w/\overline{\tau}_{cb}$
$(x - x_A)/\overline{AB}$
LES results

(b)

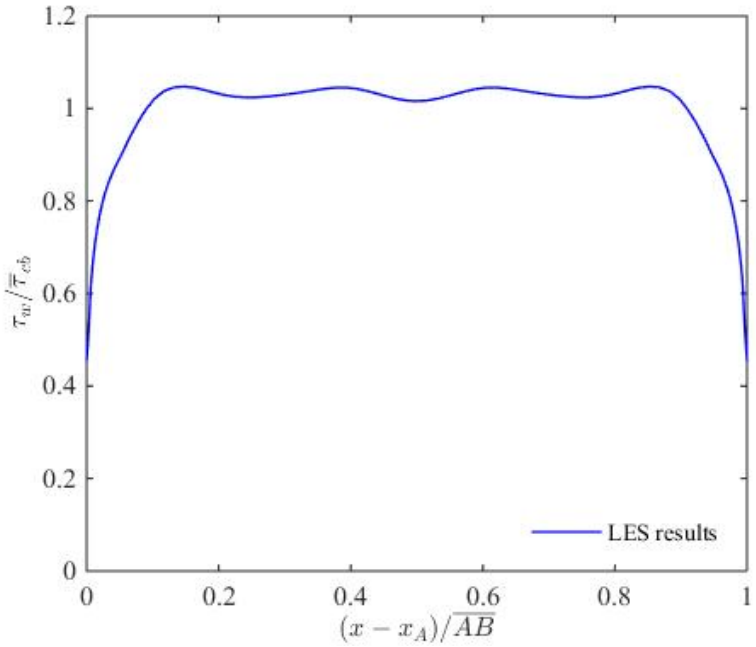
1.2
1
0.8
0.6
0.4
0.2
0
0
0.2
0.4
0.6
0.8
1
$\tau_w/\overline{\tau}_{cb}$
$(x - x_A)/\overline{AB}$
LES results

(c)

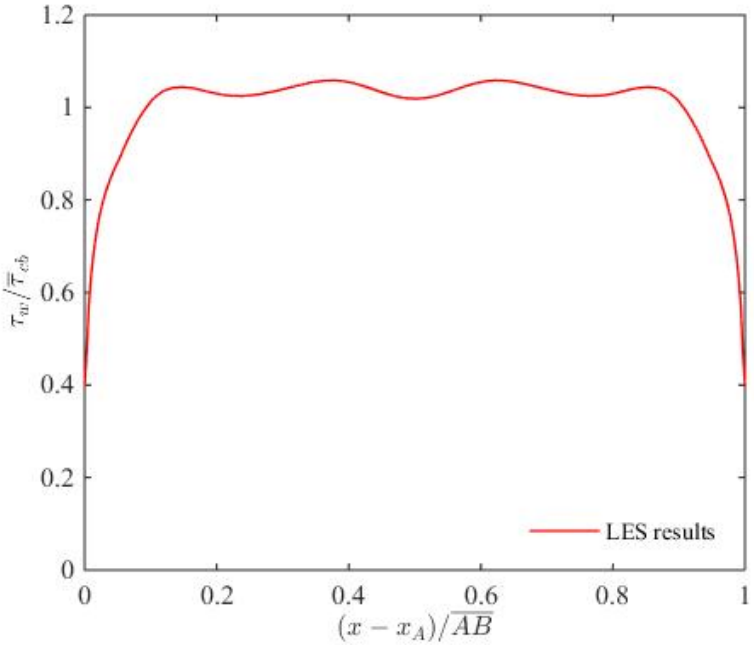

Figure 4.18 Distribution of predicted bed shear stress for Case 3, where x is the dimensionless cross-channel coordinate relative to the corner marked as A (Figure 3.4), and $\overline{AB}$ is the channel-bed width (Figure 3.4). Model times are t = 38 [panel (a)], 40 [panel (b)], and 42 s [panel (c)]

(a)

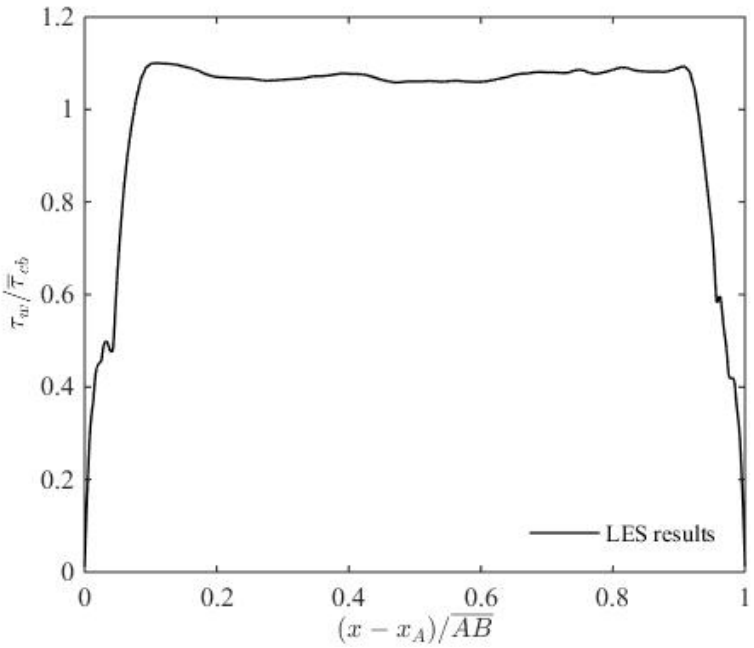

(b)

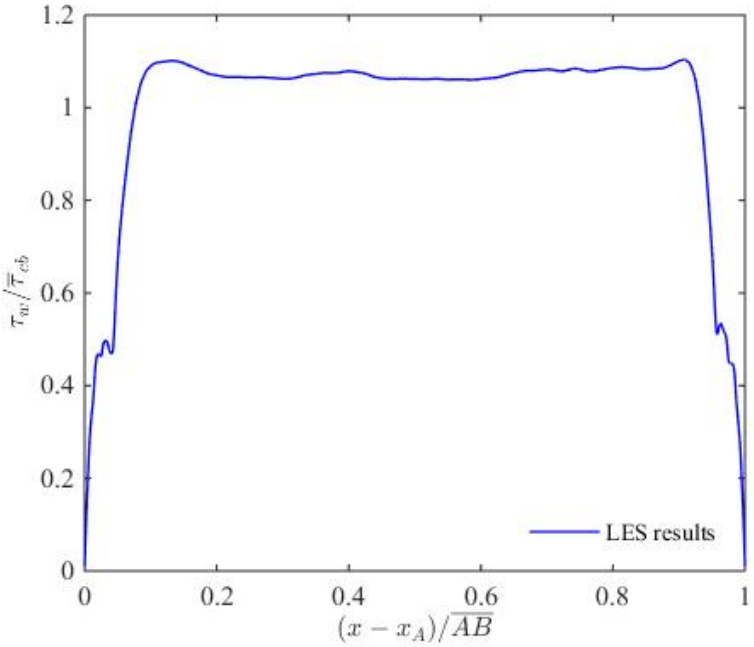

(c)

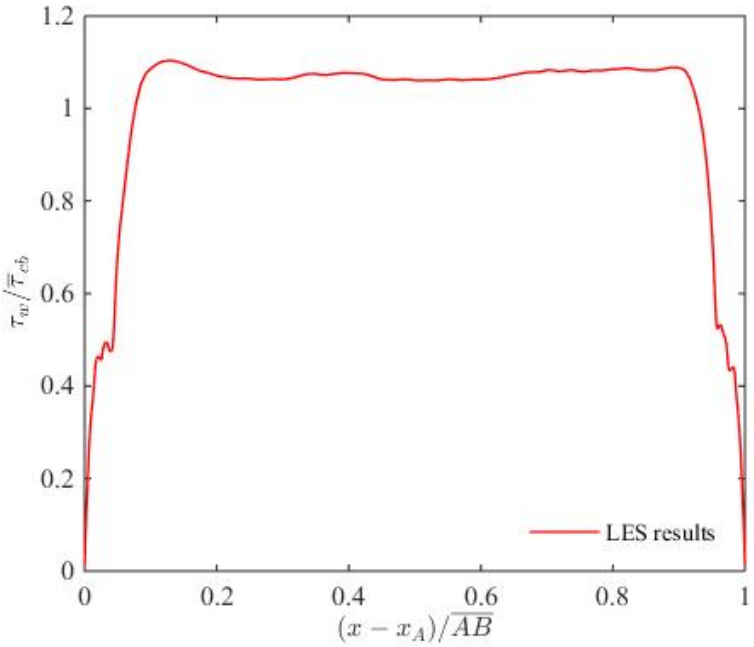

Figure 4.19 Distribution of predicted bed shear stress for Case 4, where x is the dimensionless cross-channel coordinate relative to the corner marked as A (Figure 3.5), and $\overline{AB}$ is the channel-bed width (Figure 3.5). Model times are t = 2.8 [panel (a)], 3.2 [panel (b)], and 3.6 s [panel (c)]

(a)

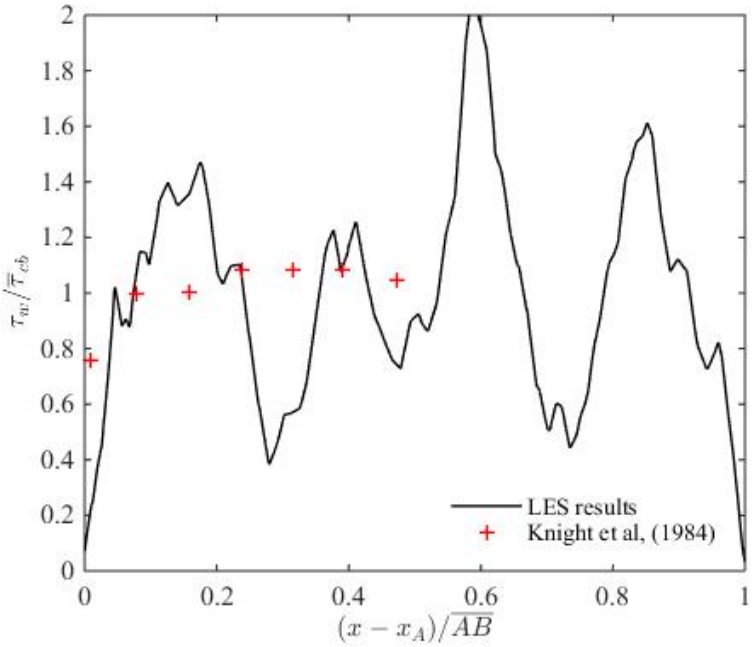
$\tau_w/\overline{\tau}_{cb}$
$(x - x_A)/\overline{AB}$
LES results
Knight et al, (1984)

(b)

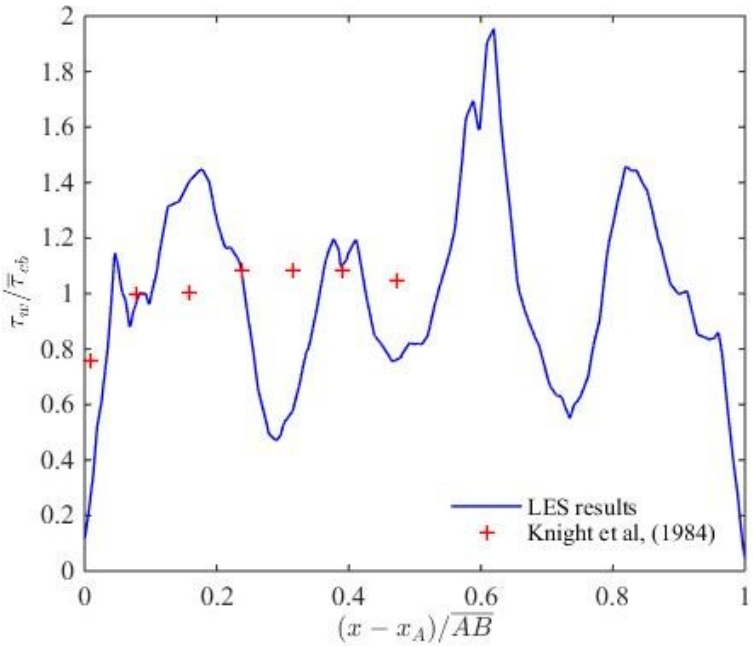
$\tau_w/\overline{\tau}_{cb}$
$(x - x_A)/\overline{AB}$
LES results
Knight et al, (1984)

(c)

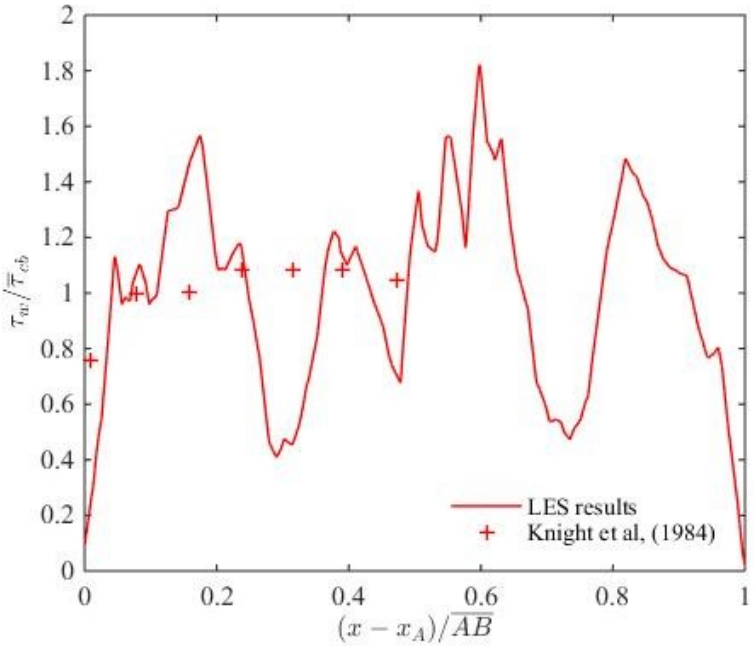

Figure 4.20 Distribution of predicted bed shear stress for Case 5, where x is the dimensionless cross-channel coordinate relative to the corner marked as A (Figure 3.6), and $\overline{AB}$ is the channel-bed width (Figure 3.6). Knight et al.'s (1984) measurements are shown as the symbols '+' for comparison. Model times are t = 20.48 [panel (a)], 21.12 [panel (b)], and 21.76 s [panel (c)]

4.4.3 Rectangular (Case 5) Open Channel with Blocks at the Channel-bed

For Case 5, Figure 4.20(a)-(c) show the distributions of bed shear stress at model times of t = 20.48, 21.12, and 21.76 s, respectively. Between panels (a), (b), and (c) of Figure 4.20, at the dimensionless distance (normalised by the channel bed-width) of 0.83, there are differences in shear stress as large as 0.06 $\bar{\tau}_{cb}$. More discussions of panels (c) of the figures are given below.

The introduction of blocks [Case 5, Figure 4.20(c)] causes significant spatial fluctuations in the distribution of local bed shear stress in the central portion of the channel-bed. The bed shear stresses decrease rapidly to zero toward the corners. As expected, the fluctuation patterns [Figure 4.20(c)] are not symmetrical about the central line of the channel. The normalised bed shear stresses by the mean value, $\bar{\tau}_{cb}$, range from 0.45 $\bar{\tau}_{cb}$ to 1.8 $\bar{\tau}_{cb}$ in the central portion of the channel-bed. There are no inflection points.

For Case 5, the predicted bed shear stresses [Figure 4.20(c)] distributed across the bed width are plotted through the experimental data of Knight et al. (1984). Note that the distribution of the predicted bed shear stress shown in Figure 4.20(c) corresponds to a snapshot at the model time (t = 21.76 s). LES realistically produced temporally evolving bed shear stresses in response to the turbulent conditions triggered by the blocks. It is possible to obtain time average of multiple snapshots, which is expected to yield a smooth distribution curve matching the experimental data.

In comparison to Case 2, the presence of blocks (Case 5) decreases the maximum bed shear stress by a factor of 1.30, and the mean bed shear stress by a factor of 2 (Table 4.3).

4.5 Distributions of Sidewall Shear Stress

Similar to the bed shear stress (Section 4.4), the sidewall shear stress is obtained from Equation [3.20]. Distributions of the sidewall shear stresses, τ_s, are plotted in Figures 4.21(a)-(c) to 4.25(a)-(c) for Cases 1 to 5, respectively. The corresponding longitudinal positions are z = −0.450, −0.439, −0.450, −0.439, and −0.813 m (Figures 3.2 to 3.6). Panels (a), (b) and (c) of the individual figures correspond to three different model times. In each of the plots, the local sidewall shear stresses have been normalised by the mean sidewall shear stress value $\bar{\tau}_{cs}$. The vertical axis shows the normalised distance (across the sidewall from the free surface to the channel-bed) by the flow depth. Cases 1 to 5 have a flow depth of 10.0, 9.75, 10.0, 9.75, and 9.75 cm, respectively (Figures 3.2 to 3.6). Table 4.3 gives a summary of the mean and maximum sidewall shear stresses.

(a)

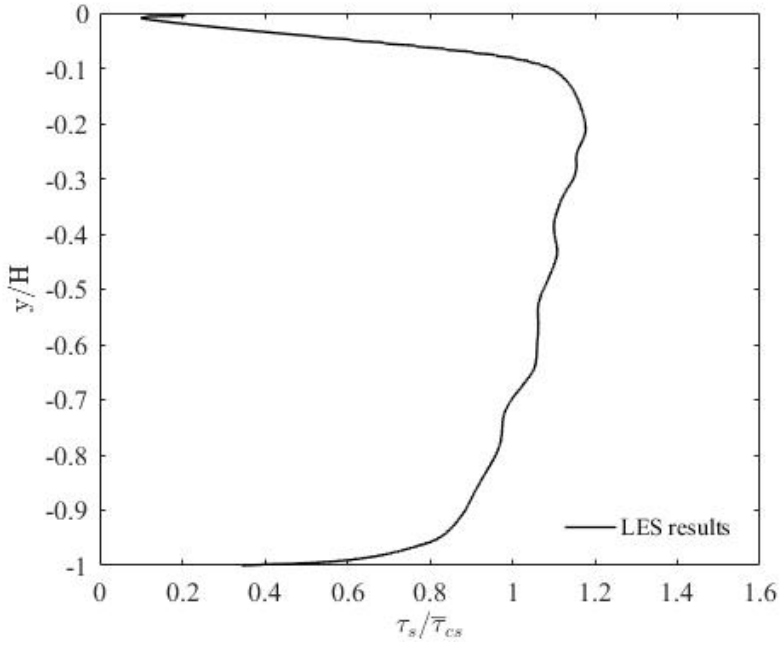
0
-0.1
-0.2
-0.3
-0.4
-0.5
-0.6
-0.7
-0.8
-0.9
-1
y/H
0
0.2
0.4
0.6
0.8
1
1.2
1.4
1.6
$\tau_s/\overline{\tau}_{cs}$
LES results

(b)

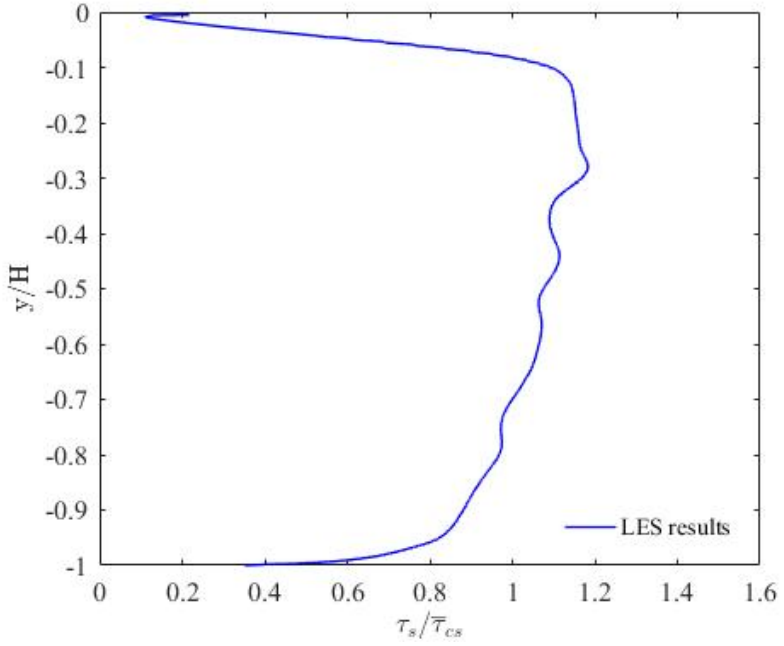
0
-0.1
-0.2
-0.3
-0.4
-0.5
-0.6
-0.7
-0.8
-0.9
-1
y/H
0
0.2
0.4
0.6
0.8
1
1.2
1.4
1.6
$\tau_s/\overline{\tau}_{cs}$
LES results

(c)

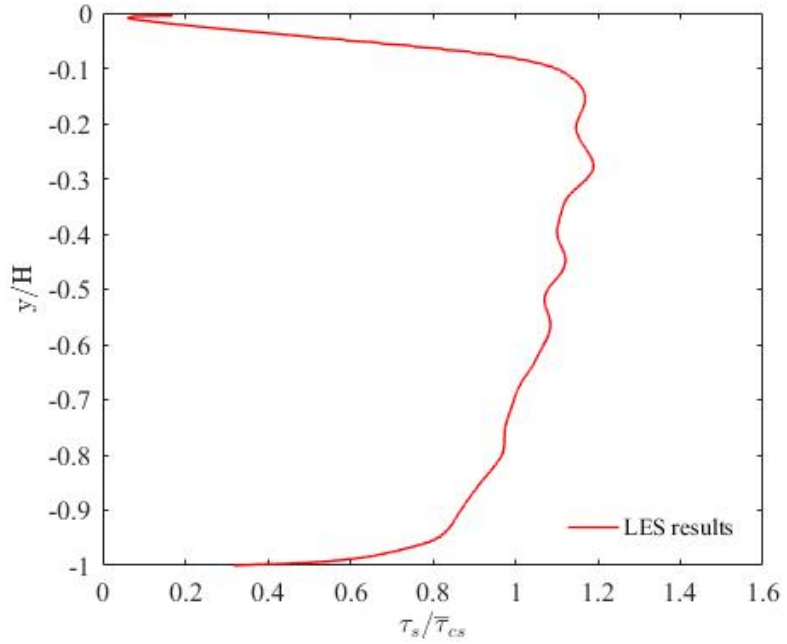

Figure 4.21 Distribution of predicted sidewall shear stress for Case 1. The depth of flow is H = 10 cm. Model times are t = 32 [panel (a)], 34 [panel (b)], and 36 s [panel (c)]

(a)

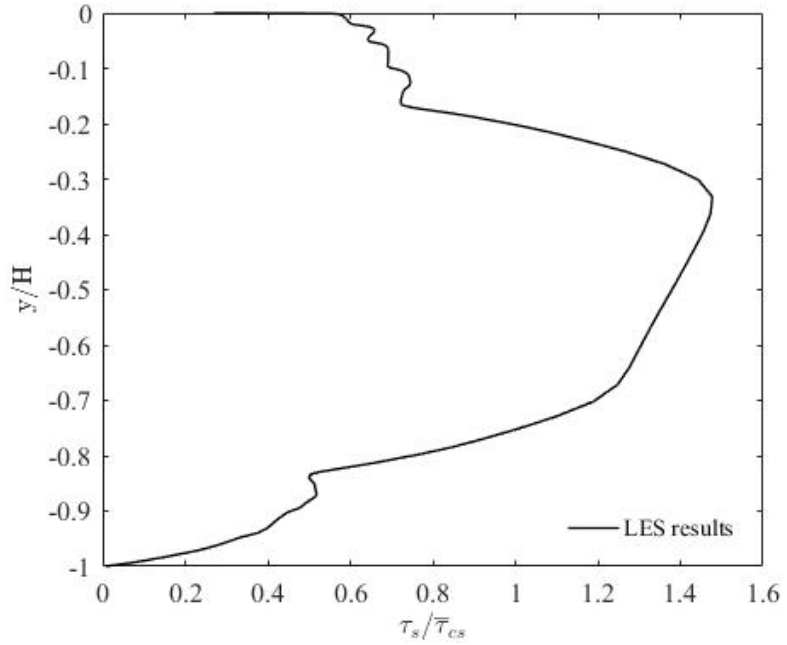

(b)

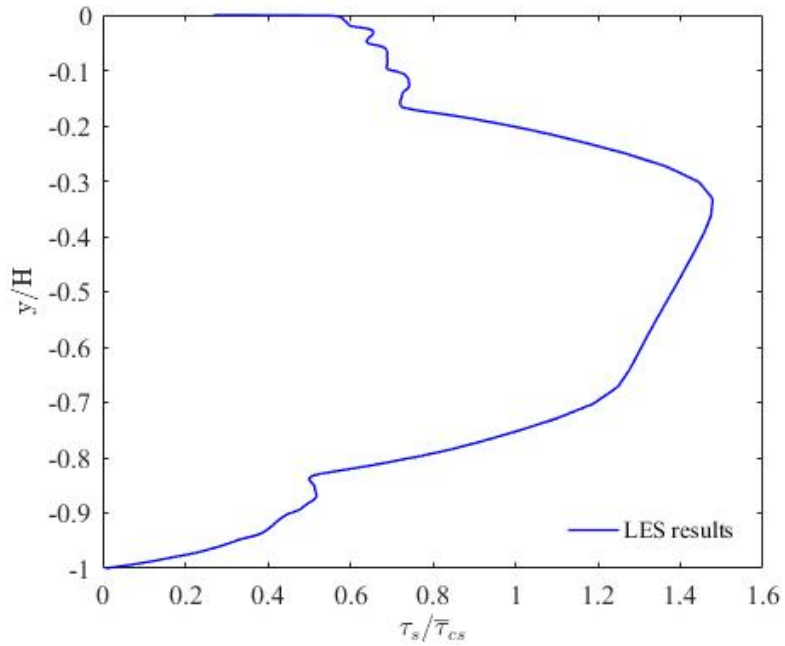

(c)

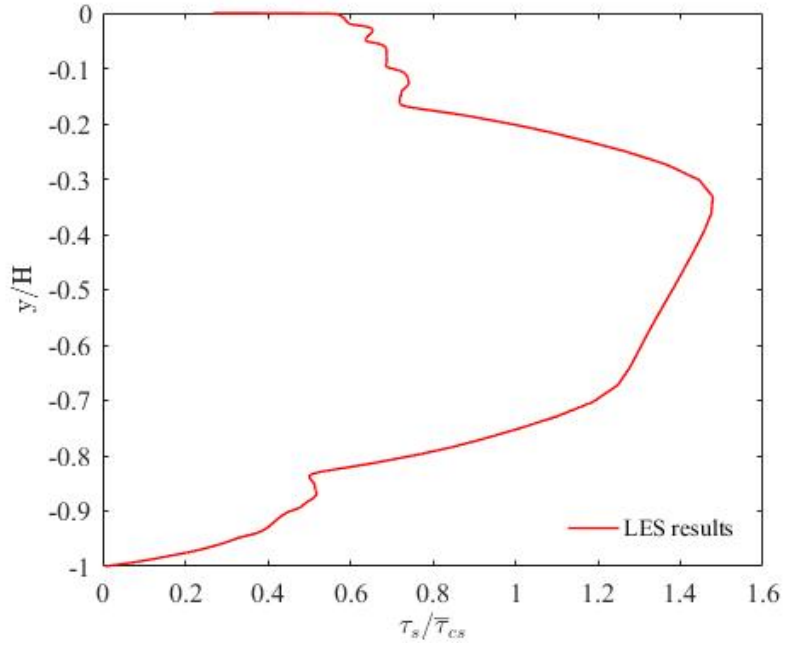

Figure 4.22 Distribution of predicted sidewall shear stress for Case 2. The depth of flow is H = 9.75 cm. Model times are t = 4.2 [panel (a)], 4.35 [panel (b)], and 4.5 s [panel (c)]

4.5.1 Trapezoidal (Case 1) and Rectangular (Case 2) Open Channels

For Case 1, Figure 4.21(a)-(c) show the distributions of sidewall shear stress at model times of t = 32, 34, and 36 s, respectively. Between panels (a), (b), and (c) of Figure 4.21, at the dimensionless distance (normalised by the flow depth) of −0.28, there are differences in shear stress as large as 0.034 $\bar{\tau}_{cb}$. For Case 2, the model times are 4.2 [Figure 4.22(a)], 4.35 [Figure 4.22(b)], and 4.5 s [Figure 4.22(c)]. Between panels (a), (b), and (c) of Figure 4.22, at the normalised distance of −0.055, there are differences in shear stress as large as 0.005 $\bar{\tau}_{cs}$. More discussions of panels (c) of the figures are given below.

For Case 1 [Figure 4.21(c)] and Case 2 [Figure 4.22(c)], the distributions of sidewall shear stresses τ_s under open water condition show a similar trend as the bed shear stresses [Case 1, Figure 4.16(c); Case 2, Figure 4.17(c)]. The sidewall shear stresses at the middle depth are much larger than near the top and bottom boundaries. The sidewall shear stresses decrease dramatically toward zero at the free surface and the channel-bed. The normalised sidewall shear stresses in the corner regions have different distributions in the trapezoidal channel [Case 1, Figure 4.21(c)] and the rectangular channel section [Case 2, Figure 4.22(c)].

For Case 2, the distributions of sidewall shear stresses have two inflection points, one being near the free surface, and the other near the channel-bed [Figure 4.22(c)]. These inflection points are symmetrically about the middle depth, located at 15 and 85% the flow depth below the free surface. The sidewall shear stresses at the inflection points have a values of approximately 60% the mean sidewall shear stress. For Case 1, there are moderate spatial fluctuations around the middle depth [Figure 4.21(c)], but there is no inflection point.

For Case 1 and Case 2, the distributions of sidewall shear stress are not symmetrical about the middle depth [Figure 4.21(c) and Figure 4.22(c)], which is different from the symmetrical distributions of the bed shear stress [Figure 4.16(c) and Figure 4.17(c)]. The sidewall shear stresses [Figure 4.21(c) and Figure 4.22(c)] have a maximum value (Table 4.3) of 1.16 $\bar{\tau}_{cs}$ for Case 1 and 1.45 $\bar{\tau}_{cs}$ for Case 2. The maximum values are located at a vertical distance of 72 and 65% the total flow depth above the channel-bed for Case 1 and Case 2, respectively. These locations are closer to the free surface than to the channel-bed.

For Case 1, the sidewall shear stress has larger maximum and mean values than the bed shear stress, by a factor of 1.48 and 1.32, respectively (Table 4.3). For Case 2, the conditions are similar, with greater maximum and mean sidewall shear stresses, by a factor of 1.83 and 1.38, respectively.

(a)

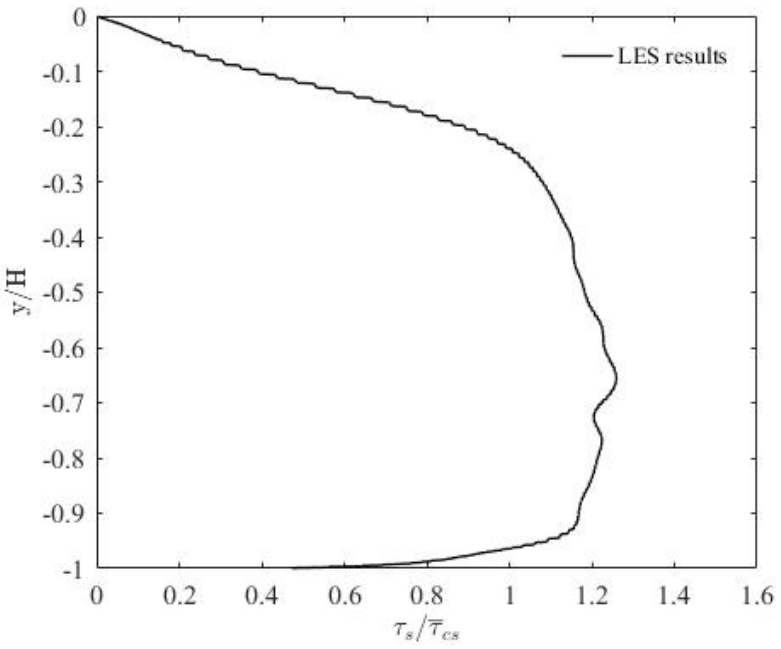

(b)

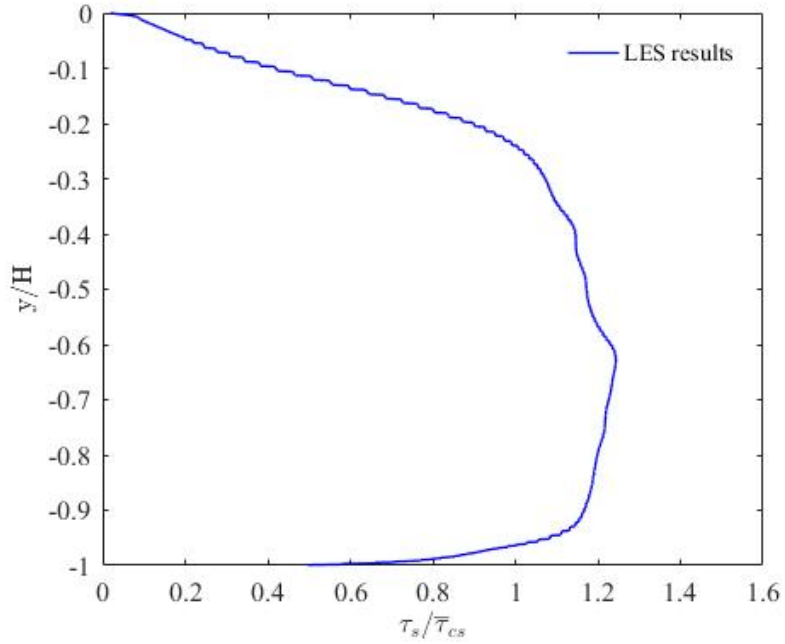

(c)

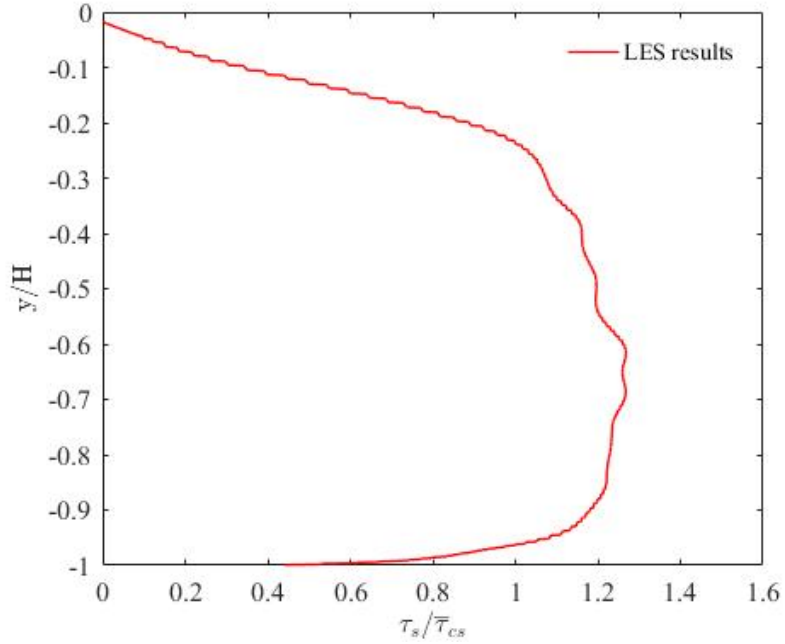

Figure 4.23 Distribution of predicted sidewall shear stress for Case 3. The depth of flow is H = 10 cm. Model times are t = 38 [panel (a)], 40 [panel (b)], and 42 s [panel (c)]

(a)

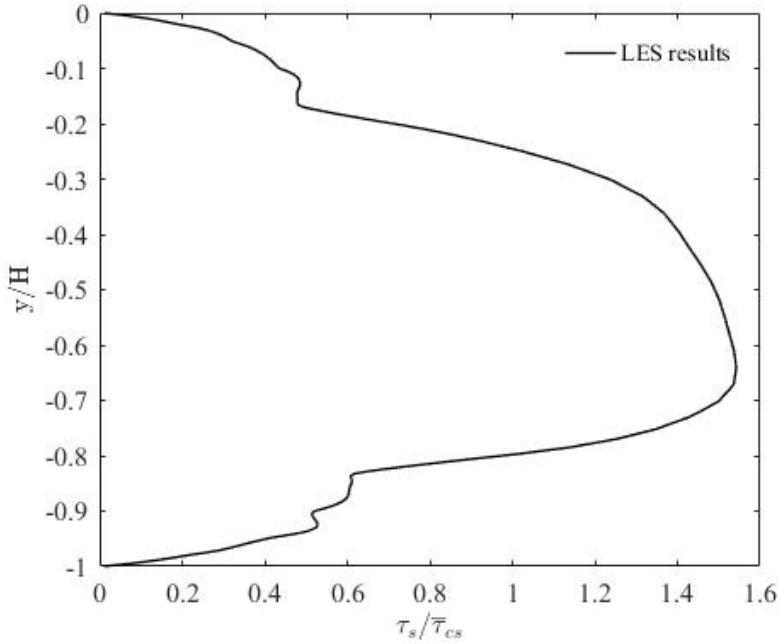
LES results
y/H
0
-0.1
-0.2
-0.3
-0.4
-0.5
-0.6
-0.7
-0.8
-0.9
-1
0
0.2
0.4
0.6
0.8
1
1.2
1.4
1.6
$\tau_s/\overline{\tau}_{cs}$

(b)

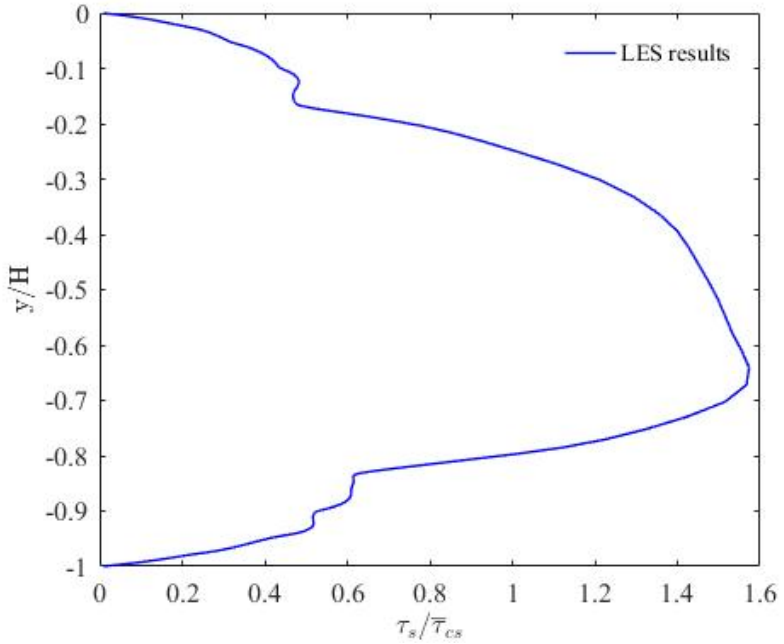
LES results
y/H
0
-0.1
-0.2
-0.3
-0.4
-0.5
-0.6
-0.7
-0.8
-0.9
-1
0
0.2
0.4
0.6
0.8
1
1.2
1.4
1.6
$\tau_s/\overline{\tau}_{cs}$

(c)

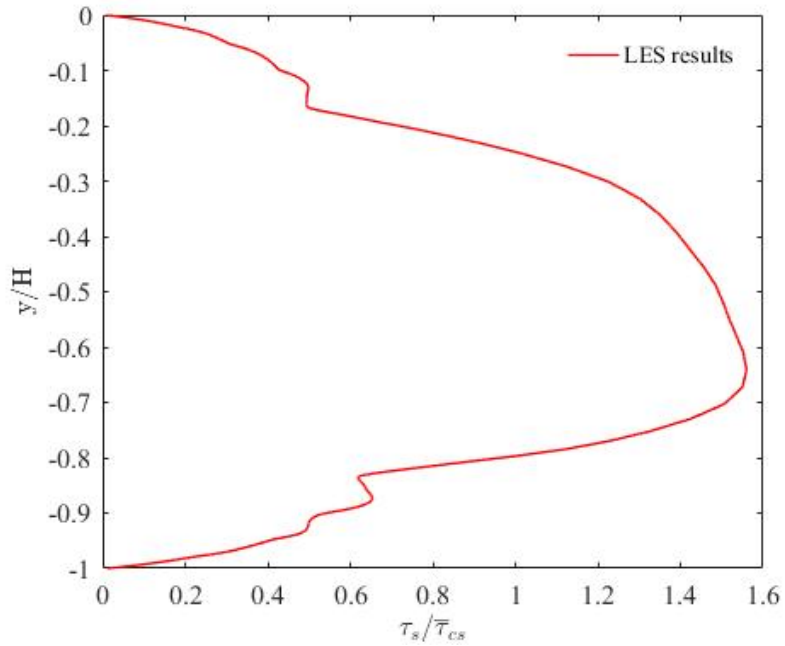

Figure 4.24 Distribution of predicted sidewall shear stress for Case 4. The depth of flow is H = 9.75 cm. Model times are t = 2.8 [panel (a)], 3.2 [panel (b)], and 3.6 s [panel (c)]

4.5.2 Trapezoidal (Case 3) and Rectangular (Case 4) Ice-Covered Channels

For Case 3, Figure 4.23(a)-(c) show the distributions of sidewall shear stress at model times of t = 38, 40, and 42 s, respectively. Between panels (a), (b), and (c) of Figure 4.23, at the dimensionless distance (normalised by the flow depth) of −0.70, there are differences in shear stress as large as 0.03 $\bar{\tau}_{cs}$. For Case 4, the model times are 2.8 [Figure 4.24(a)], 3.0 [Figure 4.24(b)], and 3.2 s [Figure 4.24(c)]. Between panels (a), (b), and (c) of Figure 4.24, at the normalised distance of −0.89, there are differences in shear stress as large as 0.044 $\bar{\tau}_{cs}$. More discussions of panels (c) of the figures are given below.

Under ice-covered condition [Case 3, Figure 4.23(c); Case 4, Figure 4.24(c)], the distributions of sidewall shear stresses show some features similar to open water condition [Case 1, Figure 4.21(c); Case 2, Figure 4.22(c)]. Sidewall shear stresses around the middle flow depth are higher than those near the channel-bed and free surface. The sidewall shear stress is insignificantly small at the free

surface and the channel-bed. The normalised sidewall shear stresses have different distributions in the corner regions between Case 3 [Figure 4.23(c)] and Case 4 [Figure 4.24(c)].

For Case 4 [Figure 4.24(c)], the distribution of sidewall shear stress shows inflection points at the same locations as Case 2 [Figure 4.22(c)]. For Case 3 [Figure 4.23(c)], the sidewall shear stress shows spatial fluctuations in the central portion of the sidewalls.

For both Case 3 [Figure 4.23(c)] and Case 4 [Figure 4.24(c)], the distributions of sidewall shear stresses are asymmetrical about the middle depth. The sidewall shear stresses (Table 4.3) have a maximum value of $1.25\,\bar{\tau}_{cs}$ and $1.55\,\bar{\tau}_{cs}$, located at a vertical distance (above the channel-bed) of 30 and 35% the flow depth [Figure 4.23(c) and Figure 4.24(c)], respectively. These locations are closer to the bed than to the free water surface.

For both Case 3 and Case 4, the sidewall shear stresses have a maximum value of 1.18 and 1.42 times larger than the maximum bed shear stresses, respectively. However, the mean shear stress value on the sidewalls and channel-bed are almost the same for each of the two cases (Table 4.3).

For Case 3 and Case 4, the mean and maximum sidewall shear stresses are 1.2 times larger than those under open water condition (Case 1 and Case 2, Table 4.3).

(a)

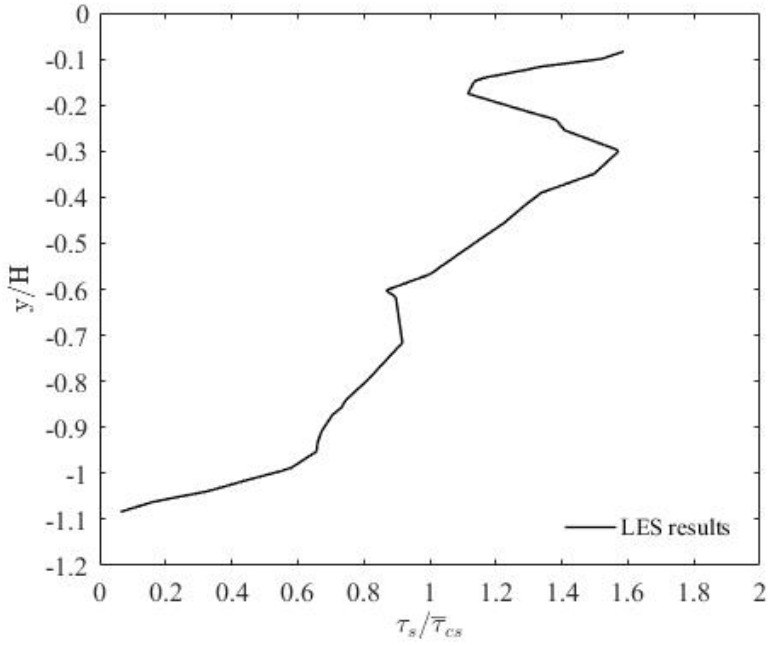
0
-0.1
-0.2
-0.3
-0.4
-0.5
-0.6
-0.7
-0.8
-0.9
-1
-1.1
-1.2
y/H
0
0.2
0.4
0.6
0.8
1
1.2
1.4
1.6
1.8
2
$\tau_s/\overline{\tau}_{cs}$
LES results

(b)

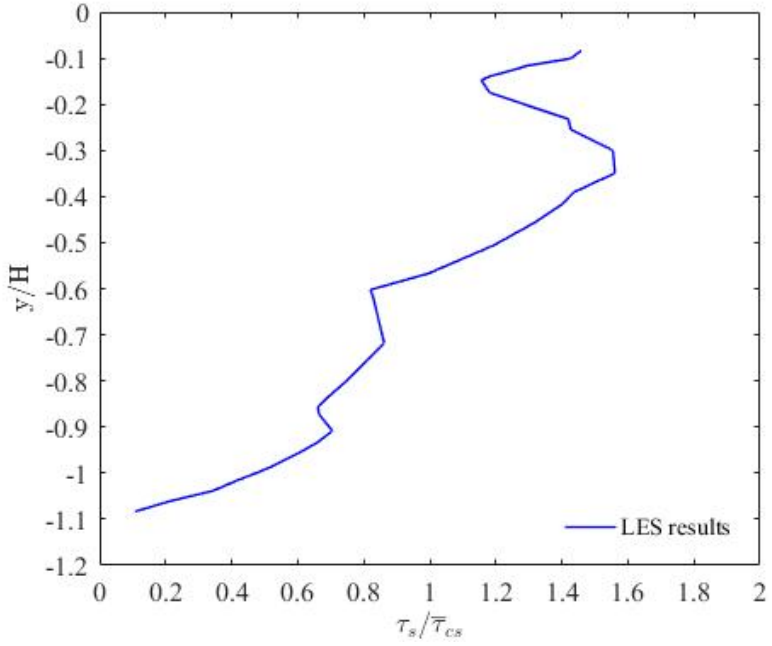
0
-0.1
-0.2
-0.3
-0.4
-0.5
-0.6
-0.7
-0.8
-0.9
-1
-1.1
-1.2
y/H
0
0.2
0.4
0.6
0.8
1
1.2
1.4
1.6
1.8
2
$\tau_s/\overline{\tau}_{cs}$
LES results

(c)

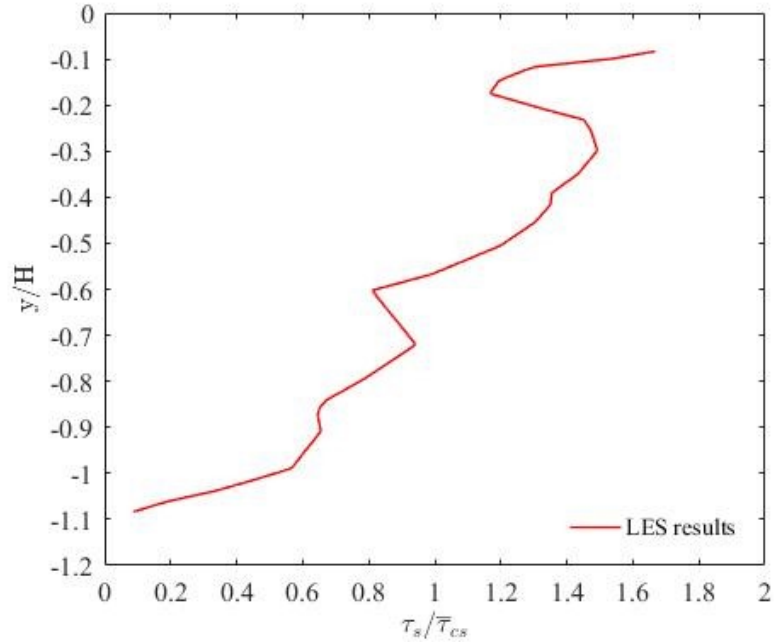

Figure 4.25 Distribution of predicted sidewall shear stress for Case 5. The depth of flow is H = 9.75 cm. Model times are t = 20.48 [panel (a)], 21.12 [panel (b)], and 21.76 s [panel (c)]

4.5.3 Rectangular (Case 5) Open Channel with Blocks at the Channel-bed

For Case 5, Figure 4.25(a)-(c) show the distributions of sidewall shear stress at model times of t = 20.48, 21.12, and 21.76 s, respectively. Between panels (a), (b), and (c) of Figure 4.25, at the dimensionless distance (normalised by the flow depth) of −0.34, there are differences in shear stress as large as 0.11 $\bar{\tau}_{cs}$. More discussions of panels (c) of the figures are given below.

For Case 5 [Figure 4.25(c)], the local sidewall shear stresses fluctuate to a large extent across the sidewall width. The sidewall shear stress has a small value at the channel-bed and increases toward the free surface. Unlike Case 2 [Figure 4.22(c)], the distribution of the sidewall shear stress for Case 5 has no inflection points. In comparison to Case 2 [Figure 4.22(c)], the presence of blocks (Case 5) decreases the maximum of bed shear stress by a factor of 2.45, and the mean bed shear stress by a factor of 2.77 (Table 4.3). For Case 5, the maximum sidewall shear stress is slightly lower than the maximum bed shear stress, whereas the mean sidewall shear stress is moderately higher than the mean bed shear stress (Table 4.3).

5. Discussions and Conclusions

5.1 Discussions

In this LES study, we predict that the peak boundary shear stress does not necessarily occur at the same location as the maximum primary velocity. This finding is consistent with the results of Chiu and Lin (1983), Knight et al. (1984), and Kabiri-Samani et al. (2012). Specifically, the results for Cases 1 to 4 show that the maximum velocity location deviates from the location of the maximum shear stress. A plausible explanation is the effect of the secondary flow. This study shows that the distributions of bed and sidewall shear stresses for a rectangular channel contain inflection points (Case 2 and Case 4). Knight et al. (1984) suggested that bottom vortices are responsible for the existence of the inflection points. In a trapezoidal channel (Case 1 and Case 3), both the bed and sidewall shear stresses show spatial fluctuations. Such features were reported earlier in Nezu & Nakagawa (1984), who attributed the fluctuations to turbulent vortices.

For given discharge and bed slope, the resistance added by a floating ice cover can increase the water depth. Smith & Ettema (1997) argued that the primary effect was a reduction to the bed shear stress, which in turn would reduce sediment bedload transport rate. This study has not examined this effect. Our study focused on the changes in flow characteristics between open water and ice-covered conditions, with the same flow depth. The presence of an ice cover is shown to increase the mean and maximum boundary shear stresses, and to cause a change to the location of the maximum velocity.

In an ice-covered channel (Case 3 and Case 4), vertical profiles of the streamwise water velocity are not symmetrical about the middle depth, even if the channel-bed and the ice cover underside have the same roughness. This prediction is different from Tsai & Ettema's (1994) theory of two-layer flow. The theory predicts that the plane of maximum velocity is at the middle depth coincident with the plane of zero shear stress for boundaries with the same roughness. In this study, the ice cover and channel bed are treated as no-slip walls, which is expected to lead to symmetrical flow. However, the velocity profiles show a maximum value at a depth closer to the channel-bed. This is an interesting phenomenon worthy further investigations.

In an experimental study of rough open channel flow, Tominaga et al. (1989) reported multi-cellular secondary currents, with upward and downward motions. These motions are thought to affect the distribution of bed shear stress, causing an increase in the shear stress in the downflow regions and a decrease in the upflow regions. Their finding supports the predictions of spatial fluctuations in bed shear stress for Case 5. The blocks being added to the bed for the case may have contributed to an increase in upward and downward cellular motions. The high local bed shear stresses [Figure 4.20(c)] may be associated with the downward motions, whereas the relatively low local bed shear stress associated with the upward motions. It is understood that the blocks enhance the turbulent levels and hence significantly change the flow characteristics from the condition without blocks. Higher turbulent levels mean a better reflection to flow conditions in natural channels. The occurrence of the maximum sidewall stress near the free water surface may be a result of the secondary flow.

5.2 Conclusions

This thesis reports LES results of boundary shear stress (BSS) distributions along the wetted perimeters of channel sections. These include a trapezoidal open channel (Case 1), a rectangular open channel (Case 2), a trapezoidal ice-covered channel (Case 3), a rectangular ice-covered channel (Case 4), and a rectangular open channel with blocks near the inlet (Case 5). An examination of the LES results has led to the following conclusions:

(1) LES gives acceptable BSS predictions. The predicted BSS varies across the channel-bed, true for the trapezoidal and rectangular channel sections under both open water and ice-covered conditions. BSS values are relatively high within the largest central portion of the bed and sidewall widths, and drop rapidly toward the corners of the channel sections (Cases 1 to 4). The predicted BSS distribution across the bed width is in reasonable agreement with available experimental data. Under open water condition, the BSS distribution across its sidewalls shows a maximum value at a location closer to the free surface than to the bed, whereas under ice-covered condition, the location of the maximum shear stress is closer to the bed than to the ice-cover underside.

(2) Predicted turbulent flows in the channel sections show features consistent with literature reports. The BSS distributions in the rectangular channels show symmetrical inflection points in the corner regions (Case 2 and Case 4). In the central region of trapezoidal channel sections, BSS has small spatial fluctuations probably caused by secondary flow (Case 1 and Case 3). The normalised bed shear stresses (normalising the local bed and sidewall shear stresses by the spatially averaged values for the bed and sidewalls, respectively) in the corner regions have different distributions between the trapezoidal channel and the rectangular channel section. The peak BSS does not necessarily need to be in the same location as the maximum primary velocity. The maximum and mean sidewall shear stress values are generally larger than their corresponding bed shear stress values (Cases 1 to 4).

(3) Predictions of velocity profiles and contours exhibit features that are consistent with the literature. The maximum velocity occurs near the free surface under open water condition. Transition points of changing velocity gradients are at a distance (above the bed or below the ice cover underside) of 15% the total flow depth. There is a core of relatively high

velocities away from the solid boundaries. Flow velocities decrease in magnitude gradually with an increasing distance from the core centre, dropping rapidly to zero toward the solid boundaries.

(4) In LES, it is appropriate to treat ice cover as a no-slip boundary, being added to the top of an open channel. The presence of ice cover (Case 3 and Case 4) causes significant changes in flow structure and shear stress, in comparison to open water condition.

- Velocity profiles show a maximum value at more or less the middle depth. The frictional effects of ice cover force the maximum velocity to occur at a lower depth, in comparison to open water condition, and at the same time cause an increase in the maximum flow velocity.
- Relative to open water condition, the presence of ice cover leads to slightly larger spatial fluctuations in BBS in trapezoidal channel sections. The ice cover increases the mean and maximum bed shear stress by 65%, and the mean and maximum sidewall shear stress by 20% in the rectangular and trapezoidal channel sections.

(5) Small blocks added to the channel bed near the inlet (Case 5) enhance turbulence intensity, with significant effects on shear stress and flow characteristics.

- At the channel bed, the shear stresses show spatial fluctuations to a large extent, and are no longer symmetrical. On the sidewalls, the shear stresses also fluctuate substantially; the maximum shear stress occurs at the free surface. The maximum and mean boundary shear stresses are larger for Case 2 (the same channel geometry without blocks) than for Case 5.
- In comparison to Case 2, the blocks result in less regular contours of water velocities, and a larger maximum velocity, which occurs at the free surface. Below the free surface to about 70% the total flow depth below, the flow velocities are high and close to the maximum velocity.

(6) The use of a proper setup and mesh configurations has been demonstrated as important in LES. In particular, it is crucial to implement mesh refinements adjacent to the channel-bed, sidewalls, and corner regions. The wall distance of the first node off a solid surface should

not exceed unity. This means that reliable BSS predictions require to resolve the viscous sublayer. This is not the case in most of the existing LES applications to open channel flow. For given hydraulic conditions and channel geometry, it is necessary to test the sensitivity of LES predictions to slight changes in mesh size and configurations.

(7) In general, LES incurs high computing costs. The costs can effectively be reduced by using User Defined Functions and symmetrical conditions, and by adjusting the ratio of grid length. Given the high costs and often technical difficulties in obtaining BSS measurements, LES offers an attractive complement to physical models, laboratory experiments, and field measurements.

5.3 Suggestions for Future Work

Future work should expand the research on the following aspects:

- First, investigate BSS in channels of a wide range of aspect ratios, which is known to be an important factor in determining BSS distribution.
- Second, roughness effects on BSS have been ignored in the present study. This is due to a lack of ability to incorporate surface roughness in LES. It would be interesting to expand the prediction capacity to include surface roughness.
- Water flows in natural channels are always turbulent, characterised by high Reynolds numbers. With an exponential increase in computing power, one should perform LES at high Reynolds numbers. The results would better reflect reality.

REFERRENCES

Abril, J., & Knight, D. (2004). Stage-discharge prediction for rivers in flood applying a depth-averaged model. *Journal of Hydraulic Research, 42*(6), 616-629.

Ackerman, J. D., & Hoover, T. M. (2001). Measurement of local bed shear stress in streams using a Preston-static tube. *Limnology and Oceanography, 46*(8), 2080-2087.

Afzalimehr, H., & Rennie, C. D. (2009). Determination of bed shear stress in gravel-bed rivers using boundary-layer parameters. *Hydrological Sciences Journal, 54*(1), 147-159.

Aghaji Zare, S. G., Moore, S. A., Rennie, C. D., Seidou, O., Ahmari, H., & Malenchak, J. (2015). Boundary Shear Stress in an Ice-Covered River during Breakup. *Journal of Hydraulic Engineering,* 142(4), 04015065.

Akan, A. O. (2001). Tractive force channel design aid. *Canadian Journal of Civil Engineering, 28*(5), 865-867.

ANSYS. (2013a). ANSYS Fluent Theory guide. Release 15.0, ANSYS, *Inc., Canonsburg, PA 15317.*

ANSYS. (2013b). ANSYS Fluent user's guide. Release 15.0, ANSYS, *Inc., Canonsburg, PA 15317.*

ANSYS. (2013c). ANSYS Workbench user's guide. Release 15.0, ANSYS, *Inc., Canonsburg, PA 15317.*

Attar, S., & Li, S. (2012). Data-fitted velocity profiles for ice-covered rivers. *Canadian Journal of Civil Engineering, 39*(3), 334-338.

Bagnold, R. (1955). Some flume experiments on large grains but little denser than the transporting fluid, and their implications. *Proceedings of the Institution of Civil Engineers, 4*(2), 174-205.

Bardina, J., Ferziger, J. H., & Reynolds, W. C. (1983). *Improved turbulence models based on large eddy simulation of homogeneous, incompressible, turbulent flows* Stanford University.

Barnes, M. P., O'Donoghue, T., Alsina, J., & Baldock, T. (2009). Direct bed shear stress measurements in bore-driven swash. *Coastal Engineering, 56*(8), 853-867.

Beltaos, S. (2011). Developing winter flow rating relationships using slope-area hydraulics. *River Research and Applications, 27*(9), 1076-1089.

Biron, P. M., Lane, S. N., Roy, A. G., Bradbrook, K. F., & Richards, K. S. (1998). Sensitivity of bed shear stress estimated from vertical velocity profiles: The problem of sampling resolution. *Earth Surface Processes and Landforms, 23*(2), 133-139.

Birtwell, I. K., & Secretariat, C. S. A. (1999). *The effects of sediment on fish and their habitat* Fisheries and Oceans Canada.

Blanckaert, K. (2010). Topographic steering, flow recirculation, velocity redistribution, and bed topography in sharp meander bends. *Water Resources Research, 46*(9)

Blanckaert, K., & McLelland, S. (2009). Simultaneous measurements with 3D PIV and acoustic doppler velocity profiler. Paper presented at the *Water Engineering for Sustainable Environment: 33rd IAHR Congress; 9-14 August 2009, Vancouver, British Columbia, Canada,*

Broglia, R., Pascarelli, A., & Piomelli, U. (2003). Large-eddy simulations of ducts with a free surface. *Journal of Fluid Mechanics, 484*, 223-253.

Castanedo, S., Medina, R., & Mendez, F. J. (2005). Models for the turbulent diffusion terms of shallow water equations. *Journal of Hydraulic Engineering, 131*(3), 217-223.

Cater, J. E., & Williams, J. J. (2008). Large eddy simulation of a long asymmetric compound open channel. *Journal of Hydraulic Research, 46*(4), 445-453.

Chanson, H. (2000). Boundary shear stress measurements in undular flows: Application to standing wave bed forms. *Water Resources Research, 36*(10), 3063-3076.

Chen, G., Gu, S., Huai, W., & Zhang, Y. (2015). Boundary shear stress in rectangular ice-covered channels. *Journal of Hydraulic Engineering, 141*(6), 06015005.

Chiu, C., & Chiou, J. (1986). Structure of 3-D flow in rectangular open channels. *Journal of Hydraulic Engineering, 112*(11), 1050-1067.

Chiu, C., & Lin, G. (1983). Computation of 3-D flow and shear in open channels. *Journal of Hydraulic Engineering, 109*(11), 1424-1440.

Chou, Y., & Fringer, O. B. (2010). A model for the simulation of coupled flow-bed form evolution in turbulent flows. *Journal of Geophysical Research: Oceans, 115*(C10)

Chow, V. T. (1959). *Open-channel hydraulics*. New York: McGraw-Hill.

Çiray, C. (1970). On wall shear stress determination(wall shear stress distribution in noncircular ducts with steady incompressible fluid flow). *Middle East Technical University Journal of Pure and Applied Sciences, 3*, 41-54.

Clauser, H., & Li, C. H. (1954). Adsorption chromatography of hypophyseal growth hormone and other proteins on hyflo super-cel columns. *Journal of the American Chemical Society, 76*(17), 4337-4341.

Cokljat, D., & Younis, B. (1995). Second-order closure study of open-channel flows. *Journal of Hydraulic Engineering, 121*(2), 94-107.

Constantinescu, G., Koken, M., & Mccoy, A. (2008). In DohmenJanssen C. H.,SJMH (Ed.), *A large eddy simulation study of the bed shear stress distributions around isolated and multiple groynes*

Cruff, R. (1965). *Cross-Channel Transfer of Linear Momentum in Smooth Rectangular Channels,*

Davidian, J., & Cahal, D. (1963). Distribution of shear in rectangular channels. *Article, 113*, C206-C208.

De Cacqueray, N., Hargreaves, D. M., & Morvan, H. P. (2009). A computational study of shear stress in smooth rectangular channels. *Journal of Hydraulic Research, 47*(1), 50-57.

Deardorff, J. W. (1970). A numerical study of three-dimensional turbulent channel flow at large Reynolds numbers. *Journal of Fluid Mechanics*, 41(02), 453-480.

Deardorff, J. (1973). The use of subgrid transport equations in a three-dimensional model of atmospheric turbulence. *Journal of Fluids Engineering, 95*(3), 429-438.

Dolgopolova, E. (1998). Velocity distribution in ice-covered flow. Paper presented at the *Proc. Inter. 14th Symp. on Ice, Potsdam: IAHR,* 544-560.

Einstein, H. A. (1942). Formulas for the transportation of bed load. *Trans.ASCE Paper, 2140*, 561-597.

Ervine, D. A., Babaeyan-Koopaei, K., & Sellin, R. H. (2000). Two-dimensional solution for straight and meandering overbank flows. *Journal of Hydraulic Engineering, 126*(9), 653-669.

Ettema, R., Braileanu, F., & Muste, M. (2000). Method for estimating sediment transport in ice-covered channels. *Journal of Cold Regions Engineering, 14*(3), 130-144.

Ferriss, D. (1965). *Preston tube measurements in turbulent boundary layers and fully developed pipe flow* Citeseer.

Ferziger, J. H., & Shaanan, S. (1976). Effect of anisotropy and rotation on turbulence production. *Physics of Fluids (1958-1988), 19*(4), 596-597.

Fox, R. W., & McDonald, A. T. (1992). *Introduction to fluid mechanics* (4th ed.). New York: J. Wiley.

Fraselle, Q., Bousmar, D., & Zech, Y. (2010). Experimental investigation of sediment deposition on floodplains. Paper presented at the *Proc. River Flow 2010 International Conference on Fluvial Hydraulics, Braunschweig, Germany,* 823-830.

Fujisawa, N., Aoyama, A., & Kosaka, S. (2003). Measurement of shear-stress distribution over a surface by liquid-crystal coating. *Measurement Science and Technology, 14*(9), 1655.

Gavrilakis, S. (1992). Numerical simulation of low-reynolds-number turbulent flow through a straight square duct. *Journal of Fluid Mechanics, 244*, 101-129.

Ghosh, S., & Jena, S. (1971). Boundary shear distribution in open channel compound. *Proceedings of the Institution of Civil Engineers, 49*(4), 417-430.

Ghosh, S., & Roy, N. (1970). Boundary shear distribution in open channel flow. *Journal of the Hydraulics Division,*

Graf, W. H. (1984). *Hydraulics of sediment transport* Water Resources Publication.

Guo, J., & Julien, P. Y. (2005). Shear stress in smooth rectangular open-channel flows. *Journal of Hydraulic Engineering, 131*(1), 30-37.

Healy, D., & Hicks, F. (2004). Index velocity methods for winter discharge measurement. *Canadian Journal of Civil Engineering, 31*(3), 407-419.

Henderson, F. M. (1966). *Open channel flow*. New York: Macmillan.

Hilldale, R. C., & Baird, D. C. (2002). Lateral variation of bed shear stress and the presence of secondary currents in the low flow conveyance channel of the middle rio grande. Paper presented at the *Hydraulic Measurements and Experimental Methods 2002,* 1-9.

Hopkinson, L., & Wynn-Thompson, T. (2012). Streambank shear stress estimates using turbulent kinetic energy. *Journal of Hydraulic Research, 50*(3), 320-323.

Houjou, K., & Ishii, C. (1990). Calculation of boundary shear stress in open channel flow. *Journal of Hydrosclence and Hydraulic Engineering, 8*(2), 21-23.

Huser, A., & Biringen, S. (1993). Direct numerical simulation of turbulent flow in a square duct. *Journal of Fluid Mechanics, 257*, 65-95.

Imamoto, H., & Ishigaki, T. (1985). Velocity vector measurement by laser doppler velocimeter in an open channel flow. *Bulletin of the Disaster Prevention Research Institute, University of Kyoto,* (28), 477-487.

Inkratas, C., Gharabaghi, B., Beltaos, S., & Krishnappan, B. (2009). 3D modelling of ice-covered flows in the vicinity of a deep hole in the east channel of the mackenzie delta, NWT. *Canadian Journal of Civil Engineering, 36*(5), 791-800.

Jazizadeh, F., & Zarrati, A. (2008). Development of a three-dimensional numerical model to solve shallow-water equations in compound channels. *Canadian Journal of Civil Engineering, 35*(9), 963-974.

Jin, Y., Steffler, P. M., & Hicks, F. E. (1990). Roughness effects on flow and shear stress near outside bank of curved channel. *Journal of Hydraulic Engineering, 116*(4), 563-577.

Jin, Y., Zarrati, A., & Zheng, Y. (2004). Boundary shear distribution in straight ducts and open channels. *Journal of Hydraulic Engineering, 130*(9), 924-928.

Jing, H., Guo, Y., Li, C., & Zhang, J. (2009). Three-dimensional numerical simulation of compound meandering open channel flow by the reynolds stress model. *International Journal for Numerical Methods in Fluids, 59*(8), 927-943.

Jueyi, S., Jun, W., Yun, H., & Faye, K. (2010). Velocity profiles and incipient motion of frazil particles under ice cover. *International Journal of Sediment Research, 25*(1), 39-51.

Kabiri-Samani, A., Farshi, F., & Chamani, M. R. (2012). Boundary shear stress in smooth trapezoidal open channel flows. *Journal of Hydraulic Engineering,*

Kang, H., & Choi, S. (2006). Reynolds stress modelling of rectangular open-channel flow. *International Journal for Numerical Methods in Fluids, 51*(11), 1319-1334.

Kara, S., Stoesser, T., & Sturm, T. W. (2012). Turbulence statistics in compound channels with deep and shallow overbank flows. *Journal of Hydraulic Research, 50*(5), 482-493.

Kean, J. W., Kuhnle, R. A., Smith, J. D., Alonso, C. V., & Langendoen, E. J. (2009). Test of a method to calculate near-bank velocity and boundary shear stress. *Journal of Hydraulic Engineering, 135*(7), 588-601.

Kean, J. W., & Smith, J. D. (2004). Flow and boundary shear stress in channels with woody bank vegetation. *Riparian Vegetation and Fluvial Geomorphology,* , 237-252.

Keller, R., & Rodi, W. (1988). Prediction of flow characteristics in main channel/flood plain flows. *Journal of Hydraulic Research, 26*(4), 425-441.

Kempf, G. (1929). Neue ergebnisse der widerstandsforschung. *Werft, Reederei, Hafen, 10*(234–239), 247-253.

Keulegan, G. H. (1938). *Laws of turbulent flow in open channels* National Bureau of Standards US.

Khodashenas, S. R., & Paquier, A. (1999). A geometrical method for computing the distribution of boundary shear stress across irregular straight open channels. *Journal of Hydraulic Research, 37*(3), 381-388.

Kirkgöz, M. S. (1990). An experimental investigation of a vertical wall response to breaking wave impact. *Ocean Engineering, 17*(4), 379-391.

Kirkgöz, M. S., & Ardiçlioglu, M. (1997). Velocity profiles of developing and developed open channel flow. *Journal of Hydraulic Engineering, 123*(12), 1099-1105.

Knight, D. W., & Demetriou, J. D. (1983). Flood plain and main channel flow interaction. *Journal of Hydraulic Engineering, 109*(8), 1073-1092.

Knight, D. W., Demetriou, J. D., & Hamed, M. E. (1984). Boundary shear in smooth rectangular channels. *Journal of Hydraulic Engineering, 110*(4), 405-422.

Knight, D. W., & Macdonald, J. A. (1979). Hydraulic resistance of artificial strip roughness. *Journal of the Hydraulics Division, 105*(6), 675-690.

Knight, D. W., Omran, M., & Tang, X. (2007). Modeling depth-averaged velocity and boundary shear in trapezoidal channels with secondary flows. *Journal of Hydraulic Engineering, 133*(1), 39-47.

Knight, D., & Shiono, K. (1990). Turbulence measurements in a shear layer region of a compound channel. *Journal of Hydraulic Research, 28*(2), 175-196.

Knight, D., Shiono, K., & Pirt, J. (1989). Prediction of depth mean velocity and discharge in natural rivers with overbank flow. Paper presented at the *Proceedings of the International Conference on Hydraulic and Environmental Modelling of Coastal, Estuarine and River Waters,* 419-428.

Knight, D., Tang, X., Sterling, M., Shiono, K., & Mc Gahey, C. (2010). Solving open channel flow problems with a simple lateral distribution model. Paper presented at the *Riverflow 2010, Proceedings of the International Conference on Fluvial Hydraulics, Braunschweig, Germany,* 8-10.

Konstantinov, N., & Dragnysh, G. (1960). The measurement of friction stress on a surface. *Dsir Rts, 1499*

Kostaschuk, R., & Villard, P. (1996). Flow and sediment transport over large subaqueous dunes: Fraser river, Canada. *Sedimentology, 43*(5), 849-863.

Kostaschuk, R., Villard, P., & Best, J. (2004). Measuring velocity and shear stress over dunes with acoustic doppler profiler. *Journal of Hydraulic Engineering, 130*(9), 932-936.

Kraft, S., Wang, Y., & Oberlack, M. (2011). Large eddy simulation of sediment deformation in a turbulent flow by means of level-set method. *Journal of Hydraulic Engineering, 137*(11), 1394-1405.

Krishnappan, B. G., & Lau, Y. L. (1986). Turbulence modeling of flood plain flows. *Journal of Hydraulic Engineering, 112*(4), 251-266.

Lau, Y. L., & Krishnappan, B. G. (1985). Sediment transport under ice cover. *Journal of Hydraulic Engineering, 111*(6), 934-950.

Lau, Y. (1982). Velocity distributions under floating covers. *Canadian Journal of Civil Engineering, 9*(1), 76-83.

Launder, B. E. (1990). Phenomenological modelling: Present.... and future? *Whither turbulence? turbulence at the crossroads* (pp. 439-485) Springer.

Leighly, J. B. (1932). *Toward a theory of the morphologic significance of turbulence in the flow of water in streams* University of California Press.

Lemmin, U., & Rolland, T. (1997). Acoustic velocity profiler for laboratory and field studies. *Journal of Hydraulic Engineering, 123*(12), 1089-1098.

Leutheusser, H. J. (1963). Turbulent flow in rectangular ducts. *Journal of the Hydraulics Division, 89*(3), 1-19.

Lilly, D. K. (1966). *On the application of the eddy viscosity concept in the inertial sub-range of turbulence* National Center for Atmospheric Research.

Liu, H., & Wu, J. (2015). Estimation of bed shear stresses in the pearl river estuary. *China Ocean Engineering, 29*, 133-142.

Ippen, A. T. (1960). *The distribution of boundary shear stresses in curved trapezoidal channels* Hydrodynamics Laboratory, Department of Civil and Sanitary Engineering, Massachusetts Institute of Technology.

McQuivey, R. S., & Richardson, E. V. (1969). Some turbulence measurements in open-channel flow. *Journal of the Hydraulics Division, 95*(1), 209-224.

Mudge, T., & Sloat, J. (2004). High resolution velocity profiles through ice cover. Paper presented at the *Oceans'04. mtts/ieee Techno-Ocean'04, 3* 1634-1637.

Myers, R. C., & Elsawy, E. M. (1975). Boundary shear in channel with flood plain. *Journal of the Hydraulics Division, 101*(ASCE# 11452 Proceeding)

Naot, D., Nezu, I., & Nakagawa, H. (1993). Hydrodynamic behavior of compound rectangular open channels. *Journal of Hydraulic Engineering, 119*(3), 390-408.

Nagib, H. M., Chauhan, K. A., & Monkewitz, P. (2005). Scaling of high reynolds number turbulent boundary layers revisited. AIAA Paper, 4810, 2005.

Nezu, I., Nakagawa, H., & Tominaga, A. (1985). Secondary currents in a straight channel flow and the relation to its aspect ratio. *Turbulent shear flows 4* (pp. 246-260) Springer.

Nezu, I., & Rodi, W. (1985). Experimental study on secondary currents in open channel flow. Paper presented at the *Proceedings of 21st IAHR Congress 2*, 19-23.

Nezu, I., & Nakagawa, H. (1984). Cellular secondary currents in straight conduit. *Journal of Hydraulic Engineering, 110*(2), 173-193.

Nezu, I., Tominaga, A., & Nakagawa, H. (1993). Field measurements of secondary currents in straight rivers. *Journal of Hydraulic Engineering, 119*(5), 598-614.

Nezu, I., & Nakagawa, H. (1993). *Turbulence in open-channel flows*. Rotterdam; Brookfield: Balkema.

Nguyen, T. D., Wells, J. C., & Nguyen, C. V. (2010). Wall shear stress measurement of near-wall flow over inclined and curved boundaries by stereo interfacial particle image velocimetry. *International Journal of Heat and Fluid Flow, 31*(3), 442-449.

Olsen, O., & Florey, Q. (1952). *Sedimentation studies in open channels: Boundary shear and velocity distribution by the membrane analogy, analytic, and finite-difference methods* Bureau of Reclamation.

Papanicolaou, A. N., Elhakeem, M., & Hilldale, R. (2007). Secondary current effects on cohesive river bank erosion. *Water Resources Research, 43*(12)

Parthasarathy, R., & Muste, M. (1994). Velocity measurements in asymmetric turbulent channel flows. *Journal of Hydraulic Engineering, 120*(9), 1000-1020.

Pasche, E., & Rouvé, G. (1985). Overbank flow with vegetatively roughened flood plains. *Journal of Hydraulic Engineering, 111*(9), 1262-1278.

Patel, V. (1965). Calibration of the preston tube and limitations on its use in pressure gradients. *Journal of Fluid Mechanics, 23*(01), 185-208.

Petryk, S., & Shen, H. (1971). Direct measurement of shear stress in a flume. *Journal of Hydraulic Engineering, 97*(6), 883-887.

Pieterse, A., Puleo, J. A., McKenna, T. E., & Aiken, R. A. (2015). Near-bed shear stress, turbulence production and dissipation in a shallow and narrow tidal channel. *Earth Surface Processes and Landforms, 40*(15), 2059-2070.

Preston, J. (1954). The determination of turbulent skin friction by means of pitot tubes. *JR Aeronaut.Soc, 58*, 109-121.

Pujara, N., & Liu, P. L. (2014). Direct measurements of local bed shear stress in the presence of pressure gradients. *Experiments in Fluids, 55*(7), 1-13.

Raichlen, F. (1967). Some turbulence measurements in water. *Journal of the Engineering Mechanics Division, 93*(2), 73-98.

Rajaratnam, N., & Ahmadi, R. (1983). Meandering channels with floodplains." personal communication.

Rajaratnam, N., & Muralidhar, D. (1969). Boundary shear stress distribution in rectangular open channels. *La Houille Blanche,* (6), 603-610.

Rajaratnam, N., & Ahmadi, R. M. (1979). Interaction between main channel and flood-plain flows. *Journal of the Hydraulics Division, 105*(5), 573-588.

Rameshwaran, P., & Naden, P. S. (2003). Three-dimensional numerical simulation of compound channel flows. *Journal of Hydraulic Engineering, 129*(8), 645-652.

Replogle, J. A., & Chow, V. T. (1966). Tractive-force distribution in open channels. *Journal of the Hydraulics Division, 92*(2), 169-191.

Rezaei, B., & Knight, D. W. (2009). Application of the shiono and knight method in compound channels with non-prismatic floodplains. *Journal of Hydraulic Research, 47*(6), 716-726.

Robert, A., & Tran, T. (2012). Mean and turbulent flow fields in a simulated ice-covered channel with a gravel bed: Some laboratory observations. *Earth Surface Processes and Landforms, 37*(9), 951-956.

Rodi, W., Constantinescu, G., Stoesser, T., & CRCnetBASE. (2013). *Large-eddy simulation in hydraulics*. Leiden, Netherlands: CRC Press/Balkema.

Rodríguez, J. F., & García, M. H. (2008). Laboratory measurements of 3-D flow patterns and turbulence in straight open channel with rough bed. *Journal of Hydraulic Research, 46*(4), 454-465.

Rogallo, R. S., & Moin, P. (1984). Numerical simulation of turbulent flows. *Annual Review of Fluid Mechanics, 16*(1), 99-137.

Shao, X., Wang, H., & Chen, Z. (2003). Numerical modeling of turbulent flow in curved channels of compound cross-section. *Advances in Water Resources, 26*(5), 525-539.

Sharifi, S., Sterling, M., & Knight, D. (2009). A novel application of a multi-objective evolutionary algorithm in open channel flow modelling. *Journal of Hydroinformatics, 11*(1), 31-50.

Shi, J., Thomas, T., & Williams, J. (1999). Large-eddy simulation of flow in a rectangular open channel. *Journal of Hydraulic Research, 37*(3), 345-361.

Shiono, K., & Knight, D. W. (1991). Turbulent open-channel flows with variable depth across the channel. *Journal of Fluid Mechanics, 222*, 617-646.

Sime, L. C., Ferguson, R. I., & Church, M. (2007). Estimating shear stress from moving boat acoustic doppler velocity measurements in a large gravel bed river. *Water Resources Research, 43*(3)

Sinha, J., Das, S. K., Patel, P., & Samtani, B. (2014). Development of two-layered model for compound open-channel flow. *ISH Journal of Hydraulic Engineering, 20*(3), 250-262.

Smagorinsky, J. (1963). General circulation experiments with the primitive equations: I. the basic experiment*. *Monthly Weather Review, 91*(3), 99-164.

Smith, B. T., & Ettema, R. (1997). Flow resistance in ice-covered alluvial channels. *Journal of Hydraulic Engineering, 123*(7), 592-599.

Sofialidis, D., & Prinos, P. (1998). Compound open-channel flow modeling with nonlinear low-reynolds k-ϵ models. *Journal of Hydraulic Engineering, 124*(3), 253-262.

Steffler, P. M., Rajaratnam, N., & Peterson, A. W. (1985). LDA measurements in open channel. *Journal of Hydraulic Engineering, 111*(1), 119-130.

Sterling, M., Beaman, F., Morvan, H., & Wright, N. (2008). Bed-shear stress characteristics of a simple, prismatic, rectangular channel. *Journal of Engineering Mechanics, 134*(12), 1085-1094.

Tang, X., & Knight, D. W. (2008). A general model of lateral depth-averaged velocity distributions for open channel flows. *Advances in Water Resources, 31*(5), 846-857.

Tanner, L., & Blows, L. (1976). A study of the motion of oil films on surfaces in air flow, with application to the measurement of skin friction. *Journal of Physics E: Scientific Instruments, 9*(3), 194.

Teal, M. J., Ettema, R., & Walker, J. F. (1994). Estimation of mean flow velocity in ice-covered channels. *Journal of Hydraulic Engineering, 120*(12), 1385-1400.

Thomas, T., & Williams, J. (1995). Large eddy simulation of a symmetric trapezoidal channel at a Reynolds number of 430,000. *Journal of Hydraulic Research,* 33(6), 825-842.

Thornton, C., I., Cox, A., L., & Sclafani, P. (2008). *Preston tube calibration.* (). Fort Collins, Colorado:

Tominaga, A., & Nezu, I. (1991). Turbulent structure in compound open-channel flows. *Journal of Hydraulic Engineering, 117*(1), 21-41.

Tominaga, A., Nezu, I., Ezaki, K., & Nakagawa, H. (1989). Three-dimensional turbulent structure in straight open channel flows. *Journal of Hydraulic Research, 27*(1), 149-173.

Tropea, C., Yarin, A. L., & Foss, J. F. (2007). *Springer handbook of experimental fluid mechanics* Springer Science & Business Media.

Tsai, W., & Ettema, R. (1994). Ice cover influence on transverse bed slopes in a curved alluvial channel. *Journal of Hydraulic Research, 32*(4), 561-581.

Widera, P., Toorman, E., & Lacor, C. (2009). Large eddy simulation of sediment transport in open-channel flow. *Journal of Hydraulic Research, 47*(3), 291-298.

Wilcock, P. R. (1996). Estimating local bed shear stress from velocity observations. *Water Resources Research, 32*(11), 3361-3366.

Wilcox, D. C. (2006). *Turbulence modeling for CFD*. La Cãnada, Calif.: DCW Industries.

Xie, Z., Lin, B., & Falconer, R. A. (2014). Turbulence characteristics in free-surface flow over two-dimensional dunes. *Journal of Hydro-Environment Research, 8*(3), 200-209.

Yamashita, S., Shimizu, Y., & Hohjo, K. (1992). Characteristics of shear stress in the ice-covered river. Paper presented at the *Proceedings of the International Symposium on Ice. Banff, Canada,* 356-360.

Yang, S., & Lim, S. (1997). Mechanism of energy transportation and turbulent flow in a 3D channel. *Journal of Hydraulic Engineering, 123*(8), 684-692.

Yang, S., & Lim, S. (1998). Boundary shear stress distributions in smooth rectangular open channel flows. *Proceedings of the Institution of Civil Engineers.Water, Maritime and Energy, 130*(3), 163-173.

Yang, S., & Lim, S. (2005). Boundary shear stress distributions in trapezoidal channels. *Journal of Hydraulic Research, 43*(1), 98-102.

Yang, S., & McCorquodale, J. A. (2004). Determination of boundary shear stress and Reynolds shear stress in smooth rectangular channel flows. *Journal of Hydraulic Engineering, 130*(5), 458-462.

Yoon, J., & Patel, V. (1996). Numerical model of turbulent flow over sand dune. *Journal of Hydraulic Engineering, 122*(1), 10-18.

Yu, G., & Tan, S. (2007). Estimation of boundary shear stress distribution in open channels using flownet. *Journal of Hydraulic Research, 45*(4), 486-496.

Zarbi, G., & Reynolds, A. (1991). Skin friction measurements in turbulent flow by means of preston tubes. *Fluid Dynamics Research, 7*(3), 151-164.

Zarrati, A., Jin, Y., & Karimpour, S. (2008). Semianalytical model for shear stress distribution in simple and compound open channels. *Journal of Hydraulic Engineering, 134*(2), 205-215.

Zedler, E. A., & Street, R. L. (2006). Sediment transport over ripples in oscillatory flow. *Journal of Hydraulic Engineering, 132*(2), 180-193.

Zheng, Y., & Jin, Y. (1998). Boundary shear in rectangular ducts and channels. *Journal of Hydraulic Engineering, 124*(1), 86-89.